FLUX PINNING IN SUPERCONDUCTING Nb-Ti ALLOYS

by

JAMES CHARLES McKINNELL

A thesis submitted in partial fulfillment of the

requirements for the degree of

Doctor of Philosophy

(Materials Science)

at the

UNIVERSITY OF WISCONSIN-MADISON

1990

Acknowledgements

The work presented in this thesis was carried out under the supervision of Dr. David Larbalestier. I am grateful for the constant support David gave me during my graduate work even when he didn't completely agree with the course I was taking. I am also thankful for his commitment to be readily available for consultation even when he was very busy.

The monetary support of my work by the Electrical Power Research Institute (EPRI) and the Department of Energy - High Energy Physics is gratefully acknowledged. EPRI provided the funds to purchase the alloys for my work and picked up the large tab for my liquid helium usage.

There are also numerous persons from the superconducting materials research group who helped me during my graduate work. Bill Warnes and Ken Marken were always willing to answer my endless questions after my arrival in Madison. Bill Starch and Bob Remsbottom provided a tremendous amount of assistance by fabricating wire and experimental apparatus to my specifications. Alex Squitieri helped keep experimental equipment operating and helped with some of the short sample testing. Peter Lee has spent a considerable portion of his time in recent years doing microscopy on

my samples. Tom Willis willingly did microprobe analysis on my samples. I have had numerous helpful discussions over the years with Henry Muller, Christoph Meingast, Manfred Daeumling, Jeff Seuntjens, Lance Cooley, and Paul Jablonski.

I would also like to thank all the members of my family and my friends at First Baptist Church for their support during my graduate studies. My father (James) and mother (Letha) encouraged me to pursue graduate study and have always been behind me. Trudy, my wife, deserves a special thanks for her love and support throughout this whole affair. She has endured through living rooms that have looked more like MACC than a living room and bathrooms and basements which have been converted to darkrooms. More importantly she has always been there when I have hit the bottom and has put me right back on my feet again.

Contents

List of Figures

List of Tables

Chapter 1

Introduction

Niobium titanium alloys are the most widely applied superconducting materials in the world today. Although other superconductors operate at higher temperatures and magnetic field levels, ease of fabrication and ductility have made Nb-Ti the choice of the superconducting magnet industry. The applications for superconducting Nb-Ti are primarily in the form of magnets. In particle accelerators, the largest machines in which superconductors are used, 5-7 Tesla (T) superconducting dipole magnets supply the bending field for the particle beam. Whole body Magnetic Resonance Imaging (MRI) units use large superconducting solenoids to supply a 1-2 T background field for aligning the protons in the nuclei of a patient's atoms. Small laboratory magnets are the final common form of application for superconductors. Nb-Ti

wire is used for making magnets capable of achieving fields as high as 9T at 4.2K and 12T at 1.8K.

From an engineering point of view, the three important properties of a superconductor are the upper critical field (H_{c_2}), the critical temperature (T_c), and the critical current density (J_c). H_{c_2} is the magnetic field intensity at which superconductivity vanishes and the normal metallic electromagnetic properties return. Figure 1.1 shows the relationship between H_{c_2} and alloy composition in the Nb-Ti system. The commercial Nb46.5wt%Ti alloy lies near the peak of the curve ($H_{c_2} \approx 11$T at 4.2K). T_c is the temperature above which the material behaves like a normal metal. As shown in figure 1.2 the peak in T_c is much broader than the peak for H_{c_2}. For the commercial Nb46.5wt%Ti alloy $T_c \approx 9$K (for zero applied field). J_c is the maximum loss-less current density a superconductor will carry. J_c is a strong function of the applied magnetic field, the temperature, and the thermo-mechanical history of the material. For commercial Nb46.5wt%Ti, the 5T, 4.2K current density ranges from $\approx 100 A/mm^2$ to $\approx 3700 A/mm^2$ depending on the thermo-mechanical history.

Over the past decade Larbalestier's group at the University of Wisconsin-Madison has done much to increase the current density in Nb46.5wt%Ti. The impetus for this work has been the need for higher J_c Nb-Ti wires for particle accelerator dipole magnets. The impetus for this study was the requirement

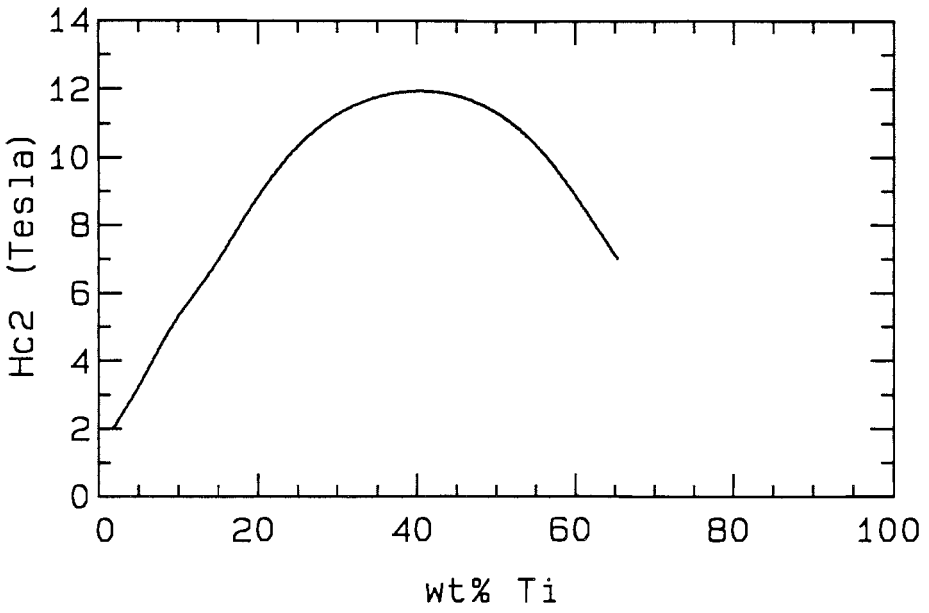

Figure 1.1: A fit to the data, compiled by Hawksworth, for H_{c_2} of Nb-Ti versus alloy composition at 4.2°K [29].

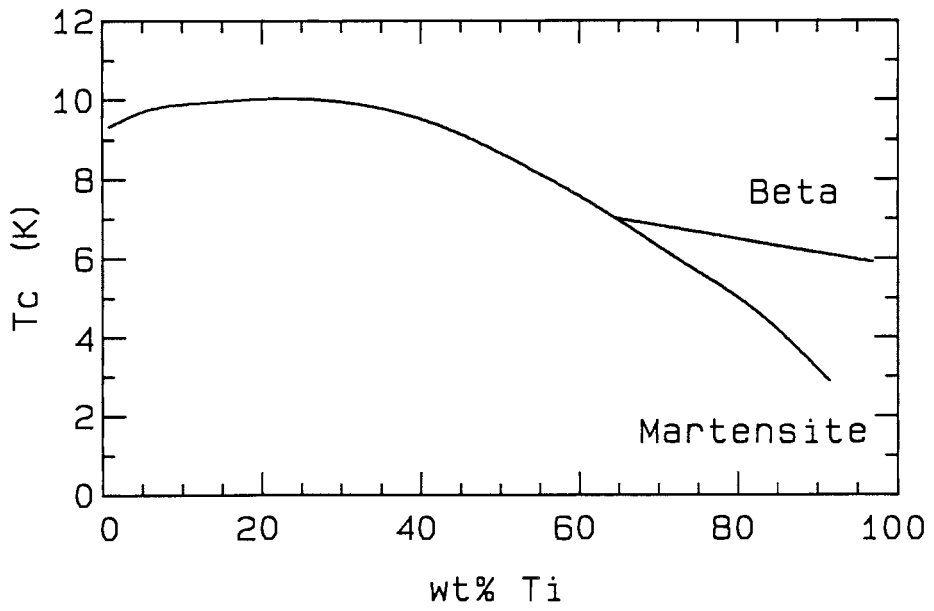

Figure 1.2: A fit to the data, compiled by Hawksworth, for T_c of Nb-Ti versus alloy composition in zero field [29].

of high J_c at low fields (2-3T) for large superconducting magnetic energy storage (SMES) magnets [6]. Several years ago Larbalestier [35] noted that alloys with a Ti content higher than the Nb46.5wt%Ti alloy had potential for producing high current densities at low field. In addition to potential increases in low field J_c with the high Ti alloys, there is also a potential savings in alloy cost because Nb costs about 10 times as much per pound as Ti. The overall purpose of this study was to optimize J_c in the range of alloys from Nb46.5wt%Ti to Nb62wt%Ti.

1.1 Flux Pinning

Two different classes of superconducting materials exist, and they can be distinguished by their magnetic behavior. Type I superconductors are characterized magnetically (see figure 1.3) by the exclusion of all magnetic flux beyond a field penetration depth λ [51]. This exclusion of the magnetic flux is a result of the positive interfacial energy between the normal and superconducting state which makes flux exclusion favorable. Exclusion of all magnetic flux from the sample causes an increase in the free energy per unit volume of the material which is proportional to the square of the applied field. Thus for fields greater than a few hundred gauss, the increase in free energy due to the exclusion of all flux is greater than the decrease in free energy associated

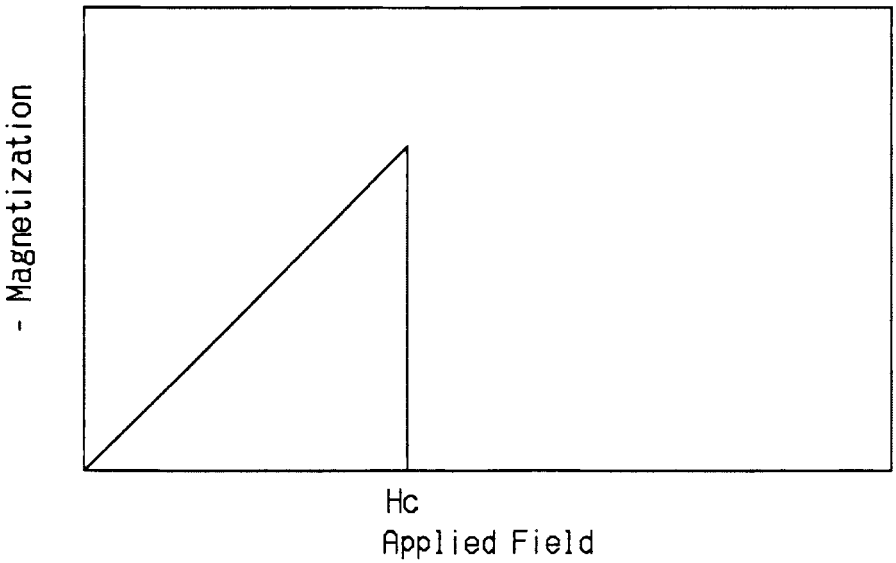

Figure 1.3: Schematic of an ideal magnetization curve for a Type I superconductor.

with the superconducting state, and the material returns to the normal state.

Type II superconductors have a quite different magnetic behavior compared to that observed in Type I superconductors. Figure 1.4 shows the magnetization curve for an ideal reversible Type II superconductor. Initially, as in a Type I superconductor, all flux is excluded. Upon reaching the field H_{c_1}, flux begins to penetrate the material. Eventually, superconductivity is destroyed at the field H_{c_2}. In this case the energy of the normal-superconducting interface is negative, which makes the flux penetration into the material favorable. When flux penetrates a Type II material, less of the material is excluding flux than in the case of the Type I, and thus the free energy per unit volume of the superconductor increases more slowly with

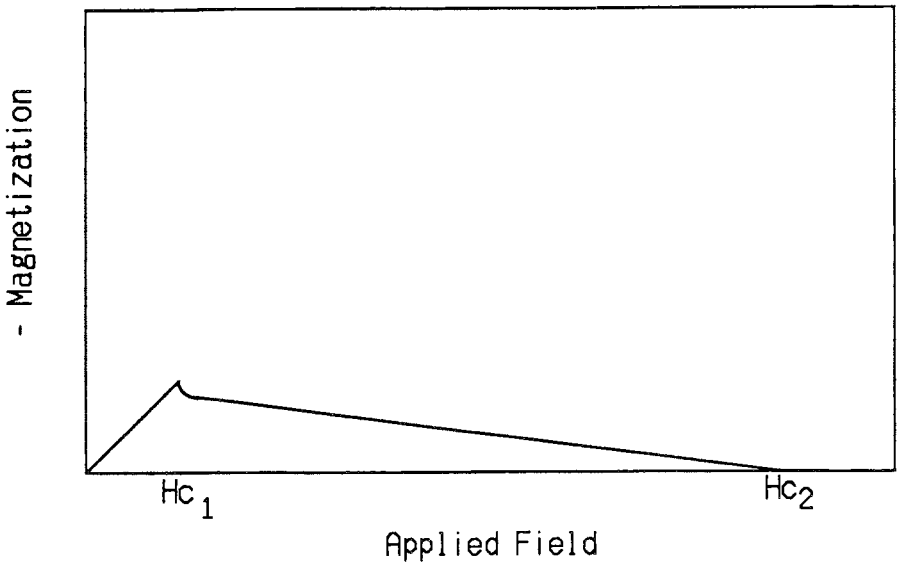

Figure 1.4: Schematic of an ideal magnetization curve for a reversible Type II superconductor.

increasing field than in the case of the Type I material. This allows Type II materials to remain in the superconducting state to higher fields than Type I materials. The flux which penetrates the material does so in quantum units called fluxons ($\phi_0 = 2.07 \times 10^{-15} Wb$) [3]. These fluxons have two characteristic lengths associated with them. The first is the field penetration depth λ. The second is the coherence length ξ which is the characteristic distance over which interactions between superconducting electrons takes place. The parameter $\kappa = \lambda/\xi$ describes their difference in behavior. If $\kappa < 1/\sqrt{2}$ the material is Type I, and if $\kappa > 1/\sqrt{2}$ the material is Type II [18]. Niobium titanium is a Type II material with $\xi \approx 6nm$ at 4.2K. κ for Nb-Ti may be

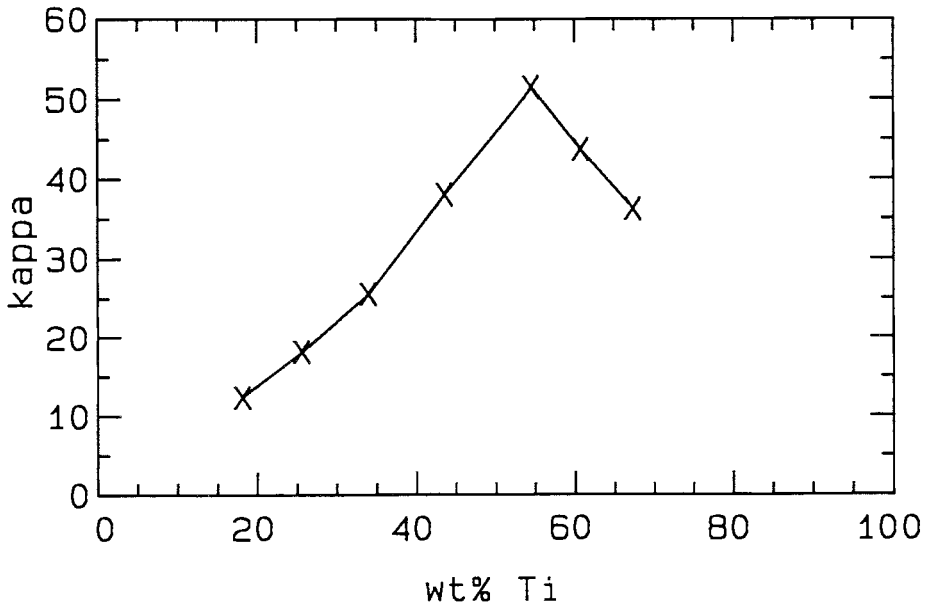

Figure 1.5: Kappa (κ) for β phase Nb-Ti alloys.

calculated from

$$\kappa = 7.49 \times 10^3 \gamma^{1/2} \rho. \tag{1.1}$$

where γ is the electronic specific heat in $(erg)/(cm^3K^2)$ and ρ is the resistivity in Ωcm [68]. Figure 1.5 shows the relationship between κ and the alloy composition using Muller's data for γ and ρ and calculating the alloy density by a random mixing approximation [66].

Type I and Type II superconductors also have different properties with respect to transport current. In a Type I superconductor all the current flows in a sheath of depth λ near the surface. Superconductivity is maintained until the local field exceeds H_c. The material then returns to a resistive normal state. Thus the appearance of a voltage across a specimen with increasing

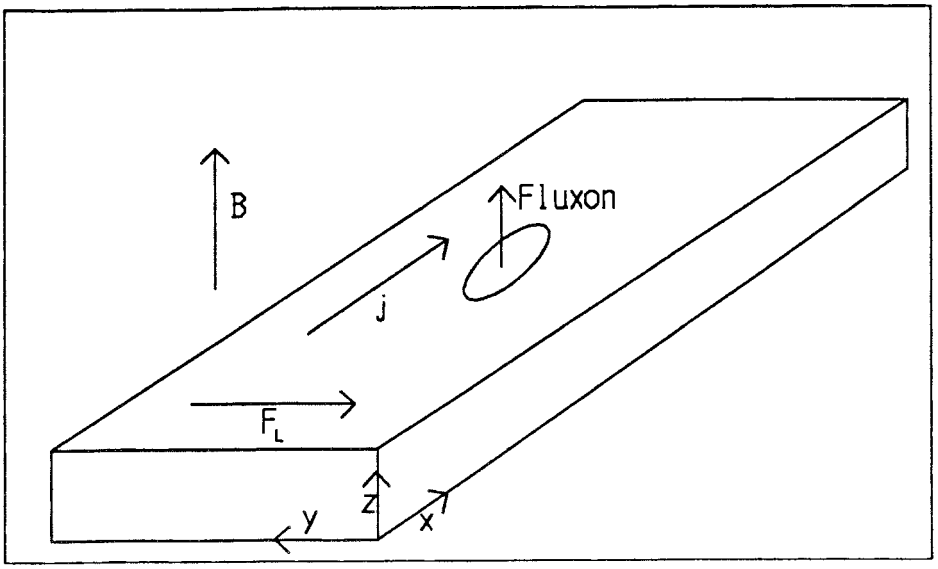

Figure 1.6: Schematic of the Lorentz force on an isolated fluxon.

current is associated with a return to the normal state. In a Type II material the appearance of a voltage across the specimen does not necessarily indicate a return to the normal state.

Figure 1.6 shows an isolated fluxon in a superconducting slab. If a field is applied in the $\vec{z}$ direction then the fluxon will thread the material in the $\vec{z}$ direction. If a transport current is now applied in the $\vec{x}$ direction then there will be a Lorentz force ($\mathbf{F}_L = \mathbf{J} \times \mathbf{B}$) acting on the fluxon in the $-\vec{y}$ direction. If the fluxon is not held in place, then the fluxon will move under the applied force dissipating an amount of energy $\Delta W = F_L \Delta y$. This will lead to the appearance of a voltage across the material. Thus the first appearance of a voltage across a Type II superconductor is associated with fluxon motion and

not with a return to the normal state. The normal state is achieved if enough current is passed such that the energy dissipation due to flux motion causes an increase in temperature above the T_c characteristic of the applied field. In order for Type II superconductors to carry loss-less transport current, there must be pinning centers which prevent flux motion in the material.

Fluxons may be pinned in the material by defects. Defects lower the energy required for the existence of a fluxon in the superconducting material. The typical types of defects which pin flux in superconducting materials are voids, grain boundaries, precipitates, and dislocations. The simplest case for flux pinning in a superconductor is the case of an isolated fluxon occupying a small void of volume V. The energy reduction associated with the presence of the fluxon in the superconductor is [80]

$$\Delta G = \frac{\mu_0 {H_c}^2 V}{2}. \tag{1.2}$$

Thus the presence of the void acts as a potential well for the fluxon. The elementary pinning force (f_p) may then be estimated by dividing the potential by ξ, the range over which the order parameter changes. This gives

$$f_p = \frac{\mu_0 {H_c}^2}{2}\frac{V}{\xi}. \tag{1.3}$$

This equation can be put in terms of H_{c_2} and κ by using

$$H_{c_2} = \kappa\sqrt{2}H_c = \frac{\phi_0}{2\pi\mu_0\xi^2}, \tag{1.4}$$

which yields

$$f_p = \frac{(2\pi\mu_0)^{3/2} {H_{c_2}}^{5/2}}{48{\phi_0}^{1/2}\kappa^2}. \tag{1.5}$$

Calculations such as this allow an estimate of the elementary pinning interaction f_p. A tabulation of the elementary pinning interactions for several other forms of defects has been compiled by Dew-Hughes [10].

In the simple case above, only the ΔH_c contribution to the free energy was considered. In the Ginzburg–Landau theory a secondary contribution to the free energy, and thus to f_p, is the variance in κ due to electron scattering. The contribution to the free energy by both ΔH_c and $\Delta\kappa$ forms of pinning can be written as [9]:

$$\Delta E = \int \mu_0 {H_c}^2 (-\frac{\delta H_{c_2}}{H_{c_2}}|\Psi|^2 + \frac{1}{2}\frac{\delta\kappa^2}{\kappa^2}|\Psi|^4) dV. \tag{1.6}$$

To show the ΔH_c and $\Delta\kappa$ contributions directly, equation 1.6 can be rewritten by combining with equation 1.4 which yields:

$$\Delta E = \int \mu_0 {H_c}^2 \left[-\frac{\delta H_c}{H_c}|\Psi|^2 - \frac{\delta\kappa}{\kappa}\left(|\Psi|^2 - |\Psi|^4\right)\right] dV. \tag{1.7}$$

In the case of Nb-Ti wires, the pinning centers are generally α -Ti precipitates which have been cold worked into fine ribbons (when examined in transverse cross section) which extend several microns along the drawing axis of the wire [43]. These fine ribbons contribute both to the ΔH_c term and the $\Delta\kappa$ term of equation 1.7.

Equations such as those above may be used to calculate the strength of a single fluxon interacting with a single pinning center. As more fluxons are added to the material fluxon—fluxon interactions occur. As the density of fluxons increases, the fluxons are pushed closer together, and the fluxons repel each other. In the absence of pinning centers, this repulsion leads to the formation of a flux line lattice [2].

The interaction between the lattice forces on the fluxons and the elementary pinning centers has been a topic of interest for some time [9, 10, 33]. One approach to this problem is to assume that the global pinning force F_p depends on the elementary pinning interaction f_p times the density of pins ρ_p. This value is then modified by a pinning efficiency factor (C) which is representative of the way the fluxons interact with the pins in the material. The expression for the global pinning force may then be written as:

$$F_p = C\rho_p f_p. \tag{1.8}$$

Two of the considerations which control the efficiency factor C are the rigidity of the flux line lattice (FLL) and the geometrical distribution of pinning centers in the material. Most materials have a random distribution of pinning centers, or at best some weak texturing. Using the case of random pinning centers, consider what happens if the attractive force in the FLL is varied. First, take the case of a FLL with a very weak FLL interaction. In

this case flux can readily move to a pinning site. If the density of pinning sites is greater than the density of fluxons, each fluxon is locally pinned by the force f_p. For this case, C would be 1, the maximum value. If we look at the other extreme case where the FLL interaction is strong, then fluxons sit where the inter fluxoid (i.e. lattice) forces push them. In this case, the value of C will be zero, since the random forces on individual fluxons will sum to zero.

Experimentally the pinning force F_p is determined by using the expression:

$$\mathbf{F}_p = \mathbf{J}_c \times \mathbf{B} \tag{1.9}$$

to obtain F_p from critical current data. f_p is then traditionally calculated from equation 1.8 using a value of $1/2$ for C [44] (this gives $f_p \approx 300 N/m^2$ for optimized Nb-Ti at 5T, 4.2K). Although using $1/2$ for the value of C may not be strictly correct, it provides a useful first approximation of the actual case consisting of randomly distributed pinning centers in a material. Recently, Meingast and Larbalestier have shown evidence for direct summation (C = 1) in optimized Nb-Ti wires [62].

Scaling of the global pinning force with temperature is a phenomena often observed in high κ superconductors. Scaling was first noted by Fietz

and Webb [13] and can be expressed as [21]

$$F_p = (B_{c_2}(T))^q f(b). \tag{1.10}$$

The table by Dew-Hughes [10] also contains theoretical scaling expressions for the various types of pinning centers. Experimentally it has often been noted that for Nb-Ti, $f(b)$ goes as $b(1-b)$ and for Nb_3Sn it goes as $b^{1/2}(1-b)^2$ [40]. Many technologically important superconductors exhibit scaling behavior. This allows reliable prediction of current densities at various temperatures, once a pinning force curve has been experimentally determined at one temperature [29]. However, scaling does not always occur. A lack of scaling in superconducting materials is often associated with the presence of two different types of pinning centers, size matching between vortices and pinning centers, or flux creep [9].

In the Nb-Ti system there have been many reports of scaling behavior [13, 16, 21, 22, 23, 24, 28, 54]. However, recently there have been two reports of non-scaling in Nb-Ti wires [34, 62]. The first report by Küpfer and Matsushita found the coefficient q in equation 1.10 depended on the reduced field ($b = B_{applied}/B_{c_2}$). A lack of scaling was also seen by Meingast and Larbalestier [62]. In this case they attributed the lack of scaling behavior to the presence of two different pinning mechanisms: ΔH_c and $\Delta\kappa$. They argued that the lack of scaling was due to the different temperature dependencies of

the two pinning mechanisms.

What Meingast and Larbalestier observed for optimized Nb47.8wt%Ti as the temperature increased was that the reduced field at which the maximum in the pinning force occurred (b_p) shifted toward lower reduced field. They explained this effect by considering the plot in figure 1.7 and equation 1.7. At 4.2K the relative changes in κ and H_c for varying compositions are comparable. At 8K this is no longer true because H_c now varies more strongly with composition than κ. Thus they concluded that the shift of b_p to low field with increasing temperature was due to the increasing dominance of the ΔH_c term in equation 1.7.

Using their conclusion Meingast and Larbalestier put forth a hypothesis concerning the flux pinning behavior of Nb-Ti alloys containing ~60wt%Ti. For these high Ti alloys it has been observed that the shape of the f_p curve is much more like $b^{1/2}(1-b)^2$ than like the $b(1-b)$ usually seen in commercial Nb-Ti alloys [16, 57, 70]. Since the high Ti alloys lie closer to the steep part of the H_c versus composition curve in figure 1.7, Meingast and Larbalestier predicted that ΔH_c pinning would dominate in the high Ti alloys.

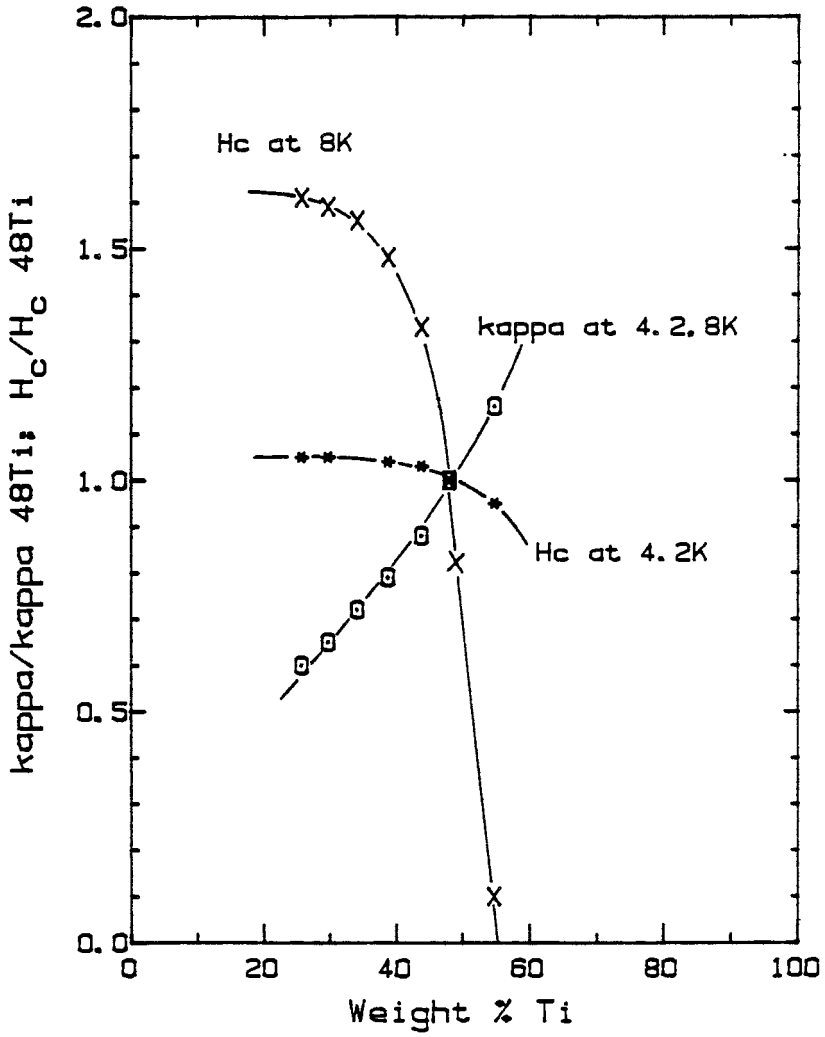

Figure 1.7: Normalized values of ΔH_c and $\Delta\kappa$ pinning interactions at 4.2°K and 8°K [62].

1.2 Nb-Ti Metallurgy

As discussed in section 1.1 the flux pinning behavior and thus J_c for Nb-Ti wires is related to the defect structure of the material. At equilibrium, below 880°C, there are two phases α and β as shown in figure 1.8 [26]. For the alloys of this study, the pinning defects are α -Ti precipitates in the β matrix. In addition to the the equilibrium phases, there are also three metastable phases (α', α'' and ω). These, grain boundaries and dislocations may all pin flux. The phase diagram for this system has been experimentally determined up to about 50wt%Nb. Further experimental determination of the phase diagram has been hampered by the sluggishness of the kinetics with increasing Nb content. The sluggishness is primarily due to an increase in T_m from ~1720°C for pure Ti to ~2400°C for pure Nb with increasing Nb content while the temperature of the phase boundary between β and the $\alpha+\beta$ region is dropping from $\sim 880°C$ for pure Ti to $\sim 570°C$ for Nb34wt%-Ti [35]. Thus at Nb34wt%Ti T/T_m for the two phase boundary is about 0.4 which is too low for rapid diffusion to take place.

1.2.1 β-phase

The β-phase of the Nb-Ti alloy system is BCC, as is Nb. The β-phase is also stable for Ti above 880°C. The lattice parameter of the β-phase ranges from

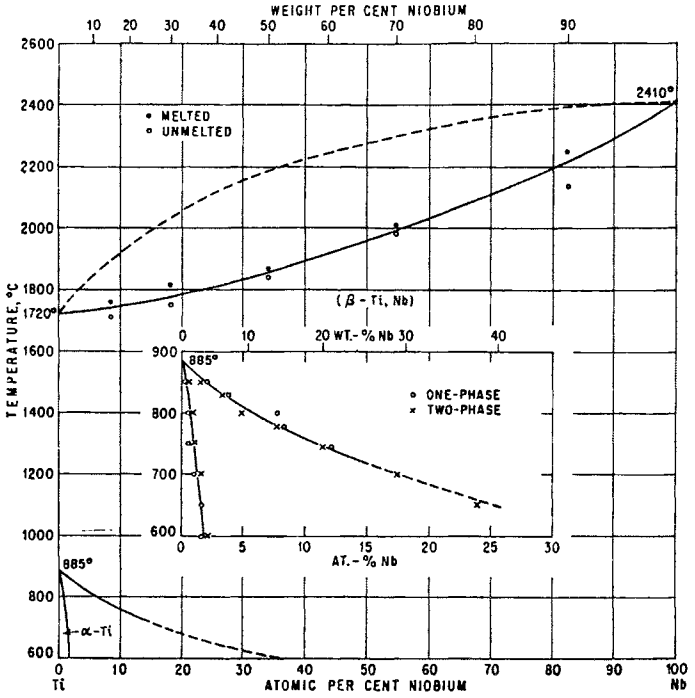

Figure 1.8: Equilibrium phase diagram for the Nb-Ti system [25, 26].

$\sim 0.328nm$ to $\sim 0.330nm$ [63] with increasing Nb content. For the alloys of this study the β-phase is stable above $\approx 650°$C. β also forms the matrix in which precipitation takes place.

1.2.2 α-phase

The α-phase of this alloy is HCP, as is Ti at room temperature. The lattice parameters of the α-phase are a : $0.2956nm$ and c : $0.4716nm$ [63]. Two forms of α precipitates are generally seen. The first is the intragranular Widmanstätten form, whose appearance is needlelike. This type of α grows with $(0001)_\alpha \parallel (110)_\beta$ and $< 1120 >_\alpha \| < 111 >_\beta$ [8]. The second form is equiaxed grain boundary triple point precipitation. The equiaxed precipi-

tates were determined to contain ≥90wt% Ti by Lee and Larbalestier using EDS techniques [43].

1.2.3 α'-phase

The martensitic α'-phase is HCP [64] with lattice constants similar to α. α' occurs in alloy containing up to 13wt%Nb. α' has the same orientational relationships as α [8]. Since this martensite is seen only at very low Nb concentrations, this phase is not expected to occur in the alloys of this study.

1.2.4 α''-phase

The martensitic α'' phase is C-centered orthorhombic [64]. It exists in the compositional range from 13wt%Nb to 47wt%Nb [64]. The lattice parameters of this phase vary smoothly from near the HCP of α-Ti to the BCC of β-Nb-Ti as the Nb concentration is increased [64]. α'' also obeys the same orientational relationships with the matrix as α[8]. Some of the Nb-Ti alloys for this study, from Nb53wt%Ti to Nb62wt%Ti, could show α'' precipitation. However, Moffat and Larbalestier [64] showed that ω-phase forms preferentially over α'' unless the quench rate from the β-phase region is extremely fast.

1.2.5 ω-phase

The metastable ω-phase is hexagonal and has lattice parameters relative to the β-phase of $a_\omega = \sqrt{2}a_\beta$, $c/a = \sqrt{3/8}$ [73]. The ω-phase forms in the compositional range from 26–46wt%Nb. This phase may form either by slow cooling or by quenching and aging. ω precipitates are ellipsoidal in shape. The presence of the ω-phase is accompanied by a large increase in hardness and change in the slope of resistivity versus composition [63]. The ω-phase also observes an orientational relationship with the matrix. The orientational relationship is $(0001)_\omega \parallel (111)_\beta$ and $[11\underline{2}0]_\omega \parallel [110]_\beta$ [8]. All the alloys of this study are in the proper compositional range for ω-phase precipitation. Additionally, according to Moffat and Larbalestier [65], ω occurs more readily as the Ti content of the alloys increases.

1.3 A Brief History of Nb-Ti Superconductors

The first report of the combination of mechanical working and precipitation heat treatments in Nb-Ti alloys was made by Vetrano and Boom in 1965 [81]. They obtained critical current densities of $\sim 1200 A/mm^2$ (3T, 4.2K) in a Nb65wt%Ti alloy which had been recrystallized, cold rolled for

an area reduction of 80%, and given a 3h heat treatment of $\sim$ 430°C. The precipitates formed by this heat treatment were identified as α -Ti by X-ray analysis.

Several years after the first production of commercial Nb-Ti, Pfeiffer and Hillman [73] published results on Nb50wt%Ti and Nb65wt%Ti which identified some of the important aspects of processing on the microstructure of Nb-Ti. First, cold working of the alloy from the larger as - cast size to smaller sizes caused an increase in the grain boundary density with a corresponding decrease in grain size. Upon heat treatment in the two-phase region, the boundaries of this refined grain structure were observed to act as nucleation sites for α-Ti particles. In addition, multiple heat treatments were required at various sizes to obtain good precipitation in their Nb50wt%Ti alloy. Pfeiffer and Hillman obtained their best critical current densities in materials receiving cold work following the heat treatment. Using the cold work—precipitation heat treatment—cold work cycle, they obtained $\sim 2000 A/mm^2$ (4.2K, 5T) in Nb50wt%Ti. Pfeiffer and Hillman also discussed the occurrence of the ω-phase in Nb65wt%Ti. They noted that the ω-phase occurred in recrystallized, cooled and aged alloys but not as readily in specimens receiving severe cold work prior to aging. Thus, by the end of 1968, the cold work—precipitation heat treatment—cold work cycle had been shown to produce high J_c values in Nb50wt%Ti and Nb65wt%Ti. In addition, it had been

shown that the hardening ω-phase could be avoided by large amounts of cold work.

Following the work of Pfeiffer and Hillman, there was little progress toward improving J_c for quite some time. In 1971, Neal et al. [67] reported work on Nb42wt%Ti which was thought to be single phase β with no α-Ti precipitate present in their alloy. They reported a general inverse dependence of J_c on grain size (i.e. $J_c \propto 1/d$) and these results were used by Hampshire and Taylor to model the pinning in terms of $\Delta\kappa$ variation at cell walls produced by the drawing process [21, 36].

At about the same time as these studies [67, 73], McInturff and Chase [55] systematically studied Nb-Ti alloys in the range of Nb46wt%Ti to Nb65-wt%Ti. They found a weak peak in J_c of $\sim 1100 A/mm^2$ (5T, 4.2K) for Nb61wt%Ti for a cold work—precipitation heat treatment—cold work cycle. Although no microstructural studies were performed, the enhanced J_c values of heat treated alloys were ascribed to precipitation of a second phase.

At the time of the late 1970's, there was a lack of fundamental understanding of the limits to developing high J_c in the Nb-Ti system and no systematic understanding of how to choose the best alloy or its optimum processing. There were occasional reports of high current densities in the alloy system such as $3380 A/mm^2$ (4.2K, 5T) on short samples by Willbrand and Schlump [85] in the mid 1970's. However, in longer lengths these wires

achieved only $2800 A/mm^2$ [86]. On an industrial scale, J_c values were much lower ($1500–2000 A/mm^2$ at 5T), with occasional poorly understood improvements. Optimization of the J_c on an industrial scale involved proprietary fabrication processes which were not founded in fundamental knowledge and had only limited transferability from one conductor design to another. The state of the art in the period 1975 to 1982 for Nb-Ti wire is exemplified by the Fermilab Energy Doubler conductor. Over 1000 billets of this wire were produced and J_c(5T) ranged from about $1700–2000 A/mm^2$. In an early survey of the previously published literature Larbalestier [35] proposed the NbTi alloys be broken into three distinct catagories: high Nb, intermediate, and high Ti. This categorization turned out to be invalid when the system finally became understood.

The principal developments of Nb-Ti superconducting composites in the 1980's have been carried out by Larbalestier's group at the University of Wisconsin - Madison. In 1979 West and Larbalestier [84] reported results which challenged many of the long - held beliefs in the field. The first of these beliefs was that high Nb alloys did not produce α-Ti precipitation. Using the better resolution of newer TEM [36] instruments, they showed precipitation of α-Ti in grain boundaries of a material which matched the electromagnetic data of Neal, et al. Second, they asserted that the boundaries observed in Nb46.5-wt%Ti were actually high angle grain boundaries and not sub-bands. Third,

they showed that cold work following heat treatment caused the equiaxed α-Ti precipitates to form into flattened ribbons which are of size and spacing similar to that of the equilibrium fluxoid spacing at 5T. Larbalestier and West also noted the presence of non-uniform precipitation in the material and speculated that this was due to compositionally inhomogeneous starting material. Their conclusions were strengthened by the report in 1982 of very high J_c(5T) values in Nb50wt%Ti by Li Chengren et al [49]. These authors supplied samples to Larbalestier's group so that the reported high values ($> 4000A/mm^2$) could be verified. In fact they had J_c(5T) at $10^{-14}\Omega m$ of $3400A/mm^2$, a value clearly the highest achieved to that time. [1]

Larbalestier et al. were investigating the effect of material homogeneity [37]. In collaboration with Teledyne Wah Chang-Albany, Intermagnetics General Company and the Lawrence Berkeley Laboratory, a billet of high homogeneity Nb46.5wt%Ti material (HiHo) was produced. The high homogeneity material performed considerably better than standard material in a Fermi Lab type heat treatment optimization ($2365A/mm^2$ compared to the average of $\sim 1850A/mm^2$, 5T, 4.2K for Fermi Lab material). Using a new three heat treatment process developed in the UW Laboratory, J_c(5T) was

[1] Li Chengren et al. have never revealed the full details of their processing. It appears to have involved 6 heat treatments and a process which they were not subsequently able to duplicate. In normal industrial practice it is hard to give more than three heat treatments due to limitations in strain space.

raised to $2750 A/mm^2$. This process is easily adapted to the full industrial scale and has since been almost universally employed. Lab scale processes had simultaneously raised J_c(5T) to $3300 A/mm^2$.

Shortly thereafter, the effect of Cu-Ti intermetallics on the sausaging of filaments was investigated by Larbalestier et al. [37, 38]. Cu-Ti intermetallics were shown to grow at the Cu-Nb-Ti interface during heat treatments rather than at extrusion, as had previously been believed. The fine ($< 100\ nm$ thick layers) were proposed to break up and then agglomerate as the composite was drawn to smaller sizes. The hard Cu-Nb-Ti intermetallics embedded in the ductile Nb-Ti filaments. This causes a variation in cross sectional area (sausaging), which in turn causes a reduction in the overall current the composite can carry. A solution to the problem is to use Nb diffusion barriers at the Cu-Nb-Ti interface [20].

The problems of chemical inhomogeneity and cross sectional area variation are actually very similar problems. Both of these limit the overall current a wire can carry by producing regions of reduced I_c. In the case of inhomogeneities, the defect is the section of the composite having the lowest average critical current density. In the case of sausaging, the defect is the place in the wire with the smallest cross sectional area. Wire of high quality requires careful attention to both of these factors.

During the time that the macroscopic problems of homogeneity and

sausaging were being solved, attention was also being given to the microstructure in the material. In 1986, Buckett and Larbalestier [7] reported work on the importance of the initial cold work given to Nb46.5wt%Ti prior to heat treatment. They found that precipitation in the alloy depended markedly on the amount of initial cold work given the material. For a heat treatment of 40h at 375°C, material receiving a true strain of 2 since the last full anneal showed highly irregular α-Ti precipitation and signs of ω-phase precipitation. Increasing the initial strain since the last full anneal to 5 suppressed the ω-phase and yielded much more uniform α-Ti precipitation across the cross section. This showed that an initial strain of at least 5 is necessary to obtain good J_c results in Nb46.5wt%Ti. These findings are consistent with the general findings of Pfeiffer and Hillman [73].

The next stage of the material optimization was attention to the heat treatment and final strain range of the material processing. Larbalestier et al. reported in 1986 on the effects of increasing the number of heat treatments received during processing [39]. A weak improvement in J_c was seen by increasing the number of heat treatments to six. A very detailed study of the heat treatment by Li and Larbalestier [50] showed three 80h, 420°C heat treatments to be optimum for Nb47.8wt%Ti.

Following the last heat treatment, the specimens showed maximum J_c with a final strain of ~4–5.5, and with current densities as high as

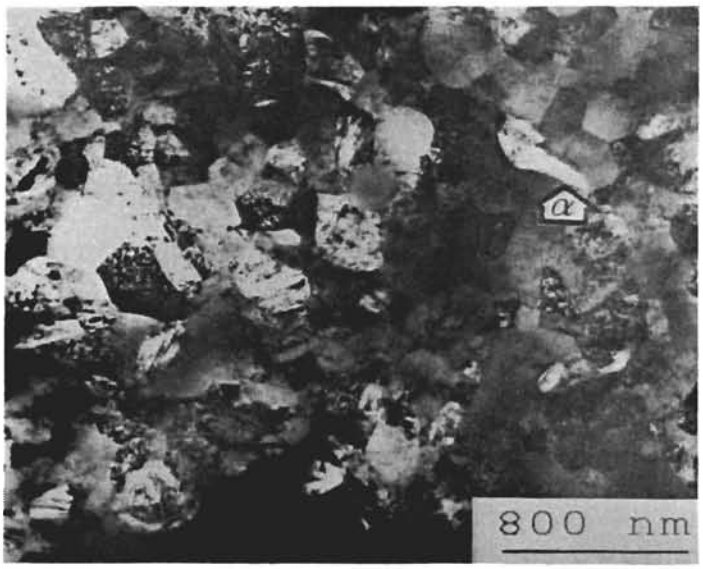

Figure 1.9: TEM cross sectional micrograph showing the equiaxed precipitate morphology of Nb46.5wt%Ti after the last heat treatment ($\epsilon_p = 6.81$, 3X80h/420°C, $\epsilon_i = 1.15$, courtesy of Dr. Peter Lee).

$3680A/mm^2$. Figure 1.9 shows the desired microstructure of Nb46.5wt%-Ti following the last heat treatment. The microstructure resulting from cold work following the final heat treatment is shown in figure 1.10. This highly refined microstructure has resulted in current densities as high as $3800A/mm^2$ [30].

Over time many important processing variables have been identified for making Nb46.5wt%Ti wires. The first important processing variables are controlled by the alloy manufacturer. The manufacturer must insure good material homogeneity without allowing excess grain growth. Grain growth requires additional cold work to obtain microstructural refinement prior to

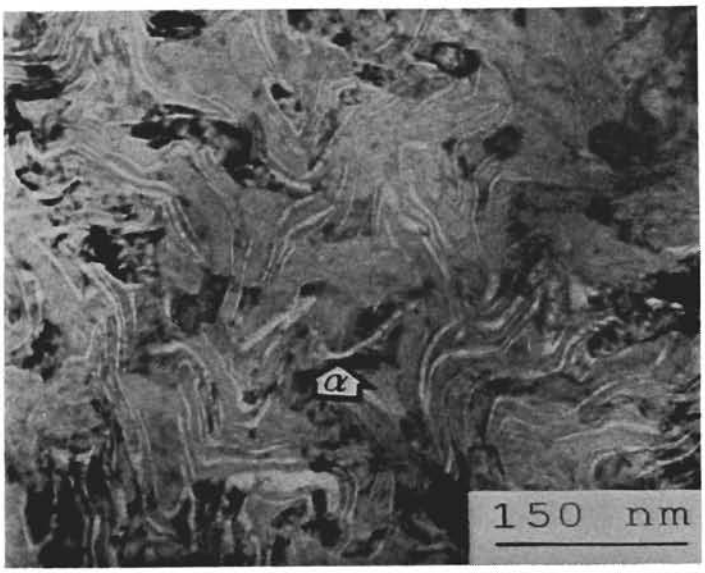

Figure 1.10: TEM micrograph showing the ribbon precipitate morphology at final size for Nb46.5wt%Ti (ϵ_p = 6.81, 3X80/420, ϵ_i = 1.15, ϵ_f = 5.56, courtesy of Dr. Peter Lee).

precipitation heat treatments. Additionally, the alloy manufacturer must deliver rod in the β-phase to insure easy fabrication of the material and uniform precipitation. Following the last anneal in the β-phase region the material must then be worked by cold drawing or extrusion to the first heat treatment size. In this step there must be enough cold work (ϵ_p of at least 5 for Nb46.5wt%Ti) to insure uniform α-Ti precipitation. Billet stacking is usually performed prior to the first heat treatment. Billets can contain from one to over 40000 filaments. Also, a diffusion barrier should be provided if needed to insure the best possible filament quality at final size. Precipitation heat treatments should then be given to allow α-Ti precipitation. Three 80h, 420°C heat treatments have been shown to be optimum. Each heat treatment

should be separated by a true strain of about 1. Following the last heat treatment, an additional strain of about 5 should be given to form the equiaxed Nb-Ti precipitates into ribbons. Occasionally, final size heat treatments increase the current density, but this type of heat treatment tends to degrade current density in fully optimized material. A comprehensive description of the microstructural evolution during the various processing steps is found in Lee and Larbalestier [43]. The flux pinning mechanisms of the highest J_c material have been treated by Meingast, Lee and Larbalestier [61, 62].

1.4 Overview of the Thesis Experiments

This study was composed of three major experiments. At the start of the study, it was unclear how the properties of high Ti alloys would differ from the standard Nb46.5wt%Ti alloy. To investigate this systematically, alloys were special ordered at increments of 4wt%Ti. The resulting nominal compositions were Nb50wt%Ti, Nb54wt%Ti, Nb58wt%Ti, and Nb62wt%Ti. These alloys were fabricated in the same fashion as worked best for Nb46.5wt%Ti alloys. The results from this first standard experiment formed the basis for subsequent experiments.

The standard experiment showed that the J_c values were high for all of the alloys. The alloys containing less than Nb54wt%Ti had current densi-

ties of about $3500A/mm^2$ (5T, 4.2K). The Nb58wt%Ti showed about a 10% improvement in J_c over Nb46.5wt%Ti at 2T and 4.2K. While high J_c values were achieved, all the high Ti content alloys were hard following precipitation heat treatments and the microstructures were very non-uniform. The exception to the non-uniform microstructures occurred in some wire which had been drawn to final size (ϵ_p= 12.6 compared to ϵ_p= 5 for standard processing) [2] before it received any heat treatment. Unfortunately, since the wire was already at final size it could not be given the cold work following heat treatment which is required to obtain high J_c. Finally, as had been noted before, the flux pinning curves ($F_p = J \times B$) shifted to lower field with increasing Ti content [16, 70].

The second major experiment in this study (increased prestrain experiment) was designed to test two increments in the cold work (ϵ_p= 8.3 and ϵ_p= 9.5) prior to heat treatment and still leave room following the heat treatment for enough additional cold work to obtain high J_c. Unfortunately, most of the wire in this experiment broke within a few dies of the final size. When tested at break size, the current densities were near $3000A/mm^2$ (5T, 4.2K). From a microstructural point of view this experiment was a success. Increas-

[2] The degrees of cold work are reported in true strain ($\epsilon = log_e(A_i/A_f)$). ϵ_p = the cold work since recrystallization and prior to heat treatment, ϵ_i = the cold work between heat treatments, ϵ_f = the cold work following the heat treatments, and ϵ_t = the total cold work since recrystallization.

ing the cold work prior to the first heat treatment caused the formation of uniform microstructures in both the Nb49wt%Ti alloy and the Nb53wt%Ti alloy. Quantitative analysis of the microstructures following the last precipitation heat treatment for these alloys showed that the percentage of precipitate following the precipitation heat treatments increased with increasing Ti content.

The third experiment was designed to produce similar microstructure in each of the alloys (isomorphology experiment) by varying the heat treatment temperature to keep the diffusion rate constant. In the previous experiments the results had shown that the microstructure varied with increasing Ti content. Thus, the goal of the third experiment was to keep the microstructure constant to test whether the change in the flux pinning properties with increasing Ti content was due to the change in microstructure or was due to the dominance of ΔH_c pinning, as proposed by Meingast and Larbalestier [62].

The major goals of these experiments were, first, to understand the way in which precipitate morphology depends on the alloy Ti content and the cold work prior to precipitation heat treatment. The second goal was to understand the processing of Nb-Ti alloys over a wide range of Ti content. The third major goal was to test the flux pinning hypothesis of Meingast and Larbalestier.

Chapter 2

Sample Preparation

The processing of samples in this study was by standard wire drawing methods. The Nb-Ti alloy was sheathed in Cu to allow the use of standard Cu wire drawing dies during the fabrication process. The Cu also acts as a stabilizer which keeps the wire from overheating during short sample testing. Prior to assembly, the Nb-Ti and the Cu tube were both etched to remove surface contamination. The etching bath for the Nb-Ti alloy was 15% HF, 35% HNO_3 and 50% H_2O and the bath for the Cu was 35% HNO_3 and 65% H_2O. The Nb-Ti rod was then slipped into the Cu tube and the end was swaged down to allow insertion into the wire drawing die. The wire was then drawn on a standard Cu 20% area reduction die schedule. Heat treatments were performed in laboratory size tube furnaces. When multifilamentary wire was desired, the wire was hexed between 0.125" and 0.079". This hexed wire was

then etched and stacked into a larger Cu tube for further reduction.

The Nb-Ti alloys for this study were specially ordered from Teledyne Wah Chang in Albany, Oregon (TWCA). TWCA was chosen as the supplier for the alloy because of its extensive experience with Nb46.5wt%Ti. Table 2.1 lists the alloys used in this study and their chemistries. Table 2.1 also lists the recrystallization anneal size, density, and homogeneity grade of the alloys. The bottom of table 2.1 lists the composites made from each alloy. As shown, each of the three major experiments in this study used a different batch of Nb46.5wt%Ti. Additionally, the Nb44wt%Ti and the Nb52wt%Ti alloys were not originally part of the study. The Nb44wt%Ti alloy was obtained midway through the increased prestrain experiment because it was unclear, from the existing data, whether the peak in H_{c_2} versus alloy composition occurred at Nb46.5wt%Ti or was lower in Ti content [27, 29]. It was reasoned that if the peak in H_{c_2} was actually near Nb44wt%Ti, an increase in J_c might be realized. As described in section 4.3, the expected result was not reached. It is believed that this is due to the extremely sluggish α -Ti precipitation in Nb44wt%Ti.

The densities listed in table 2.1 were used to calculate the copper to superconductor ratio for the wires in this study. These values were obtained by measuring the dimensions of the Nb-Ti rods at 0.280" and weighing the rods to calculate the density for all the high Ti alloys. The density value used for

Nb46.5wt%Ti is the standard value ($6.02 g/cm^3$). The value used for Nb44-wt%Ti ($6.06 g/cm^3$) was calculated using a random mixing approximation. Since the high Ti alloys were prone to ω formation which might change the density of the alloy, a careful set of density measurements was performed on three inch lengths of the alloy rods [75] and compared to densities computed from X-ray measurements on β-phase alloys [41]. The result of this comparison is shown in table 2.2. The agreement between the densities based on X-ray measurements and those measured on rods agree within a few parts in 500. Thus, ω formation did not affect the measured density values. The largest percent difference for the density values in table 2.2 is 2.6% for the Nb44wt%Ti alloy where the calculated density value was used rather than the measured density.

Following the conclusion of the prestrain experiment, it became obvious that the standard grade Nb53wt%Ti was causing difficulty in the microstructural measurements. The lack of chemical homogeneity in this standard grade made it almost impossible to find an area from which to get representative TEM information. Thus, a HiHo Nb52wt%Ti alloy was ordered to replace the standard grade Nb53wt%Ti alloy. As listed in table 2.1, the actual overall composition difference between these two alloys was only 0.1wt%Ti. The Nb52wt%Ti alloy arrived in time to be added to the isomorphology experiment (UW1719–UW3419). For the isomorphology experiment, a standard

grade Nb46.5wt%Ti alloy was inadvertently used. Fortunately, this standard grade alloy was homogeneous enough that consistent results were obtained with it.

2.1 Standard Experiment

The first major experiment in this study was the standard experiment in which monofilament wires were produced from the alloys using a processing schedule with heat treatments placed at the standard intervals for Nb46.5-wt%Ti. The strain space for this experiment was very similar to that available in large commercial wire processing. As shown in Figure 2.1 the heat treatments ranged in length from short (10 hours) to long (80 hours) and ranged in temperature from cool (375°C) to warm (435°C). Also included was a nonstandard process sequence of cold working to final size and heat treating at final size.

Several problems were encountered during the actual fabrication of samples from the experiment design shown in figure 2.1. The first problem was that the Nb46.5wt%Ti alloy used in this experiment was an experimental high homogeneity alloy which was designated HiHo[3]. Following the last anneal (at 1.448") the material had a duplex grain structure. 40% of the material had an ASTM grain size of #6 and 60% of the material had an

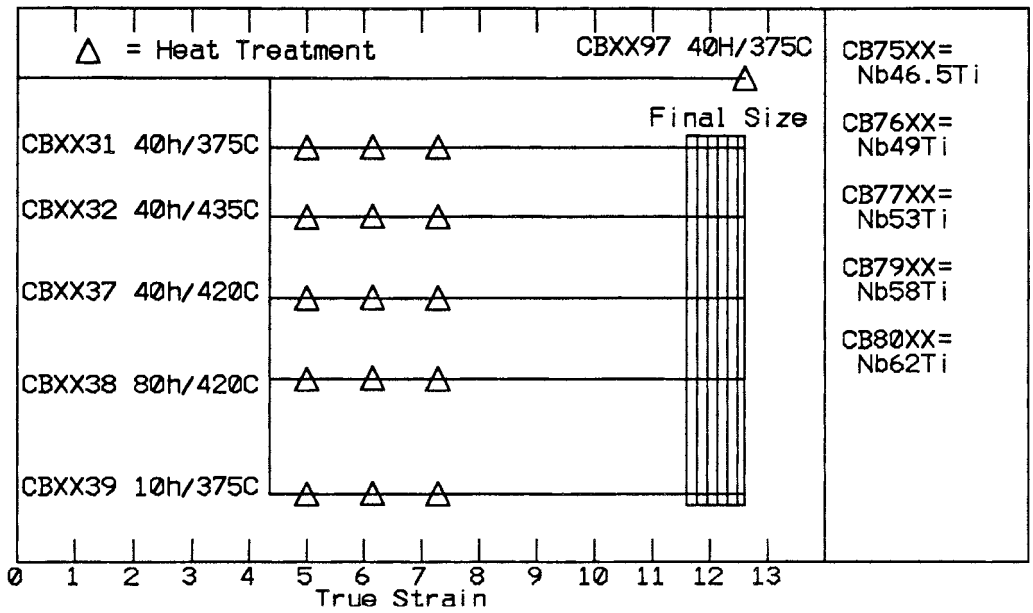

Figure 2.1: Processing sequence for the standard experiment. △ denotes a heat treatment of the time and temperature listed at the left. The X's denote variables. For example CB7737 is Nb53wt%Ti which received three 40 h, 420°C heat treatments.

ASTM grain size of #8. This variation in the grain size probably lowered the critical current density. The second problem was wire breakage during fabrication. For the standard process CB7931 (Nb58wt%Ti), CB8031 (Nb62wt%Ti), CB7939 (Nb58wt%Ti), and CB8039 (Nb62wt%Ti) could not be drawn to final size. In the final size heat treatment experiment CB7597 (Nb46.5wt%Ti) and CB8097 (Nb62wt%Ti) could not be drawn to final size. Since one of the wires which broke in this experiment was Nb46.5wt%Ti (CB7597) the breakage could not simply be attributed to the high hardness of the high Ti alloys. One possibility for the problems encountered during wire drawing was poor quality copper. Recent investigations have raised concern about the quality of the Cu tube available on the spot market due to the presence of porosity and cracks [31].

As described in section 4.3 the J_c results on those wires which could be drawn to final size were very encouraging. Unfortunately the microstructural results were not encouraging (see section 3). The precipitation obtained in all the alloys but Nb46.5wt%Ti was very uneven and greatly hardened the alloy. The exceptions were the samples receiving the large degree of cold work followed by a heat treatment at final size, which showed very uniform precipitation.

2.2 Increased Prestrain Experiment

The second major experiment in this study was the increased pre-strain experiment. In Nb46.5wt%Ti Buckett and Larbalestier had shown that increasing the prestrain from 2 to 5 reduced the appearance of hardening phases and increased the uniformity of the precipitation [7]. Similar behavior occurred in the standard experiment, where hardening phases occurred for alloys containing more than 47wt%Ti when ϵ_p= 5 but not when ϵ_p= 12.6. The increased prestrain experiment was performed to investigate the region between ϵ_p= 5 and ϵ_p= 12 and thus determine where the switch between precipitation of intragranular phases and the intergranular phases occurs for the high Ti alloys. The design of the increased prestrain experiment is shown in figure 2.2. As can be seen, two prestrains were tested in this experiment: ϵ_p=8.3 and ϵ_p=9.5. The increase in available strain space was achieved in two ways. To go from ϵ_p=5 in the standard experiment to ϵ_p= 8.3, a 19 filament wire was used rather than a monofilament. The second increment in ϵ_p from 8.3 to 9.5 was achieved by using only two heat treatments. The heat treatment selected for this experiment was 80 h/420°C which gave the best results in the standard experiment (see section 4.3). In an attempt to raise the J_c of the control wire the Nb46.5wt%Ti alloy used for this experiment was a HiHo grade.

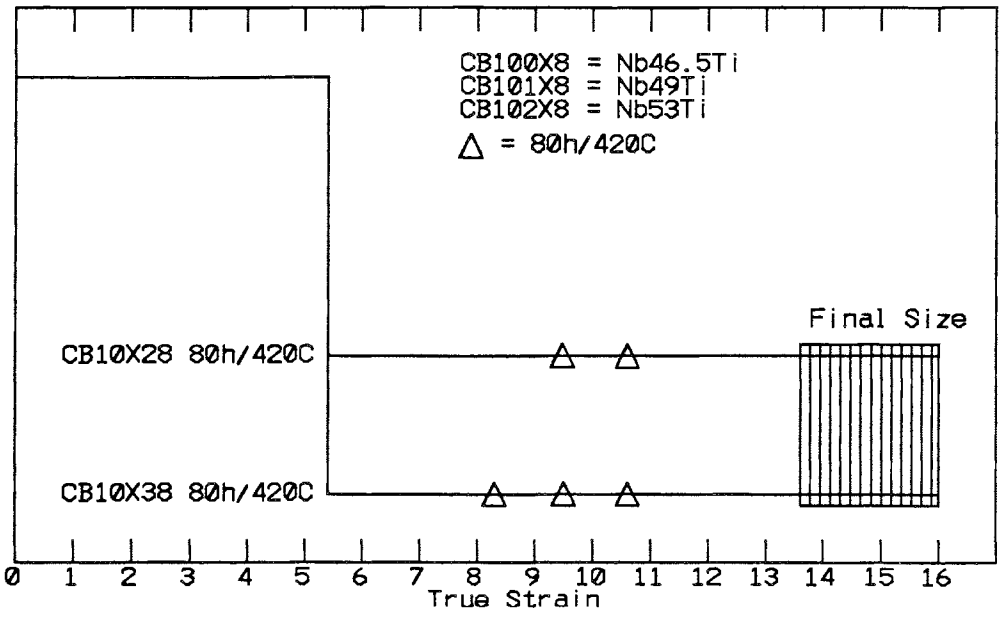

Figure 2.2: Processing sequence for the increased prestrain experiment.

Several problems were encountered during the fabrication of samples in this experiment. The first problem was a copper shortage. Due to the Cu shortage, Nb58wt%Ti and Nb62wt%Ti (CB104X8 and CB105X8) were never started. The second problem occurred near final size where most of the wire broke repeatedly during fabrication. CB10228 was the only wire to reach the final size of 0.0031". Table 2.3 lists the smallest size obtained for the rest of the wires from this experiment. As in the standard experiment, the breakage could not simply be attributed to the high Ti alloys since the control Nb46.5wt%Ti wire also broke.

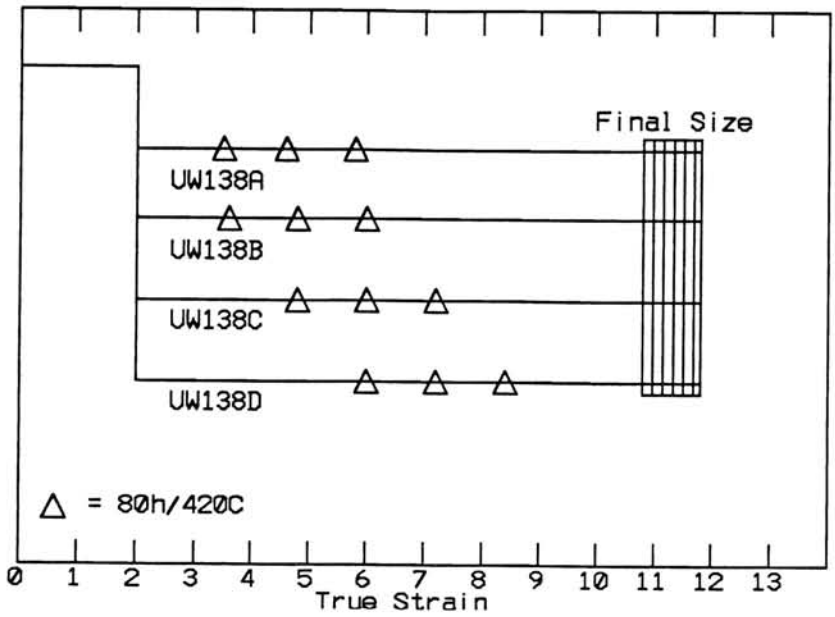

Figure 2.3: Processing sequence for the Nb44wt% Ti alloy standard experiment.

2.3 Minor Experiments

Following the completion of the increased prestrain experiment, the Nb44-wt%Ti alloy arrived. In order to test its behavior quickly, several monofilament wires were made. The design of these wires is shown in figure 2.3. The main variable in the design was the initial strain. Since the increased prestrain experiment had shown that alloys with Ti content higher than Nb46.5wt%Ti required additional strain prior to heat treatment, (see section 3.3) this experiment was designed to see if alloys with Ti content lower than Nb46.5wt%Ti required less initial strain.

All of the wires from this experiment processed to final size well. The

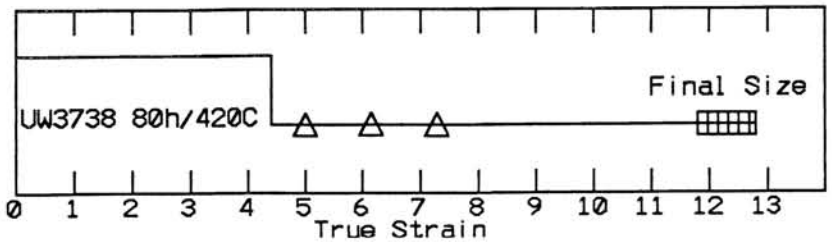

Figure 2.4: Processing sequence for the Nb52wt% Ti alloy standard experiment.

microstructural results showed no signs of the hardening intragranular precipitation with the reduced strain. However, the wire receiving a standard processing sequence (UW138C) had only 10vol% of α -Ti precipitate following three heat treatments compared to 20vol% for Nb46.5wt%Ti alloys [44]. The J_c results for Nb44wt%Ti were also low (see section 4.3).

As described in section 2 above, following the conclusion of the increased prestrain experiment a HiHo Nb52wt%Ti alloys was ordered to replace the standard grade Nb53wt%Ti alloy. Upon receiving the Nb52wt%Ti alloy, a wire was made using a standard heat treatment sequence to bench mark the new alloy against the other alloys. The design of the monofilament wire in this bench marking experiment is shown in figure 2.4. The wire was readily fabricated to final size and the J_c results were respectable (>3000 A/mm^2 at 5T, 4.2K).

2.4 Isomorphology Experiment

The final experiment performed on this set of alloys was the isomorphology experiment. The flux pinning results from the previous experiments in this study and other studies [70, 83] showed that the flux pinning properties changed considerably as the overall Ti content of the alloys changed (see section 5.1). Also observed in the previous experiments of this study was a large variation in microstructure as the overall Ti content changed (see chapter 3). Thus it seemed plausible that the change in the flux pinning properties was a direct result of the changing microstructure. However, Meingast and Larbalestier had proposed that the large variation in the pinning properties of Nb-Ti alloys containing about 60wt%Ti was due to changes in the elementary pinning mechanism (see section 1.1). The purpose of the isomorphology experiment was to test this hypothesis by fabricating wires across the alloy range with microstructures as similar as possible.

In order to achieve a constant microstructure across the alloy range, two things were done. First, a large degree of initial cold work (ϵ_p= 11.8) was given the alloys to insure that precipitation would occur in the grain boundaries. Second, the heat treatment temperature was varied for each alloy in an attempt to keep the precipitation rate constant and in turn keep the percentage of precipitate constant across the alloy range. The first approach to

varying the heat treatment temperature was to calculate the temperatures for each alloy keeping the ratio of the heat treatment temperature to the melting temperature (T/T_m) constant. The base for this calculation was Nb46.5wt%Ti at 375°C for which T/T_m=.301. The values used for the melting point were taken from the solidus of the phase diagram by Hansen et al. (see section 1.2) [25]. As listed in table 2.4, the heat treatment temperatures calculated by this method were often separated by less than 5°C. This is not a large change in the heat treatment temperature from alloy to alloy and is on the order of the uncertainty in the overall furnace temperature. Thus, an alternative approach was sought.

The alternative approach to varying the heat treatment temperature was to maintain a constant diffusion rate across the alloy range. The use of a constant rate of diffusion for the precipitation heat treatments should give relatively uniform precipitation in materials when the precipitation is diffusion limited. This appears to be the case in Nb-Ti because several heat treatments separated by cold work are needed to obtain a high percentage of α -Ti precipitate. For the Nb-Ti system, the majority of the data available is for Nb diffusing in Nb-Ti (which is slower than Ti diffusing in Nb-Ti). Moffat has summarized the diffusion data for Nb in Nb-Ti and finds:

$$D = D_0 e^{\left(\frac{-Q}{RT}\right)} \quad (cm^2/sec) \tag{2.1}$$

$$D_0 = 5.5783 \times 10^{-4} e^{(8.209x)} \ \ (cm^2/sec) \tag{2.2}$$

$$Q = 31463 + 65674x \ \ (cal/mol) \tag{2.3}$$

where x is the atomic fraction of Nb [63].

Pontau and Lazarus made the only known report for the diffusion of Ti in Nb-Ti alloys [74]. Their data for Ti diffusing in Nb-Ti may be modeled with:

$$D_0 = 10^{(3.5515+0.07611x)} \ \ (cm^2/sec) \tag{2.4}$$

$$Q = 29768 + 798.9x \ \ (cal/mol) \tag{2.5}$$

However, the validity of Pontau and Lazarus' data for Ti diffusing in Nb-Ti is placed in question by their D_0 values for Nb diffusion in Nb-Ti which do not agree well with other studies [1, 17, 52, 71, 72, 74, 76]. Additionally, the values obtained by Pontau and Lazarus do not agree well with other reports of Ti diffusion in Nb and Ti diffusion in Ti [78, 82]. Even so, as shown in table 2.5, the two sets of equations 2.2-2.3 and 2.4-2.5 yield comparable heat treatment temperatures. The temperatures resulting from the Nb diffusion in Nb-Ti calculations were used for the isomorphology experiment.

The wire geometry selected for the isomorphology experiment was a 61 filament conductor which allowed a total true strain for the experiment of approximately 16. This allowed ϵ_p =11.8 for the experiment with remaining available strain of 4 following the heat treatment. Based on the microstruc-

tural results of the previous experiments (see section 3.7), ϵ_p=11.8 would be high enough to insure uniform precipitation in Nb44wt%Ti to Nb58wt%Ti but Nb62wt%Ti would likely be subject to precipitation of hardening phases. The projection of the precipitation of hardening phases in Nb62wt%Ti was confirmed during fabrication. Following the heat treatment the Nb62wt%-Ti wire was too brittle to draw and work hardened to breakage simply by bending the wire. A second unheat-treated piece of the Nb62wt%Ti wire was then drawn to an initial final strain of approximately 15 and given the same heat treatment. At this stage, the Nb62wt%Ti was ductile following heat treatment. Figure 2.5 shows the processing sequence for the isomorphology experiment. As shown, samples were taken for J_c testing following heat treatment and at increments of one in strain there after.

The processing of the isomorphology wires went well. The only break encountered was the Nb62wt%Ti wire (UW1819) following heat treatment as mentioned above. The other minor problem encountered during this experiment was an oscillation in furnace temperature (caused by the controller) of $\pm$5°C at 337°C and 342°C (UW2319 and UW3419) with a period of about 10 minutes. The microstructural results of this processing were good, although as shown in section 3.7, the term isomorphology is somewhat a misnomer.

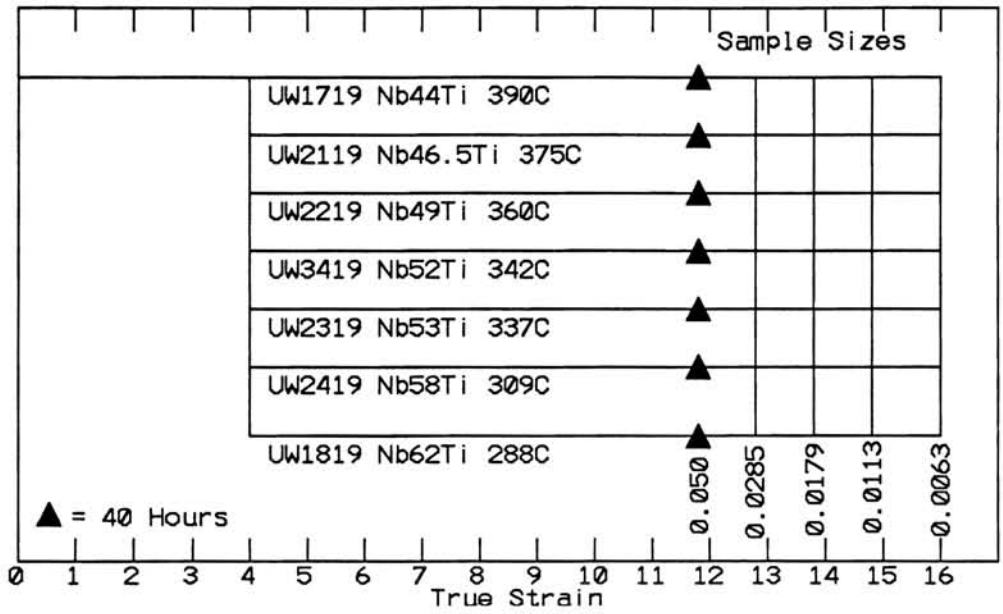

Figure 2.5: Processing sequence for the isomorphology experiment.

Table 2.1: The Chemistry, Grade, Density, and Billet identification for the Alloys used in this study. Compositions are in wt%Ti, densities (ρ) are in g/cm^3, the recrystallization anneal size is in inches, and impurities are in ppm.

Nom.	Nb44Ti	Nb46.5Ti			Nb50Ti	Nb52Ti	Nb54Ti	Nb58Ti	Nb62Ti
Ref.	Nb44Ti	Nb46.5Ti			Nb49Ti	Nb52Ti	Nb53Ti	Nb58Ti	Nb62Ti
Ti	43.5	46.4	46.8	46.5	49.3	52.4	52.5	57.8	62.3
Anneal	1.625"	1.5"	1.5"	1.5"	1.5"	1.620"	1.5"	1.5"	1.5"
$\rho(g/cc)$	6.06	6.02	6.02	6.02	5.96	5.77	5.85	5.67	5.52
Grade	HiHo	HiHo[3]	HiHo	Std	HiHo	HiHo	Std	HiHo	HiHo
Al	<25	<25	<25	<25	<25	<25	<25	<25	30
C	40	40	35	30	40	34	40	50	60
Cr	<50	28	<50	25	<50	<50	<50	<50	<50
Cu	12	<10	<10	<10	11	<10	11	45	12
Fe	<50	67	51	58	<50	<50	<50	74	92
H	16	13	<5	32	20	<5	28	21	48
N	23	63	23	42	8	30	16	20	8
Ni	<25	<25	<25	<25	<25	<25	<25	<25	<25
O	690	720	735	660	590	608	630	680	620
Si	<100	<100	<100	<100	<100	<100	<100	<100	<100
Sn	<40	<40	<40	<40	<40	<40	<40	<40	<40
Ta	1310	330	915	320	680	982	550	540	520
Wires	UW138x	CB75xx	CB100xx	UW2119	CB76xx CB101xx UW2219	UW3738 UW3419	CB77xx CB102xx UW2319	CB79xx UW2419	CB80xx UW1819
	UW1719								

Table 2.2: A comparison of the density values used to calculate copper to superconductor ratios, the densities calculated from X-ray measurements, and the densities measured on 0.280" diameter rods.

Alloy	Used in this Study (g/cm^3)	X-ray [41] (g/cm^3)	Measured 36" Rod (g/cm^3)	Measured [75] 3" Rod (g/cm^3)
Nb43.5wt%Ti	6.06	6.18	6.22	—
Nb46.4wt%Ti	6.02	6.05	—	6.04
Nb46.8wt%Ti	6.02	6.05	—	—
Nb46.5wt%Ti	6.02	6.05	—	—
Nb49.3wt%Ti	5.96	5.93	5.96	5.91
Nb52.4wt%Ti	5.77	5.83	5.77	—
Nb52.5wt%Ti	5.85	5.83	5.85	5.82
Nb57.8wt%Ti	5.67	5.63	5.67	5.61
Nb62.3wt%Ti	5.52	5.48	5.52	5.46

Table 2.3: Wire breakage sizes for the increased prestrain experiment. Only CB10228 reached design size.

Wire ID	Alloy	Diameter (in)	Strain Since Last Heat Treatment (ϵ_f)
CB10038	Nb46.5wt%Ti	0.0063	3.93
CB10138	Nb49wt%Ti	0.0063	3.93
CB10238	Nb53wt%Ti	0.0079	3.44
CB10028	Nb46.5wt%Ti	0.005	4.42
CB10128	Nb49wt%Ti	0.010	3.04
CB10228	Nb53wt%Ti	0.0031	5.36

Table 2.4: Heat treatment temperatures for a constant T/T_m. Based on Nb46.5wt% Ti at 375°C.

wt% Ti	T_m (K)	T_{HT} (K)	T_{HT} (C)
44	2167	652	379
46.5	2152	652	379
49	2136	643	370
52	2131	641	368
53	2118	637	364
58	2090	629	356
62	2067	622	349

Table 2.5: Heat treatment temperatures based on keeping the diffusion rates for Nb and Ti constant in Nb-Ti. The baseline for this calculation was Nb46.5wt% Ti at 375°C.

wt% Ti	Nb in Nb-Ti[63]	Ti in Nb-Ti[74]
44	390°C	390°C
46.5	375°C	375°C
49	360°C	360°C
52	342°C	343°C
53	337°C	338°C
58	309°C	310°C
62	288°C	288°C

Chapter 3

Microstructure

The microstructural results from the alloys in this study contain a wealth of information. Two types of microstructural measurements were used to obtain information about the microstructures: transmission electron microscopy (TEM) and Vicker's hardness. The results from these two measurement techniques complimented each other well in this study.

The TEM for this study was performed by Dr. Peter Lee using a JOEL 200CX TEM/STEM. Samples were prepared for TEM analysis as follows. First the outside diameter of the wire was modified to $3mm$ by etching the copper away on the large monofilaments, or by plating copper onto the finer wires. Transverse cross sections of the wire were cut using a diamond saw. These sections were ground down until they were $100\mu m$ thick. Further thinning of the specimens was performed using a Fischione jet electropolishing

apparatus with a solution of 2vol% HF, 5vol% H_2SO_4 and 93vol% Methanol. The polishing conditions were 223K, 50mA, and 45V. Ion milling was performed on selected specimens as needed.

Quantitative analysis of the TEM micrographs was performed by Dr. Lee using a MegaVision image processing system[45]. In TEM measurements the α and β phases are distinguished primarily by their atomic number difference. However, due to the texture formed during wire drawing, diffraction often occurs which reduces the contrast in portions of the α -Ti precipitates. Using the MegaVision system micrographs of the same region, but at different tilts could be combined to enhance the contrast between the α -Ti precipitates and the surrounding β phase. The images were acquired from back lit TEM negatives using the MegaVision high resolution video camera. Images on the MegaVision are 1024 X 1024 pixels. This resolution is high enough that its quality approaches that of a photographic image and little essential information was lost.

The Vicker's hardness measurements for this study were made on transverse cross-sections of wire which had been mounted in 1" diameter phenolic pucks and polished optically smooth. The measurements were made using a LECO M-400 hardness tester using a mass of 200 gm.

3.1 Microstructural Results from the Standard Heat Treatment Experiment

The microstructures obtained in the standard experiment were all non-uniform following the first heat treatment. This non-uniformity had two different forms: varying β grain size and varying precipitate morphology. The hardness measured on this material also had two major trends. The hardness stayed approximately constant through heat treatments which produced α -Ti precipitates along the grain boundary. The second trend was a large jump in hardness during the first heat treatment for specimens exhibiting intragranular precipitation. The TEM for this experiment was done on a limited number of specimens due to the complexity of sample preparation.

3.1.1 Nb46wt%Ti - CB753X

The Nb46.5wt%Ti wire selected for TEM after the first heat treatment was CB7531. Following the first heat treatment, the grain size of this wire varied considerably as shown in figure 3.1. The precipitation was composed of two types of α -Ti in the grain boundaries. In some regions the grains were separated by a distinct grain boundary film of α -Ti. Other regions had developed full α -Ti precipitates in the grain boundaries. There were no obvious regions of intragranular precipitation in this wire. The large variation in grain size in this material is probably due to its being of HiHo[3] quality.

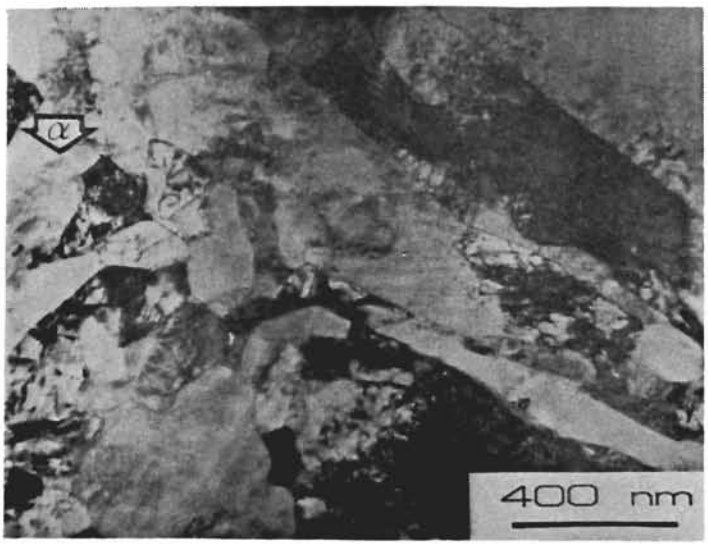

Figure 3.1: TEM micrograph of a Nb46.5wt%Ti (CB7531 0.144") transverse cross section following the first heat treatment of 40h at 375°C, $\epsilon_p = 5.02$ (courtesy of Dr. Peter Lee). The marker indicates the grain boundary film precipitate.

Lee and Larbalestier have shown that a HiHo material produces a much more uniform grain size following the first anneal [43].

The results of the hardness measurements on the Nb46.5wt%Ti wires are shown in figure 3.2. The hardness for this alloy increased only slightly during heat treatment with the longer, hotter heat treatments showing the smallest increase in hardness during the precipitation heat treatments. A slight trend toward higher hardness with increasing total strain was observed in the Nb46.5wt%Ti wires.

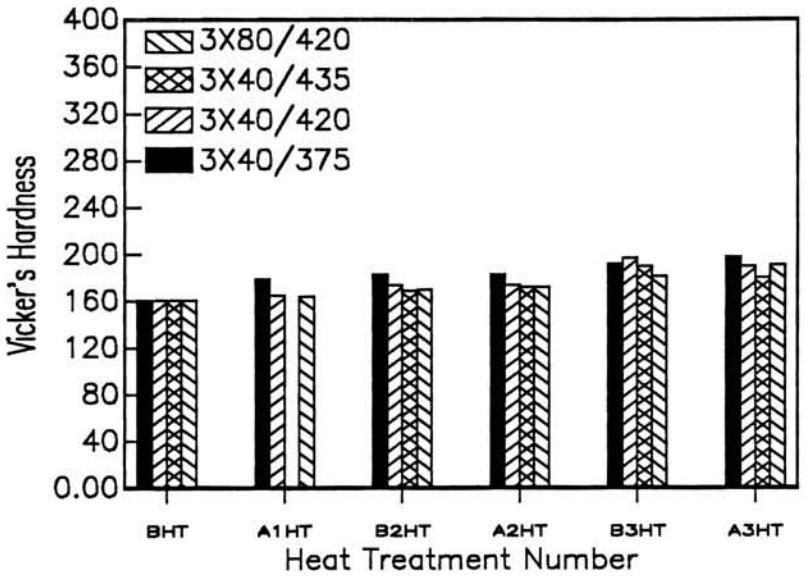

Figure 3.2: Vicker's hardness as a function of processing stage and heat treatment for Nb46.5wt%Ti (ϵ_p = 5.02). CB7531=3X40/375, CB7532=3X40/435, CB7537=3X40/420, CB7538=3X80/420. BHT and AHT denote before and after heat treatment respectively.

3.1.2 Nb49wt%Ti - CB763X

The Nb49wt%Ti wires of the standard experiment exhibited very inhomogeneous precipitation behavior. Following one heat treatment of 40h/375°C three different forms of precipitation were present (figure 3.3). The first form of precipitation was large equiaxed intergranular α -Ti precipitation. The second form of precipitation present was intragranular ω which appears in the form of dark ellipsoids. The third form of precipitation present was intragranular α -Ti which has a needle-like morphology. Increasing the heat treatment temperature to 420°C coarsened the intragranular α -Ti precipitation and ω was no longer visible (figure 3.4). The overall microstructure was still inhomogeneous. Lower magnification micrographs showed large intergranular α -Ti precipitates [46].

The hardness measurements reflect the hardening effect of the intragranular precipitates. Figure 3.5 shows the large jump in hardness which occurred during the first precipitation heat treatment for these two microstructures. As can be seen, the longer, hotter heat treatments produced wires which were softer following the heat treatment than the wires receiving the cooler, shorter heat treatments.

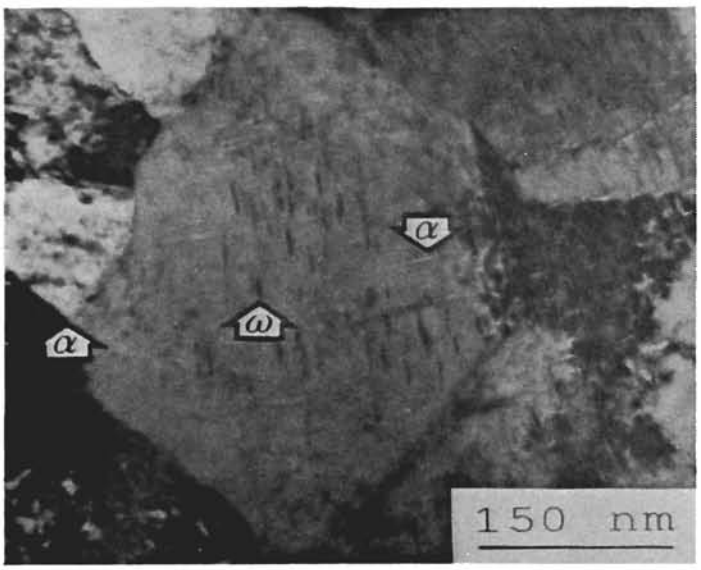

Figure 3.3: TEM micrograph of a Nb49wt%Ti (CB7631 0.144") transverse cross section following the first heat treatment of 40h at 375°C, $\epsilon_p = 5.02$ (courtesy of Dr. Peter Lee).

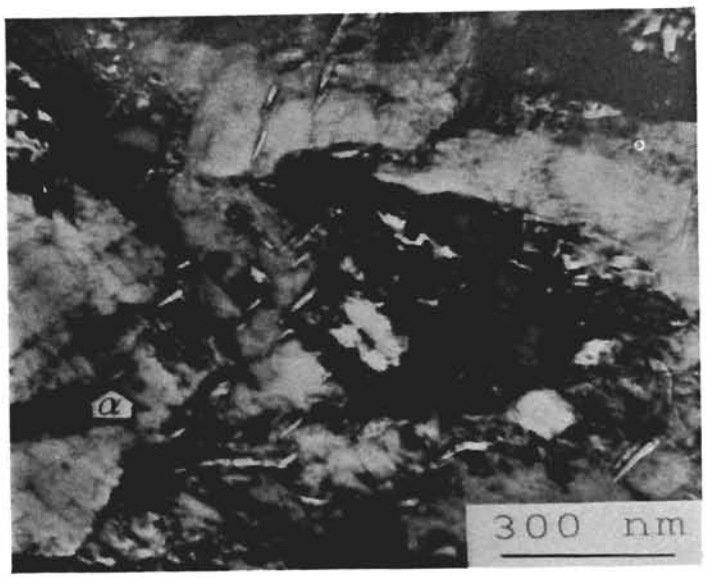

Figure 3.4: TEM micrograph of a Nb49wt%Ti (CB7637 0.144") transverse cross section following the first heat treatment of 40h at 420°C, $\epsilon_p = 5.02$ (courtesy of Dr. Peter Lee).

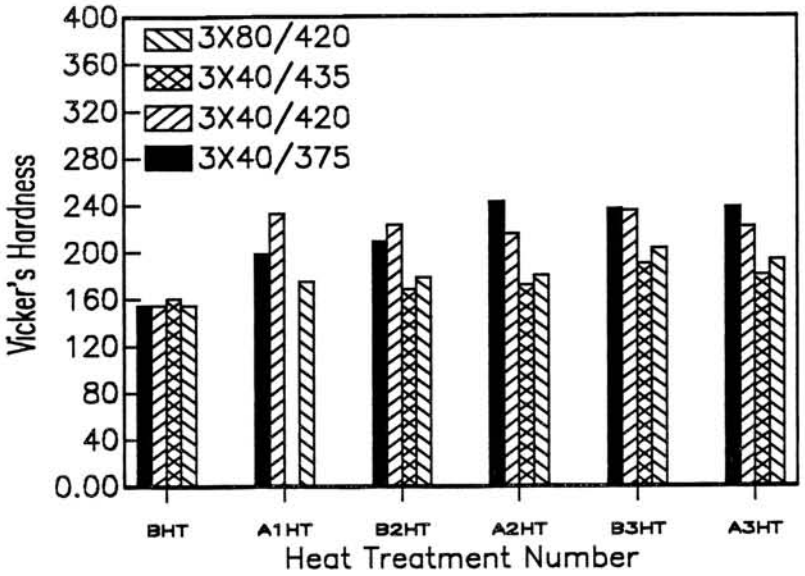

Figure 3.5: Vicker's hardness as a function of processing stage and heat treatment for Nb49wt%Ti (ϵ_p = 5.02). CB7631=3X40/375, CB7632=3X40/435, CB7637=3X40/420, CB7638=3X80/420.

3.1.3 Nb53wt%Ti - CB773X

The Nb53wt%Ti wires also exhibited very inhomogeneous precipitation. CB7731 had many needle-like precipitates, typical of Widmanstätten precipitation (see figure 3.6). Lower magnification micrographs showed a large variation in the β-Nb-Ti grain size (d_{eff} = 60nm- 800nm). Also present were large intergranular α -Ti precipitates. The microstructure resulting from the 40h/420°C heat treatment was very similar to the microstructure obtained with the 40h/375°C heat treatment (figure 3.7).

The hardness values showed large jumps during the initial heat treatment (see figure 3.8). Unfortunately, the samples for hardness measurements for

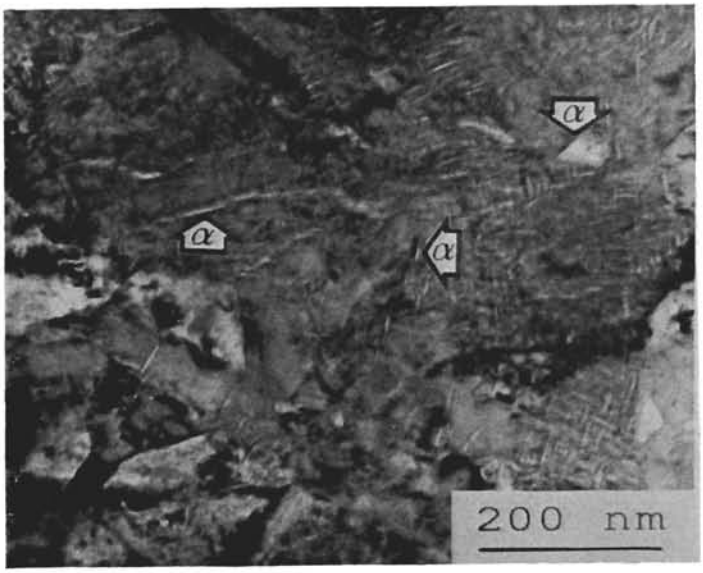

Figure 3.6: TEM micrograph of a Nb53wt%Ti (CB7731 0.144") transverse cross section following the first heat treatment of 40h at 375°C, $\epsilon_p = 5.02$ (courtesy of Dr. Peter Lee).

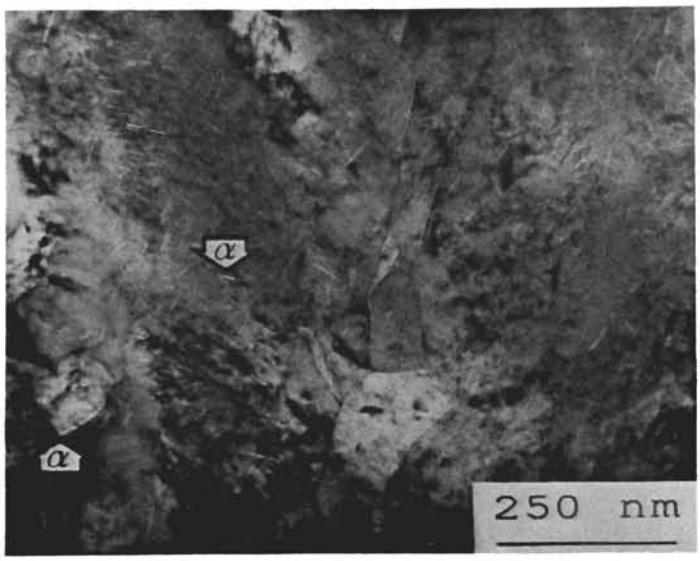

Figure 3.7: TEM micrograph of a Nb53wt%Ti (CB7737 0.144") transverse cross section following the first heat treatment of 40h at 420°C, $\epsilon_p = 5.02$ (courtesy of Dr. Peter Lee).

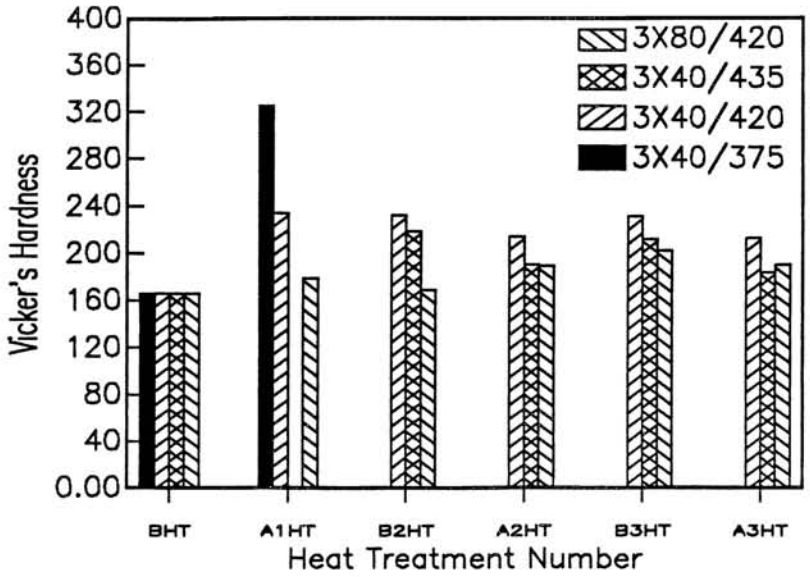

Figure 3.8: Vicker's hardness as a function of processing stage and heat treatment for Nb53wt%Ti (ϵ_p = 5.02). CB7731=3X40/375, CB7732=3X40/435, CB7737=3X40/420, CB7738=3X80/420.

CB7731 were not taken below .144". However, the rest of the wires show substantial increases in hardness between their initial cold drawn state and the hardness following the last heat treatment.

3.1.4 Nb58wt%Ti - CB793X

The microstructure of Nb58wt%Ti was even more inhomogeneous than the microstructure of the lower titanium alloys. Figure 3.9 shows the microstructure for CB7931 which received a 40h/375° C heat treatment. There is a large variation in the precipitate size shown in this micrograph. Also, the interface between the fine α -Ti precipitate and the β grains lacks definition (the

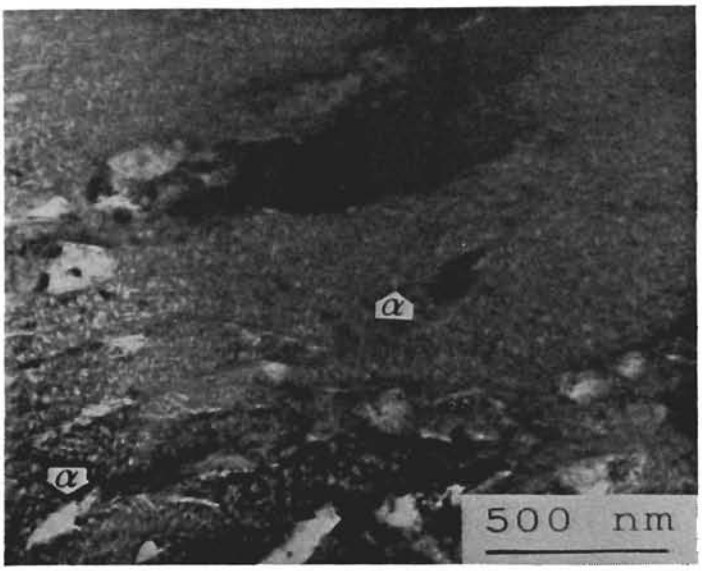

Figure 3.9: TEM micrograph of a Nb58wt%Ti (CB7931 0.144") transverse cross section following the first heat treatment of 40h at 375°C, $\epsilon_p = 5.02$ (courtesy of Dr. Peter Lee).

interface is not sharp, which probably indicates that the precipitates are thinner than the TEM foil thickness). The definition of the fine α -Ti improves considerably when the heat treatment temperature is increased from 375°C to 420°C (figure 3.10). Much of the α -Ti precipitate in figure 3.10 is very needle-like although there are also many grain boundary precipitates and equiaxed precipitates as well. The fraction of precipitate is also substantially higher than that in Nb49wt%Ti. (figure 3.4).

The hardness increase during the first heat treatment for Nb58wt%Ti was very large. (see figure 3.11). The large increase in hardness during the first precipitate anneal was followed, in general, by a subsequent decrease in

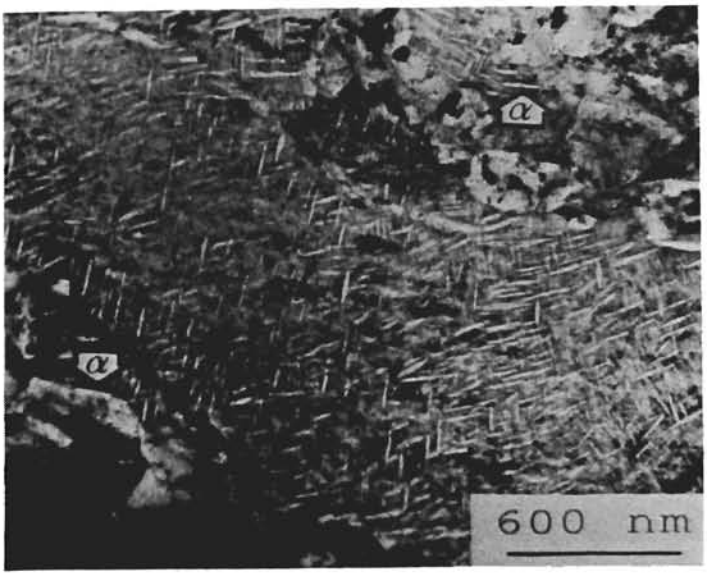

Figure 3.10: TEM micrograph of a Nb58wt%Ti (CB7937 0.144") transverse cross section following the first heat treatment of 40h at 420°C, $\epsilon_p = 5.02$ (courtesy of Dr. Peter Lee).

hardness for each subsequent step in the processing. The final hardness of the wires following the last precipitation heat treatment was higher than any of the lower Ti content wires.

3.1.5 Nb62wt%Ti - CB803X

The microstructural results for Nb62wt%Ti were much like those for Nb58-wt%Ti. Fine intragranular precipitation occurred for the cool (40h/375°C) heat treatment (figure 3.12) and again had poor definition at the interface between the α -Ti and the β. Also present were very large equiaxed α -Ti precipitates. The precipitation for the hotter heat treatment (40h/420°C)

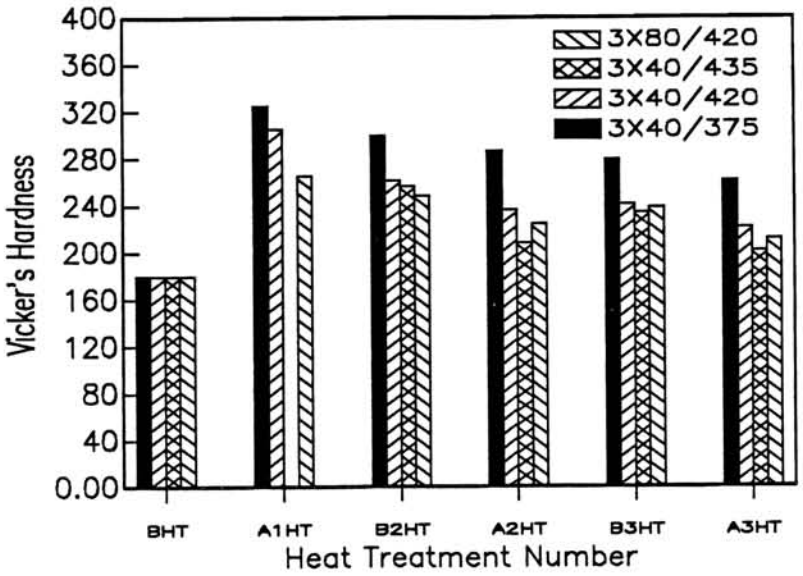

Figure 3.11: Vicker's hardness as a function of processing stage and heat treatment for Nb58wt%Ti (ϵ_p = 5.02). CB7931=3X40/375, CB7932=3X40/435, CB7937=3X40/420, CB7938=3X80/420.

was dense and showed signs of coarsening (see figure 3.13). Also present were some very long grain boundary precipitates and some equiaxed precipitates.

The hardness results for Nb62wt%Ti are shown in figure 3.14. As was the case for the Nb58wt%Ti wires, the hardness jumped substantially during the first heat treatment. Unlike Nb58wt%Ti, the subsequent cold working and heat treating procedures exhibited a more standard trend of increasing hardness during cold work and decreasing hardness during annealing.

3.2 Standard Experiment: Final Size Heat Treatments

The TEM results from the wires receiving final size heat treatments were

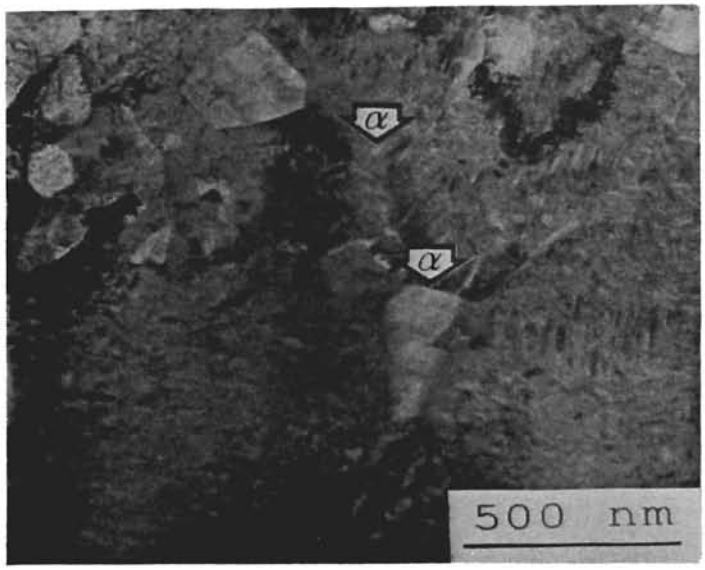

Figure 3.12: TEM micrograph of a Nb62wt%Ti (CB8031 0.144") transverse cross section following the first heat treatment of 40h at 375°C, $\epsilon_p = 5.02$ (courtesy of Dr. Peter Lee).

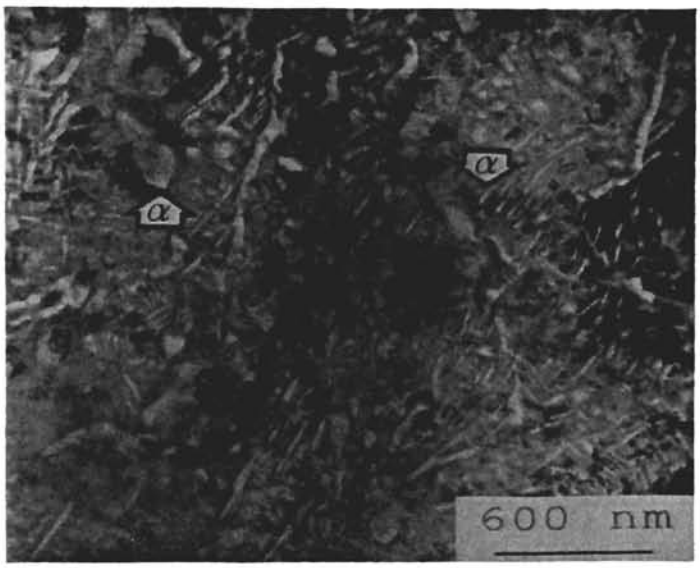

Figure 3.13: TEM micrograph of a Nb62wt%Ti (CB8037 0.144") transverse cross section following the first heat treatment of 40h at 420°C, $\epsilon_p = 5.02$ (courtesy of Dr. Peter Lee).

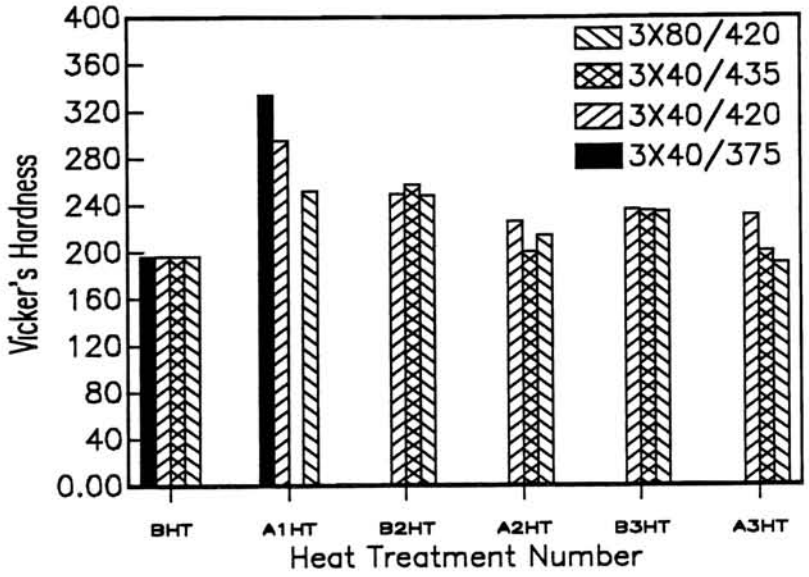

Figure 3.14: Vicker's hardness as a function of processing stage and heat treatment for Nb62wt%Ti (ϵ_p = 5.02). CB8031=3X40/375, CB8032=3X40/435, CB8037=3X40/375, CB8038=3X80/420.

very different from those receiving the standard heat treatments. All of the TEM results showed uniform precipitation in these wires, as can be seen in figures 3.15 to 3.17. All of the micrographs for these samples show α -Ti precipitates in the grain boundary triple points. These microstructures are very different from those shown in figures 3.3 to 3.10.

The major difference between the wires receiving the final size heat treatments and the standard wires was the cold work prior to heat treatment. For the standard heat treatments the prestrain was 5. This is considerably lower than the prestrain of 12.6 received by the final size heat treatment wires. Thus increasing the prestrain suppressed the intragranular precipita-

3.3.1 CB10X38: ϵ_p= 8.3

The microstructural results for the wires receiving an initial prestrain of 8.3 are shown in figures 3.18 to 3.20. The Nb46.5wt%Ti wire (CB10038) exhibited very even grain boundary triple point precipitation and fairly uniform grain size. Note that the Nb46.5wt%Ti alloy used in this experiment was HiHo rather than the HiHo[3] used in the first experiment. Thus, not all the microstructural refinement seen in figure 3.18 compared to figure 3.1 was due to the increased initial strain. The microstructure for NB49wt%Ti (CB10138) was also fairly uniform. Although the photographic quality is poor, the β grain size varied by about a factor of two and the α -Ti precipitation occurred in the grain boundary triple points. Figure 3.20 shows that Nb53wt%Ti (CB10238) still contained a great deal of intragranular precipitation. In addition to the intragranular precipitation, a large amount of intergranular precipitation was also present. Thus, ϵ_p= 8.3 was not sufficient to suppress intragranular precipitation in Nb53wt%Ti.

The hardness values from these wires correlated well with the microstructures observed (see figure 3.21). CB10038 and CB10138 both had constant hardness through the first heat treatment. But CB10238 (Nb53wt%Ti), which had the intragranular precipitation, showed an increase in hardness during the first heat treatment.

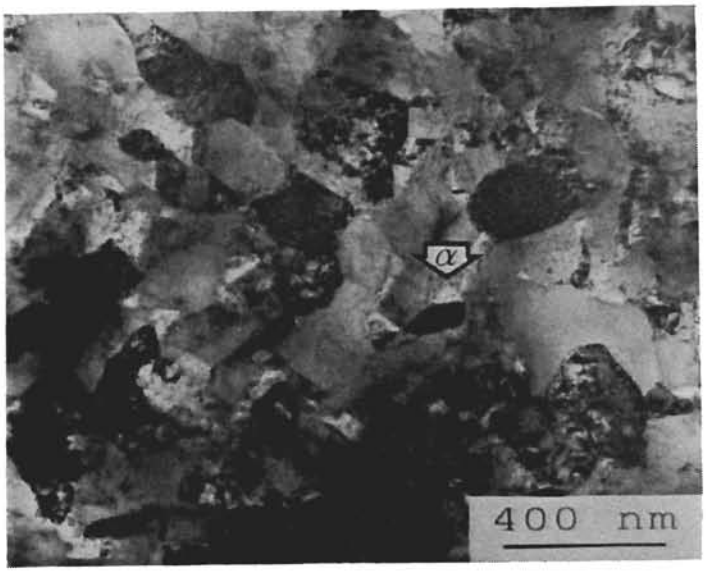

Figure 3.18: TEM micrograph of a Nb46.5wt%Ti (CB10038 0.144") transverse cross section following one heat treatment of 80h at 420°C, $\epsilon_p = 8.3$ (courtesy of Dr. Peter Lee).

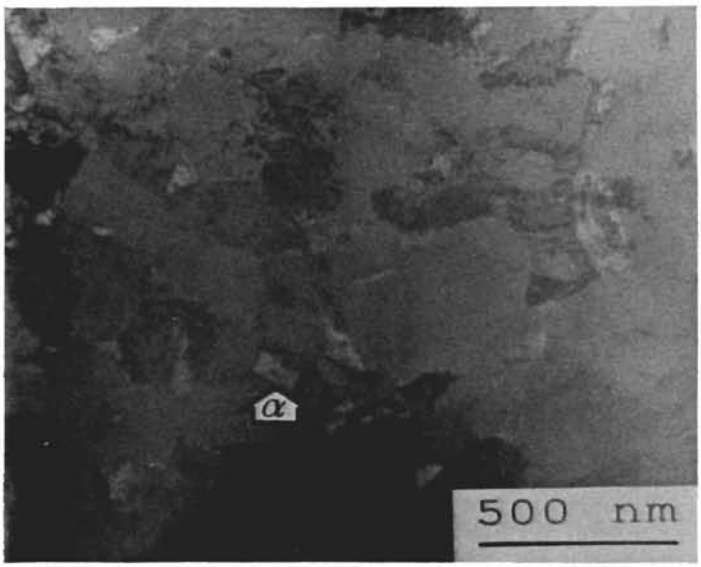

Figure 3.19: TEM micrograph of a Nb49wt%Ti (CB10138 0.144") transverse cross section following one heat treatment of 80h at 420°C, $\epsilon_p = 8.3$ (courtesy of Dr. Peter Lee).

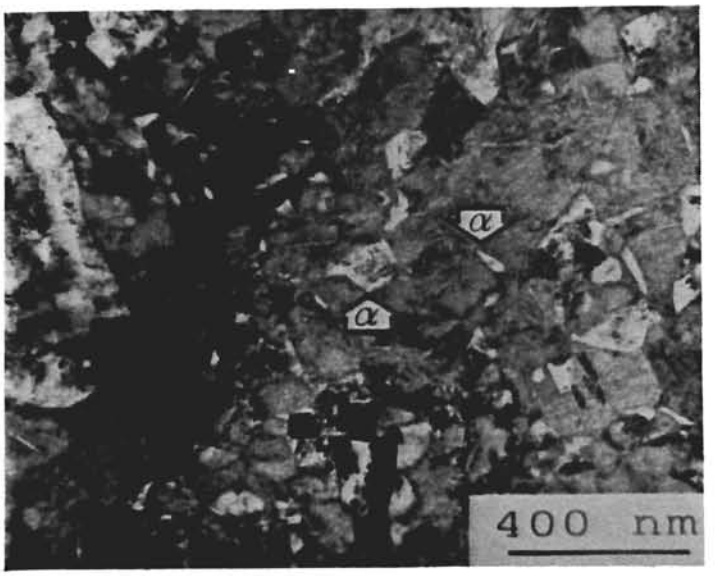

Figure 3.20: TEM micrograph of a Nb53wt%Ti (CB10238 0.144") transverse cross section following one heat treatment of 80h at 420°C, $\epsilon_p = 8.3$ (courtesy of Dr. Peter Lee).

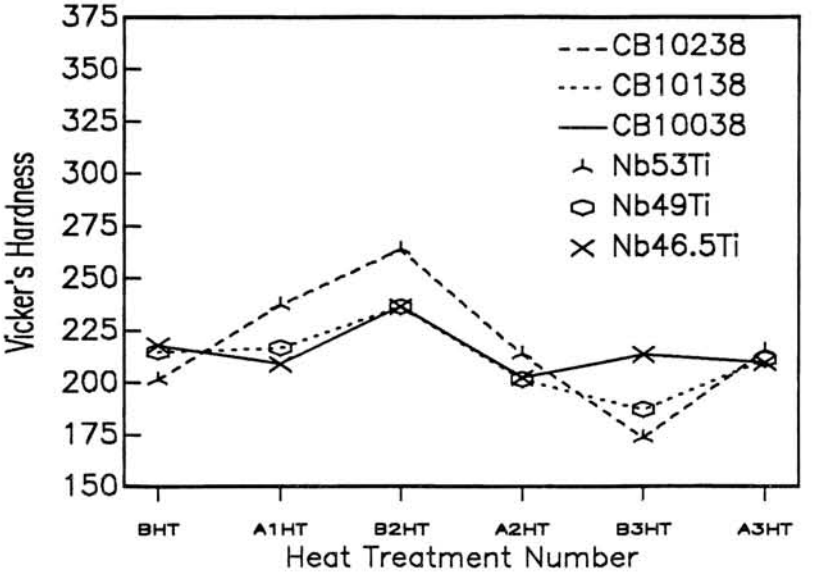

Figure 3.21: Vicker's hardness as a function of processing stage and alloy for 80h, 420°C heat treatments ($\epsilon_p = 8.3$).

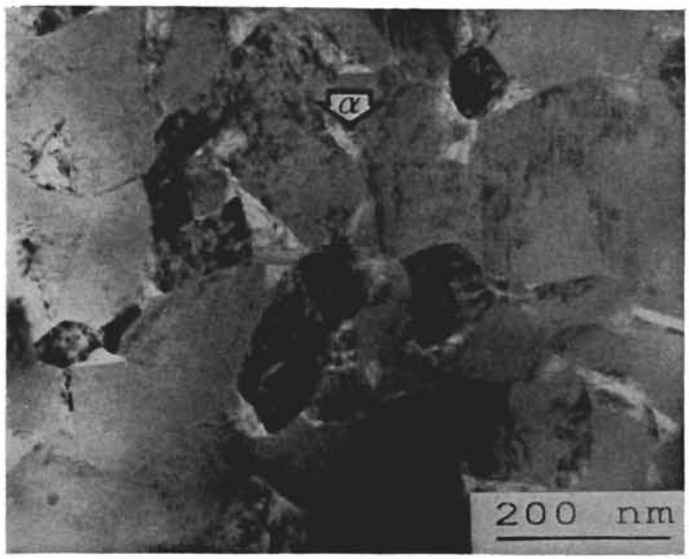

Figure 3.22: TEM micrograph of a Nb46.5wt%Ti (CB10028 0.080") transverse cross section following one heat treatment of 80h at 420°C, ϵ_p = 9.5 (courtesy of Dr. Peter Lee).

3.3.2 CB10X28 : ϵ_p=9.5

With the prestrain increased to 9.5, Nb46.5wt%Ti, Nb49wt%Ti and Nb53-wt%Ti all exhibited uniform microstructures. As can be seen in figures 3.22 to 3.24, all three alloys had α -Ti precipitation in the grain boundary triple points. In addition the β-Nb-Ti grain size was fairly uniform.

The hardness results from these three wires were all essentially flat as shown in figure 3.25. This is quite an improvement over the hardness results for Nb49wt%Ti and Nb53wt%Ti shown in figures 3.5 and 3.8 respectively.

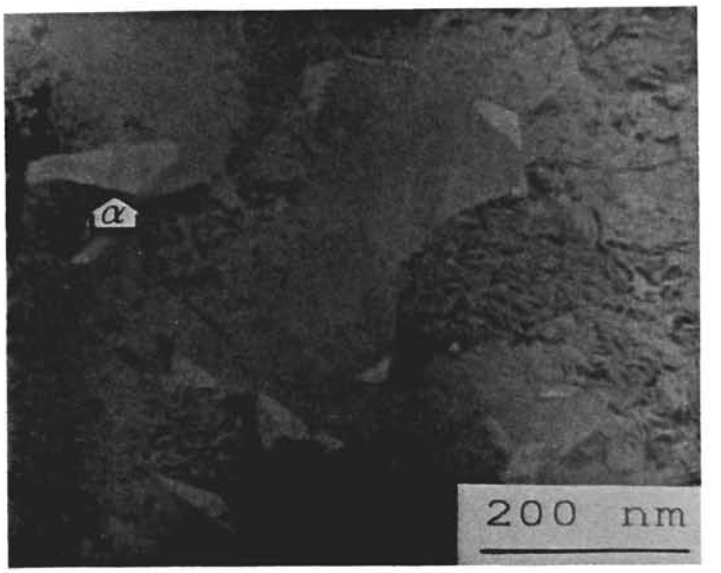

Figure 3.23: TEM micrograph of a Nb49wt%Ti (CB10128 0.080") transverse cross section following one heat treatment of 80h at 420°C, $\epsilon_p = 9.5$ (courtesy of Dr. Peter Lee).

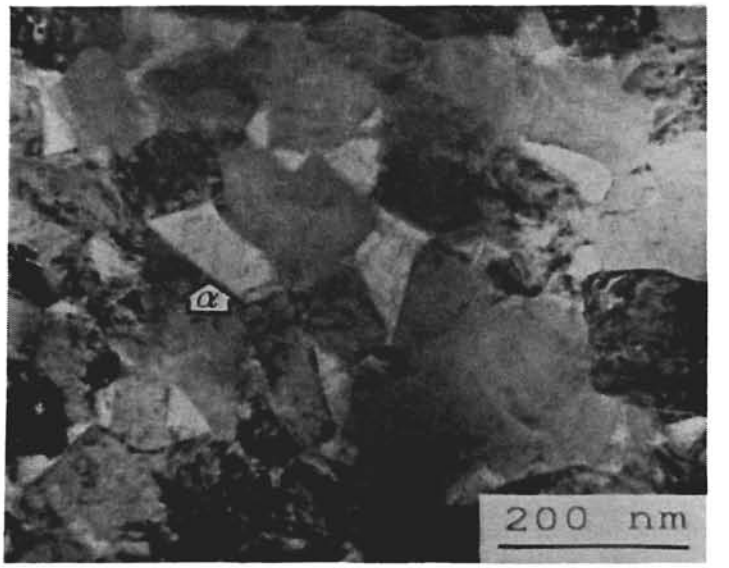

Figure 3.24: TEM micrograph of a Nb53wt%Ti (CB10228 0.080") transverse cross section following one heat treatment of 80h at 420°C, $\epsilon_p = 9.5$ (courtesy of Dr. Peter Lee).

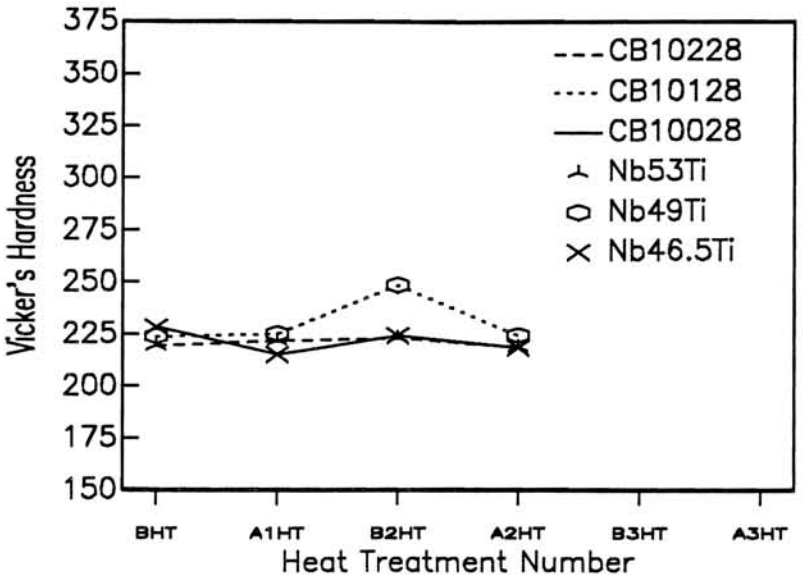

Figure 3.25: Vicker's hardness as a function of processing stage and alloy for 80h, 420°C heat treatments ($\epsilon_p = 9.5$).

3.4 The Effect of Multiple Heat Treatments and Further Cold Work

A limited amount of work has been done on the microstructures resulting from further processing in these materials. Figure 3.26 shows the microstructure of CB7638 (Nb49wt%Ti) following the last of three heat treatments. This microstructure was considerably more regular than that of CB7637 (see figure 3.4) following the first heat treatment, but there was still a large variation in the precipitate size. Some intragranular α -Ti precipitation was still present, but had coarsened since the first heat treatment.

Another example of homogenization of the microstructure with further

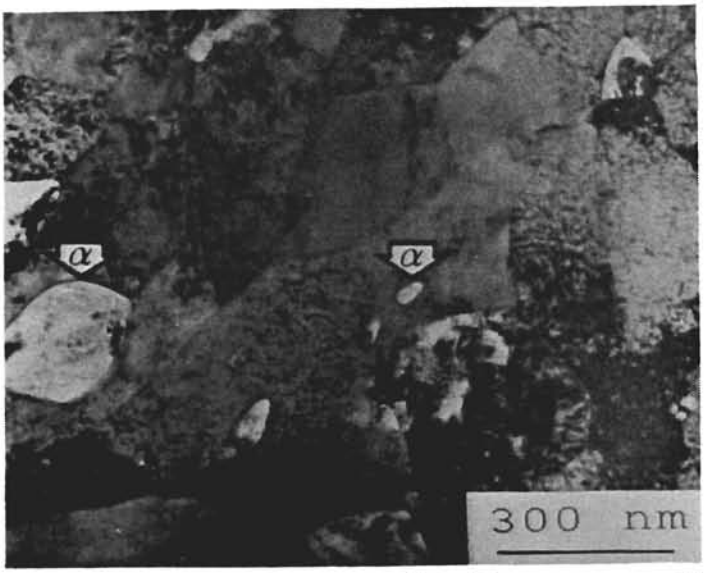

Figure 3.26: TEM micrograph of a Nb49wt%Ti (CB7638 0.0453") transverse cross section following three heat treatments of 80h at 420°C, ϵ_p = 5.02, ϵ_i = 1.15 (courtesy of Dr. Peter Lee).

processing can be seen by comparing CB10238 (Nb53wt%Ti) at 0.0453" following the last heat treatment (figure 3.27) with CB10238 at .144" following the first heat treatment (figure 3.20). As in the case of CB7638, the α -Ti precipitates following the final heat treatment were equiaxed, whether they were intergranular or intragranular. However, both CB7638 and CB10238 had a large variation in the precipitate size following the last heat treatment.

CB7938 (NB58wt%Ti) was not nearly as uniform following three heat treatments as CB7638 was. This can be seen by comparing figures 3.26 and 3.28. In this case, the large variation in precipitation which occurred during the first heat treatment was still quite evident following further thermo-

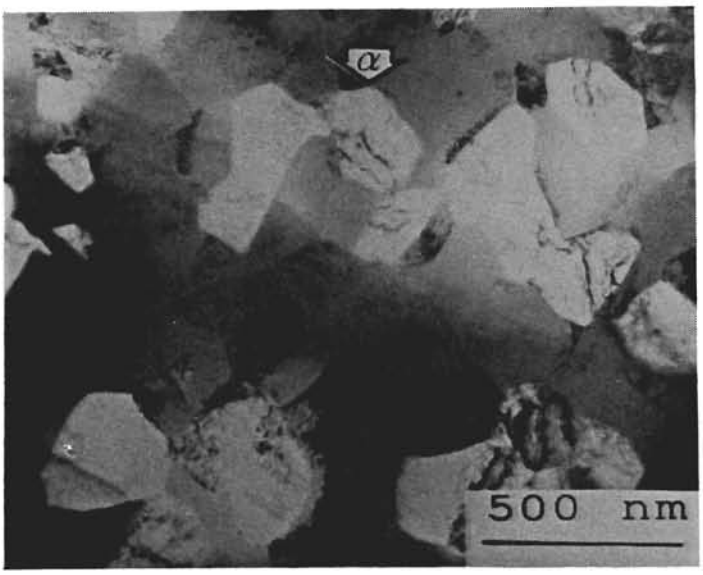

Figure 3.27: TEM micrograph of a Nb53wt%Ti (CB10238 0.0453") transverse cross section following three heat treatments of 80h at 420°C, $\epsilon_p = 8.3$, $\epsilon_i = 1.15$ (courtesy of Dr. Peter Lee).

mechanical processing. The effect of the large variation in precipitate morphology following the last heat treatment on the final microstructure ribbon morphology can be seen in figure 3.29. Overall this microstructure was similar to the high J_c microstructures for Nb46.5wt%Ti reported by Lee and Larbalestier [42, 43, 44]. But in this case the ribbon thickness was very nonuniform, ranging from $\sim 3\ nm$ thick to $15\ nm$ thick. This could explain the extremely broad peak in J_c with final drawing strain shown in figure 4.10.

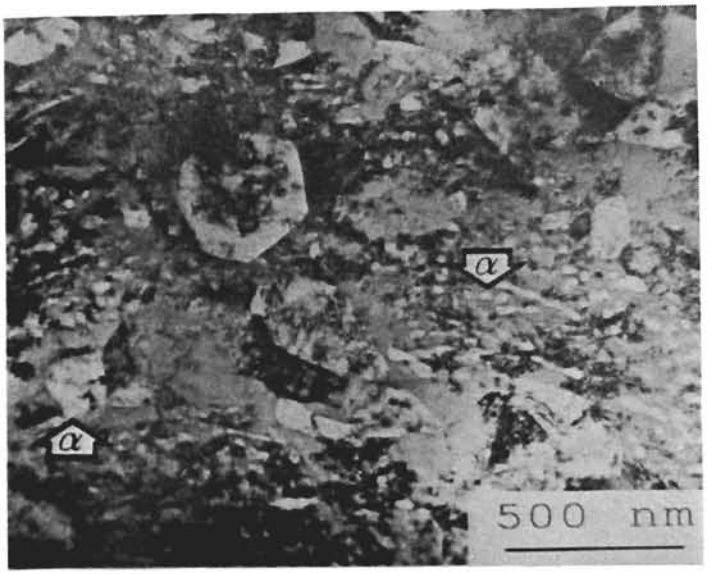

Figure 3.28: TEM micrograph of a Nb58wt%Ti (CB7938 0.0453") transverse cross section following three heat treatments of 80h at 420°C, ϵ_p = 5.02, ϵ_i = 1.15 (courtesy of Dr. Peter Lee).

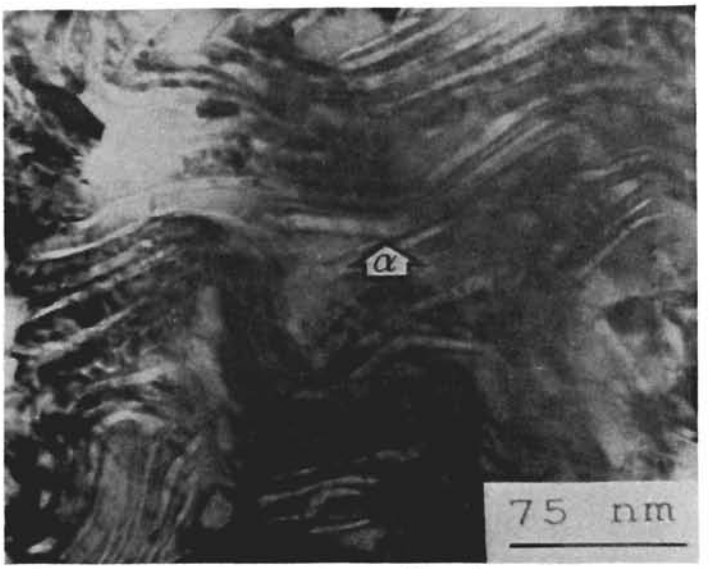

Figure 3.29: TEM micrograph of a Nb58wt%Ti (CB7938 0.0056") transverse cross section which received three heat treatments of 80h at 420°C and further cold work, ϵ_p = 5.02, ϵ_i = 1.15, ϵ_f = 4.18 (courtesy of Dr. Peter Lee).

3.5 Nb44wt%Ti: Standard Processing Results

Based on the need for increasing prestrain with increasing Ti content seen in the first two experiments, microstructural results were obtained on two parts of the standard experiment for Nb44wt%Ti. The first wire (UW138A) received its first heat treatment at 0.280" (ϵ_p=3.5) which was the size Nb-Ti rod delivered by TWCA. The second wire (UW138C) received a heat treatment after a more standard initial cold worked state (ϵ_p=5). The results of the heat treatment on bare Nb44wt%Ti rod are shown in figure 3.30. The microstructure of this wire was free from the needle-like intergranular precipitation found in the higher Ti alloys. However, due to the low level of ϵ_p dislocations were present and are not uniformly distributed throughout the β grains. There was very little α -Ti precipitate present following the 80h/420°C heat treatment and there were no signs of intragranular precipitation.

UW138C received a more standard processing sequence. Following the last heat treatment, the microstructure of Nb44wt%Ti was fairly homogenous (figure 3.31). The α -Ti precipitation formed in the grain boundary triple points. The microstructure is similar to CB7638 after three heat treatments (figure 3.26) but there was substantially less precipitate present in UW138C

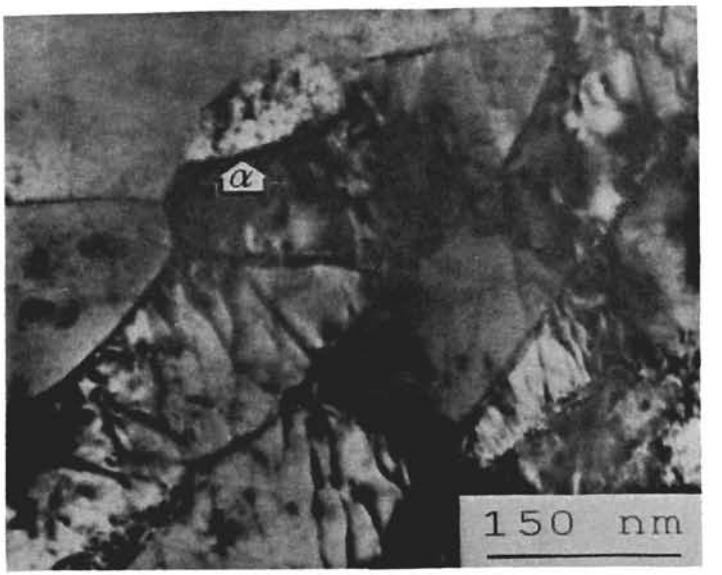

Figure 3.30: TEM micrograph of a Nb44wt%Ti (UW138A 0.280") transverse cross section after one heat treatment of 80h at 420°C, $\epsilon_p = 3.5$ (courtesy of Dr. Peter Lee).

than was present in CB7638.

3.6 α -Ti Precipitate Fraction Following the Precipitation Heat Treatments

As discussed in section 3.3.2, a limited number of wires were examined microstructurally following the last heat treatment. Table 3.1 lists the wires which were examined and the fraction of α -Ti precipitate present in these alloys, as determined by image analysis using the MegaVision. The information in this table is limited and has some scatter, but the trend toward an increasing α -Ti percentage with increasing Ti content is clear. With the increase in the α -Ti percentage there is a corresponding change in the

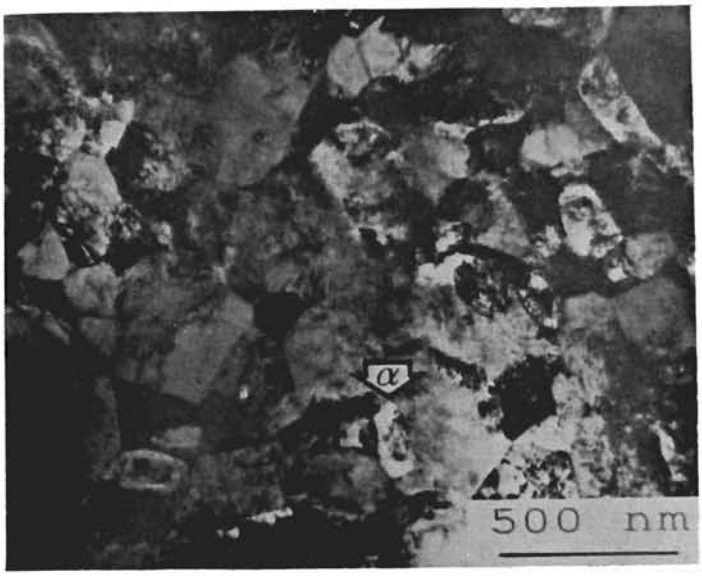

Figure 3.31: TEM micrograph of a Nb44wt%Ti (UW138C 0.050") transverse cross section following three heat treatments of 80h at 420°C, $\epsilon_p = 5$, $\epsilon_i = 1.15$ (courtesy of Dr. Peter Lee).

electromagnetic properties. As shown in section 5.1, the peak in the pinning force curve shifted to lower field with increasing Ti content. This posed the question: is the observed difference in pinning simply due to the large difference observed in the microstructures, or was it due to the actual overall difference in alloy composition? Thus an experiment was performed which attempted to keep the percentage of α -Ti as constant as possible. This experiment is the isomorphology experiment.

Table 3.1: Percentage of α -Ti precipitate present following the last heat treatment for wires from the standard experiments and the increased pre-strain experiment (courtesy of Dr. Peter Lee).

Wire ID	ϵ_p	Heat Treatment	Alloy wt%Ti	%α-Ti	Average Area $(nm)^2$
UW138C	5	3X80/420	44	10	25950
CB7638	5	3X80/420	49	14.9	20400
CB7937	5	3X40/420	58	40.2	12638
CB10038	8.3	3X80/420	46.5	20.9	36781
CB10138	8.3	3X80/420	49	34	20866
CB10238	8.3	3X80/420	53	27.9	41191
CB10028	9.5	2X80/420	46.5	14.8	5904
CB10128	9.5	2X80/420	49	20.1	18562
CB10228	9.5	2X80/420	53	25.9	54333

3.7 Isomorphology Experiment: Results

As will be shown in this section, the term isomorphology for this experiment is not strictly correct. The microstructures obtained were similar, but not identical, across the alloy range from Nb44wt%Ti to Nb58wt%Ti. As discussed in the sample preparation chapter, the total available strain space was limited and uniform precipitation was not expected to occur in Nb62wt%Ti.

Most of the micrographs shown for this experiment are the images which were used for image analysis. A comparison of an image on a TEM negative and an image used for image analysis is shown in figures 3.32 - 3.34. Most of the precipitation for this wire appeared in the form of a thick (5 nm) grain boundary film. The MegaVision images from a different region

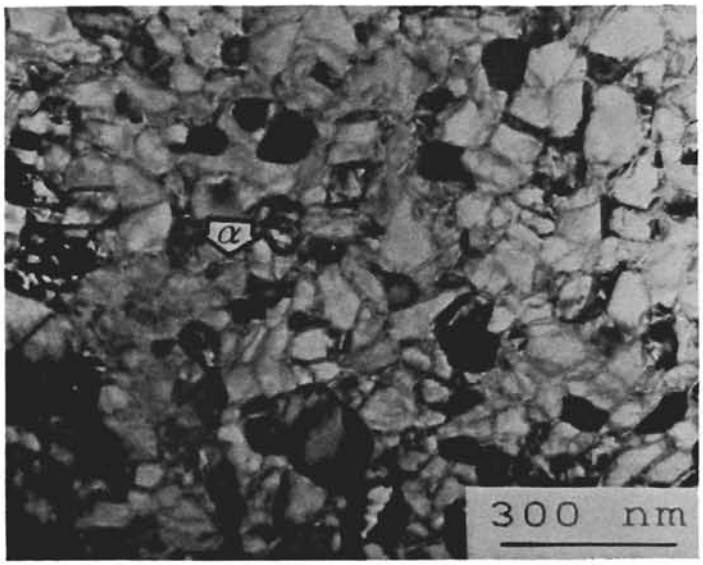

Figure 3.32: TEM micrograph of a Nb44wt%Ti (UW1719 0.050") transverse cross section after one heat treatment of 40h at 390°C, $\epsilon_p = 11.8$ (courtesy of Dr. Peter Lee).

of UW1719 (Nb44wt%Ti) show a very similar microstructure. Figure 3.33 shows a MegaVision image of UW1719 ready for processing to highlight the α -Ti precipitates. Figure 3.34 shows the results of processing to highlight the α -Ti precipitates. The highlighted precipitates were then used for analysis of the α -Ti fraction. The analysis on the rest of the wires in this experiment was performed in a similar fashion.

The precipitate morphology of UW1719 differs considerably from the rest of the wires in this study. The α -Ti precipitate for UW1719 occurred primarily in the form of a thick (5 nm) grain boundary film. The precipitate morphology for Nb46.5wt%Ti to Nb58wt%Ti wires was primarily grain

Figure 3.36: TEM micrograph, as acquired for image analysis, of a Nb49wt%Ti (UW2219 0.050") transverse cross section after one heat treatment of 40h at 360°C, $\epsilon_p = 11.8$ (courtesy of Dr. Peter Lee).

Figure 3.37: TEM micrograph, as acquired for image analysis, of a Nb52wt%Ti (UW3419 0.050") transverse cross section after one heat treatment of 40h at 342°C, $\epsilon_p = 11.8$ (courtesy of Dr. Peter Lee).

Figure 3.38: TEM micrograph, as acquired for image analysis, of a Nb53wt%Ti (UW2319 0.050") transverse cross section after one heat treatment of 40h at 337°C, $\epsilon_p = 11.8$ (courtesy of Dr. Peter Lee).

Figure 3.39: TEM micrograph, as acquired for image analysis, of a Nb58wt%Ti (UW2419 0.050") transverse cross section after one heat treatment of 40h at 309°C, $\epsilon_p = 11.8$ (courtesy of Dr. Peter Lee).

Table 3.2: Percentage of α -Ti precipitate present following the last heat treatment for the isomorphology experiment (courtesy of Dr. Peter Lee).

Wire ID	Alloy wt%Ti	Heat Treatment	%α-Ti	Average Area $(nm)^2$
UW1719	44	40/390	3.61	219
UW2119	46.5	40/375	7.65	408
UW2219	49	40/360	11.2	721
UW3419	52	40/342	14.8	255
UW2319	53	40/337	8.9	439
UW2419	58	40/309	11.6	488
UW1819	62	40/288	15.5	1775

heat treatment had been raised relative to the rest of the wires in the experiment, because sluggish precipitation had already been observed in UW138C at 420°C.

The maximum amount of precipitate for this experiment occurred in Nb62wt%Ti (figure 3.40). As described in chapter 2 on sample preparation, the cold work provided in this experiment was not expected to be enough to suppress intragranular precipitation. Although there was no evidence of intragranular precipitation for UW1819 (Nb62wt%Ti), the precipitation observed was very unusual. The precipitates are large and equiaxed with irregular interfaces with the β-Nb-Ti grains. This microstructural morphology resulted in wire so brittle that it could not even be pulled back through the same die used prior to heat treatment.

The microstructure of all the wires was on a fine scale following the heat

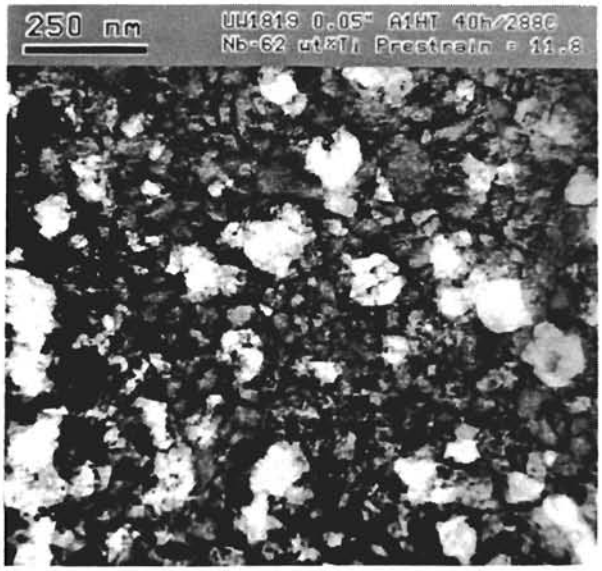

Figure 3.40: TEM micrograph, as acquired for image analysis, of a Nb62wt%Ti (UW1819 0.050") transverse cross section after one heat treatment of 40h at 288°C, $\epsilon_p = 11.8$ (courtesy of Dr. Peter Lee).

treatment (effective precipitate diameter (d^*) of about $12nm$ compared to the more typical value of $d^* \approx 80nm$ for CB7638 following three heat treatments) and refined quickly with further cold work. Figures 3.41 and 3.42 show the effect of giving UW2119 (Nb46.5wt%Ti) and UW2219 (Nb49wt%Ti) a strain of 2 following heat treatment. Following the cold work, the α -Ti precipitates were already very fine (most of the α -Ti was $\approx$1 nm thick, with occasional thicknesses as large as 10 nm) but are not the classic ribbon morphology normally seen in Nb-Ti alloys [44, 61]. An additional strain of 2 for UW2119 (Nb46.5wt%Ti) yielded a microstructure so fine that no α -Ti precipitate can be unambiguously identified in the TEM micrograph (figure 3.43). However,

Figure 3.41: TEM micrograph of a Nb46.5wt%Ti (UW2119 0.0179") transverse cross section after one heat treatment of 40h at 375°C and cold work ($\epsilon_p = 11.8$, $\epsilon_f = 2.05$ (courtesy of Dr. Peter Lee).

the diffraction pattern showed evidence for the presence of some α -Ti.

3.8 Initial Cold Work Needed to Obtain Grain Boundary Precipitation

It has been shown in this study that it is possible to suppress the hardening intergranular precipitation in Nb-Ti alloys by increasing the initial cold work prior to heat treatment. Figure 3.44 shows the relationship between the prestrain needed to suppress hard intragranular precipitation and the alloy content [47, 48]. All the points on this graph except the two highest strain points for Nb62wt%Ti are based on TEM micrographs. The two high strain

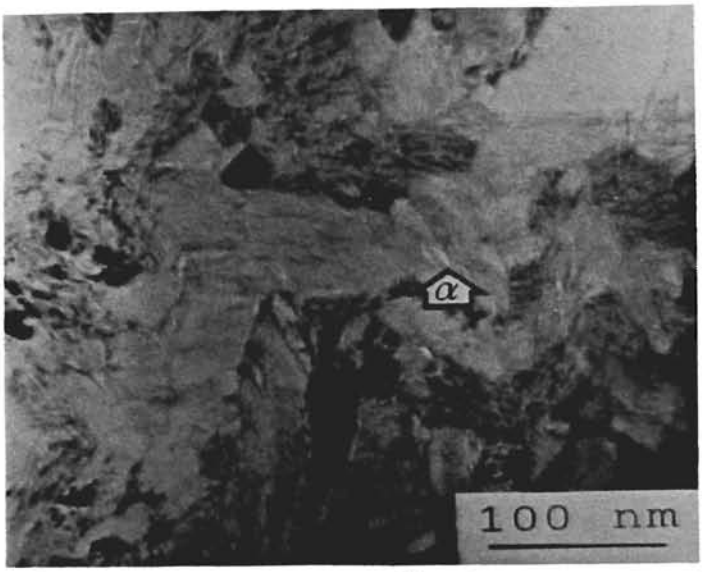

Figure 3.42: TEM micrograph of a Nb49wt%Ti (UW2219 0.0179") transverse cross section after one heat treatment of 40h at 360°C and cold work (ϵ_p = 11.8, ϵ_f = 2.05 (courtesy of Dr. Peter Lee).

Figure 3.43: TEM micrograph of a Nb46.5wt%Ti (UW2119 0.0063") transverse cross section after one heat treatment of 40h at 375°C and cold work (ϵ_p = 11.8, ϵ_f = 4.14 (courtesy of Dr. Peter Lee).

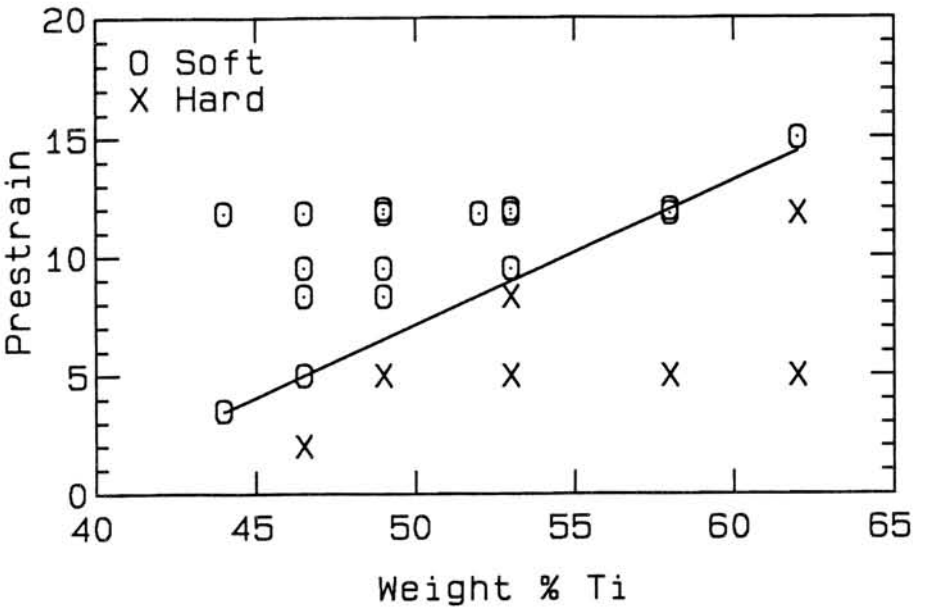

Figure 3.44: The prestrain (ϵ_p) required to suppress the hardening fine intragranular precipitation versus the Ti content of the initial alloy.

Nb62wt%Ti points are from the drawing behavior described in section 2.4. There are two primary pieces of information that can be obtained from this graph. First, if a new Nb-Ti binary alloy is used, one can get an estimate of how much cold work to provide prior to heat treatment. Second, this graph shows the importance of alloy homogeneity. If an alloy is inhomogeneous, some regions of the alloy may not receive enough cold work to suppress the hardening intragranular precipitation which can provoke mechanical instabilities during further mechanical deformation.

3.9 Summary

The microstructural results yielded a wealth of information about the alloy system. In the standard experiment (ϵ_p=5), only Nb46.5wt%Ti showed the desired grain boundary triple point α -Ti precipitation. The rest of the alloys showed non-uniform precipitate morphologies and size distributions, with both Widmanstätten α-Ti and ω precipitation present. The exception to the inhomogeneous precipitation was the set of wires receiving a large initial strain (ϵ_p=12.6) and a single heat treatment at final size. All of the final size heat treatment wires had uniform grain boundary triple point α -Ti precipitation. The results of the increased prestrain experiment showed that increasing the initial cold work to a strain of 8.3 was sufficient to suppress intragranular precipitation in Nb49wt%Ti and in Nb53wt%Ti a prestrain of 9.5 was sufficient.

The hardness measurements correlated well with the microscopy results. The wires with only intergranular precipitation had low ($\sim$ 200 DPN) hardness values which stayed constant or decreased slightly during the first heat treatment. Those wires which had intragranular precipitation showed jumps in hardness during the precipitation heat treatment to hardness values as high as 350 DPN. The hardness values were reduced substantially by longer and hotter heat treatments.

The isomorphology experiment was an attempt to reduce the large variation in the percentage of α -Ti precipitation observed in the standard experiment and the increased prestrain experiment. In order to achieve this, the diffusion of the alloys were held constant by varying the precipitation heat treatment temperature. Although the resulting microstructures were not perfectly identical, they were a considerable improvement over the microstructures observed in the previous experiments.

Based on the results in this study it has been possible to construct a graph showing the amount of initial cold work needed to avoid large jumps in the hardness and inhomogeneous precipitation before the first heat treatment. The avoidance of large increases in hardness during heat treatment is important with respect to the mechanical stability of a composite wire, while the avoidance of inhomogeneous precipitation should allow a higher ultimate intrinsic J_c.

Chapter 4

Critical Current Results

Some very high critical current densities were obtained in this experiment. The standard experiment had the best overall J_c results. The results for the increased prestrain experiment were probably affected by the wire breakage which was documented in section 2.2. The isomorphology experiment also achieved high critical current results, considering that the wires received only one cool heat treatment. Two different methods were used for measuring the critical current densities of the samples for this study: transport current and magnetization. Transport current measurements were made for all the experiments except the isomorphology experiment where only the finest wires were measured in this way.

4.1 Transport Current Measurements

Transport current measurements provide a direct way of obtaining the critical current density of a sample. A background field is applied transverse to the sample and then a current is ramped through the sample until a voltage appears. The measurements were made on 60 *cm* long samples which were wound into a solenoidal configuration and immersed in liquid helium. The solenoidal configuration of the samples when soldered in place on the sample holder is shown in figure 4.1. The diameter of the sample holder is 1.375". The wire is wound on the holder in a groove which has a pitch of 8 turns per inch. Each end of the sample holder is comprised of a copper ring for good current transfer from the leads of the rig to the wire being tested. The central gauge section of the sample holder is made of stainless steel tubing with 0.032" wall.

The background field during the transport measurements was supplied parallel to the axis of the sample holder by one of three magnets at the UW-Madison. The first magnet is a 10 T Nb-Ti-Nb_3Sn hybrid solenoid built at the UW. The second is an 11.3 T magnet comprised of an 8 T Cryogenics Consultants Limited Nb-Ti magnet and a 3.3 T Nb_3Sn magnet made at the UW. The third magnet is a 7 T American Magnetics Nb-Ti coil outfitted with a tub insert dewar for 1.8K transport measurements at reduced pressure. The

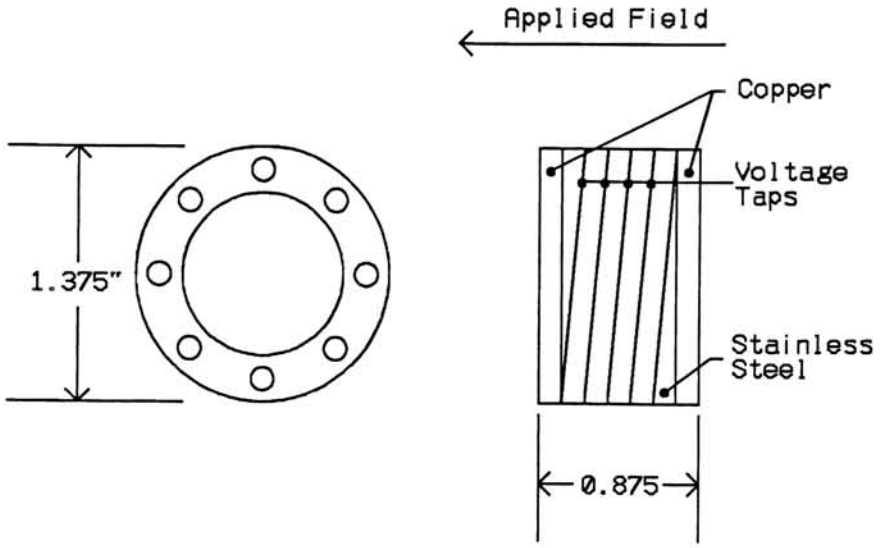

Figure 4.1: Schematic of the sample holder used for transport current measurements.

pumping system used to lower the pressure is capable of handling a 5 W heat load at 1.8K.

The sample voltage was measured by monitoring a pair of the four voltage taps soldered along the sample (see figure 4.1). The voltage taps were separated by 11 *cm* for a total of 33 *cm* between the furthest apart taps. The voltage from the taps was measured using a Keithley model 155 null detector. The output voltage from the 155 was recorded by either an X-Y chart recorder or a computer. The sample current (0-1000 A) was measured using a shunt resistor. The voltage from the shunt resistor was also fed to either an X-Y chart recorder or a computer. The critical current (I_c) for each test was determined where the V-I trace intersected a $10^{-14}\Omega m$ resistivity

line (based on the overall wire area) drawn from the origin.

The critical current density (J_c) of the Nb-Ti alloy was determined by dividing I_c by the area of the Nb-Ti in the wire. The average area of the Nb-Ti was determined from measurements of the wire diameter and copper to Nb-Ti volume ratio measurements. The wire diameter was determined using a micrometer accurate to ±0.00005". At the smallest wire size, nominally 0.003145" this micrometer would read either 0.00310" or .00315" Calculating the area from these two values gives 7.5477x10-6 in^2 and 7.79311x10-6 in^2 which is a difference of 3.3% in between the two areas. Thus for a nominal value of $3500 A/mm^2$ for the fine wire. The uncertainty is $\approx \pm 114 A/mm^2$. To reduce the uncertainty in area to 1% using this micrometer requires the wire diameter to be .010" or greater.

The Cu/Nb-Ti ratio was determined by weighing a section of wire, etching the copper off, and weighing the bare filaments. This measurement was made using a digital balance accurate to 0.1 mg on lengths of wire whose initial mass was greater than 0.5 g. The density used for copper was 8.96 g/cm^3 and the density used for each of the Nb-Ti alloys is listed in table 2.1.

4.2 Vibrating Sample Magnetometer Measurements

An alternate method of obtaining the critical current density is with mag-

netization measurements. Magnetization measurements may be used for obtaining the critical current density (J_c) by application of the critical state model [4]. This model assumes that J_c is constant across the cross-section of superconductor. Figure 4.2 shows the critical state model schematically for a superconducting slab in which the magnetic field has fully penetrated to the center. In part A of this figure, the magnetic field profile decreases linearly to the center of the slab with a slope of $dH/dx = J_c$. In part B of this figure, the critical current density J_c is shown to flow everywhere in the sample.

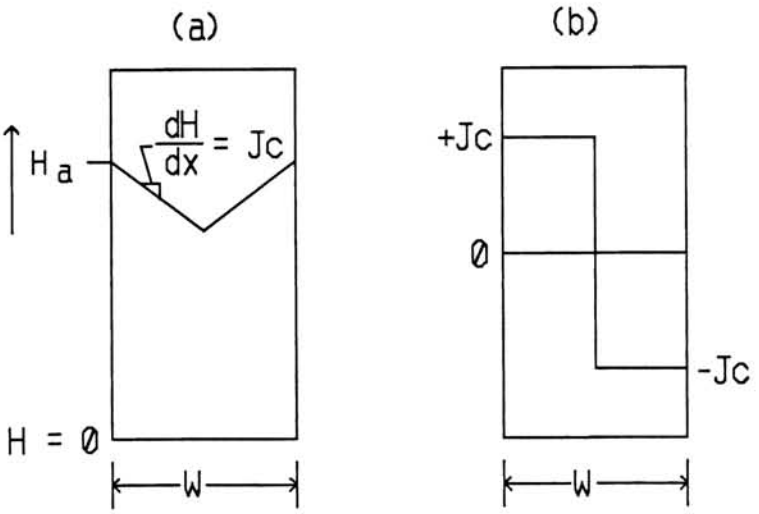

Figure 4.2: Schematic of the critical state model for a fully penetrated superconducting slab. A) Field profile, B) Current profile.

For the case of a fully penetrated superconducting filament in transverse field (figure 4.3) J_c may be obtained as follows:

proportional to the magnetic moment of the sample. The dependence of the signal on the amplitude and frequency of vibration can be removed by subtracting the signal from a vibrating reference capacitor and integrating the difference to drive the voltage across the capacitor plates. The voltage across the capacitor plates will then be proportional to the magnetic moment of the sample. Calibration of the system is accomplished by testing a sample of known moment such as a carefully prepared specimen of nickel.

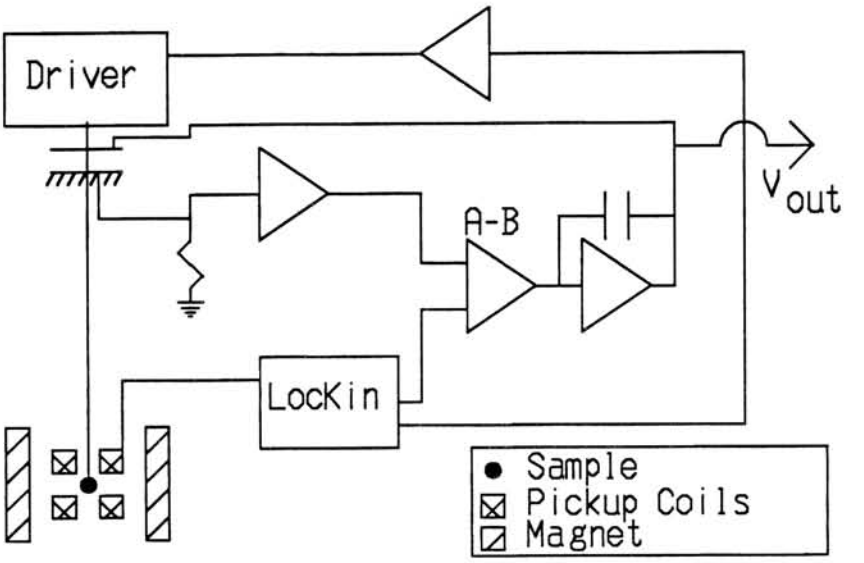

Figure 4.4: Schematic of a vibrating sample magnetometer.

The VSM used in this study consists of the vibration head and supporting electronics for a Princeton Applied Research Model 155 VSM. The magnet system used to supply the field is an Oxford 15 Tesla magnet with a variable temperature insert. The magnet current was supplied with a Cryomagnetics

IPS 100 power supply. In order to use the VSM with the Oxford magnet, the pickup coils and the sample holder had to be replaced with custom fixtures. The sample holder was replaced with a long 3 *mm* diameter Pyrex rod in order to reach the center of the magnet's field. The sample was glued directly to the bottom of the Pyrex rod with Duco cement. The pickup coil set consists of a Hemholtz coil pair [79]. Each coil has an inner diameter of 6 *mm*, an outer diameter of 12.4 *mm*, a length of 2.75 *mm*, and 3700 turns of 46 gauge wire. The center to center separation of the coils is 8.38 *mm*. A schematic cross section of the coil form is shown in figure 4.5.

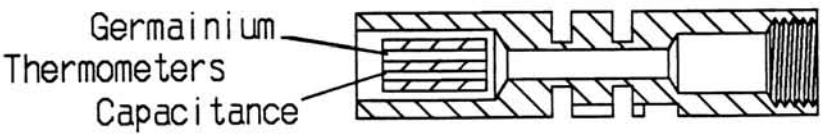

Figure 4.5: Cross section of the pickup coils used for the measurements. The location of the thermometers is also shown.

The sample temperature in the Oxford variable temperature dewar was controlled by allowing a constant flow of heated helium gas to flow along the pickup coils. The temperature was controlled using a Lakeshore DRC-91C to monitor the thermometers and to supply the current for the helium gas heater. The thermometers used for this experiment were a germanium resistor for absolute temperature measurement in zero applied field, and a capacitance thermometer for control in applied magnetic field.

Since the thermometers are coupled to the sample by gas there is some offset in the temperature. Figure 4.6 shows the T_c's measured for Nb, Pb, V, and Ta. The T_{meas} values were taken from the 50% point of the transition and the T_{act} values were taken from NBS data [77]. The line drawn through the data is the least squares fit to the data. All the temperatures for the magnetization data have been corrected using the equation:

$$T_{act} = T_{meas} * 0.981673 + 0.2124841 \tag{4.8}$$

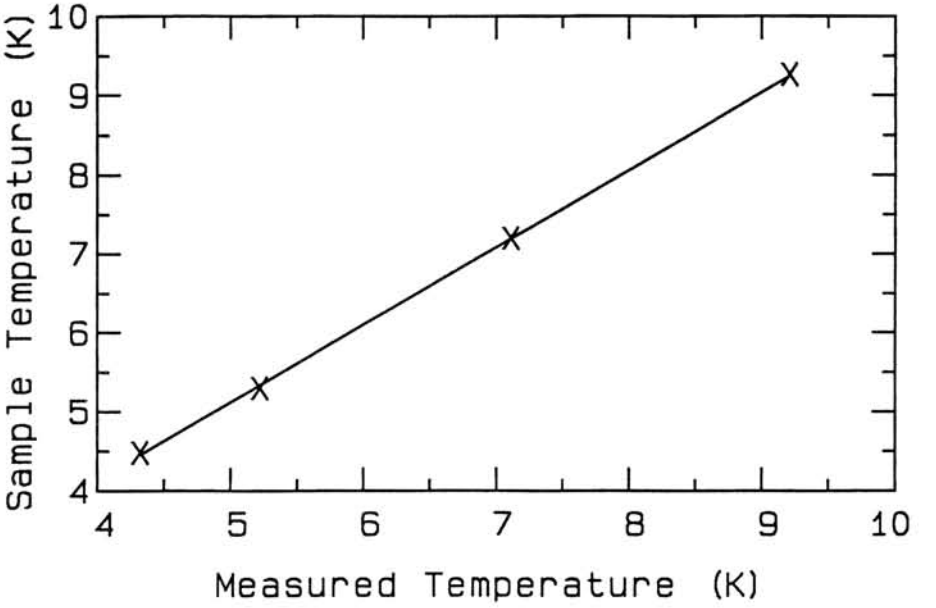

Figure 4.6: Actual sample temperature as a function of the thermometer temperature for the VSM.

Magnetization tests were done only on the wire from the isomorphology experiment. Samples were cut directly from the wire at 0.050", 0.0285", and 0.0179" diameter using a diamond saw. For the 0.0113" and 0.0063" diameter

wires, 20 to 40 pieces of wire were bundled together and glued with Duco cement prior to cutting. The sample lengths ranged from .060" to .110". Samples were measured from approximately 2K to T_c.

4.3 J_c Results of the Standard Experiment

Figures 4.7 to 4.10 show J_c versus the final drawing strain as a function of applied field for the standard experiment. As can be seen in figures 4.7 to 4.9, the best heat treatment for CB75XX to CB77XX (Nb46wt%Ti to Nb53wt%Ti) was 3X80h/420°C. In the case of the 40h heat treatments at 5T and 4.2K, 420°C did best at low strains. However, the curves for the 420°C heat treatments peaked before the curves for the 435°C heat treatment and the wires which received the 435°C heat treatment ultimately achieved the best results for the 40H heat treatments.

In the case of CB793X and CB803X the best heat treatment temperatures is clearer. As shown in figure 4.10 the curves for 3X40h/435°C lie above the other curves. The obvious choice between these two alloys is Nb58wt%Ti. Nb62wt%Ti appears to be too high in Ti content to achieve high J_c's in the range of interest. The benefit of using high Ti alloys at low fields is shown in figure 4.11. In this figure the sample with the highest 2T J_c for each composition was chosen. As can be seen, Nb58wt%Ti performed better at low field (2-3 T) than Nb46.5wt%Ti. Note that the J_c values shown in

figure 4.11 are lower than those shown in figures 4.7 and 4.10. Presumably this degradation occurred between the two measurements when the wires were desoldered from the sample holders following the original testing and soldered onto different solder holders prior to more complete J_c versus B testing.

4.4 J_c Results of the Increased Prestrain Experiment

The critical current density results of the increased prestrain experiment are shown in figures 4.12 and 4.13. As described in the section on sample fabrication, most of the wire for this experiment could not be fabricated to final size. Therefore, all the curves shown in figure 4.3 except CB10228 are for the smallest size the wire could be fabricated to rather than the design size. Even so, several of the wires had critical current densities near $3000 A/mm^2$ (5T, 4.2K). This is actually fairly remarkable since wire breakage reduces the critical current density in two ways. The first is the most obvious. Since the wire broke there must be severe mechanical damage to the superconducting filaments contained in the wire. This lowers the critical current density extrinsically. Second, since the wire broke above the design size the optimum high J_c microstructure was not obtained in the material, thus limiting the critical current density intrinsically.

Figure 4.13 shows the critical current density obtained for CB10228 versus final drawing strain. The peaks in the curves were all broad and occur at lower strain than the monofilament Nb53wt%Ti (see figure 4.9). It is unclear whether this is because this composite is suffering from mechanical problems, as did the rest of the wires in the experiment, or whether it is due to the reduced number of heat treatments the wire received.

4.5 Standard Experiments on Nb44wt%Ti and Nb52wt%Ti

The results from the standard experiments on Nb44wt%Ti are shown in figure 4.14. UW138C is the wire which received a standard processing sequence in this experiment. Thus it is surprising to see how low the J_c in UW138C is (2350 A/mm^2, 5T, 4.2K) compared to the Nb46.5wt%Ti wire from the standard experiment CB7538 (3450 A/mm^2, 5T, 4.2K).

Figure 4.15 shows the results of the standard experiment performed on the Nb52wt%Ti alloy (CB3738). The results of the standard experiment on this alloy were very good, J_c reached 3140 A/mm^2 (5T, 4.2K), but the critical current density is only a weak function of the final drawing strain. Determination of whether the weak dependence of J_c on ϵ_f was due to a large variation in the precipitate size and morphology is pending the completion of the microstructural analysis. Since the current densities values obtained in this experiment were high this alloy is a good replacement for the Nb53wt%Ti

treatments.

The Nb44wt%Ti alloy did not achieve the good results expected, and appears to be beyond the peak in a critical current versus alloy composition curve. The other extreme on the curve appears to be Nb62wt%Ti which also had poor results. Between Nb44wt%Ti and Nb62wt%Ti lies the range of Nb-Ti alloys which are suitable for high current applications. The low end of this range is best suited to high field applications (5-8T) and the high end of this range is best suited to low field applications (2-4T).

The critical current results of the increased prestrain experiment, although limited by the problems during fabrication, were still quite respectable. However, as shown in chapter 3, the main contribution of the increased prestrain experiment was toward microstructural understanding.

Finally, although the J_c values of the isomorphology experiment are quite low, they hint at what may actually be the controlling factor in Nb-Ti alloys: the percentage of α-Ti. Recently work has begun on wires which are designed to have a large amount of pinning center (precipitate) by artificial means [32, 88]. These artificial pinning center materials have the potential for improving the critical current densities in Nb-Ti by overcoming the metallurgical limitations to precipitation in Nb-Ti alloys.

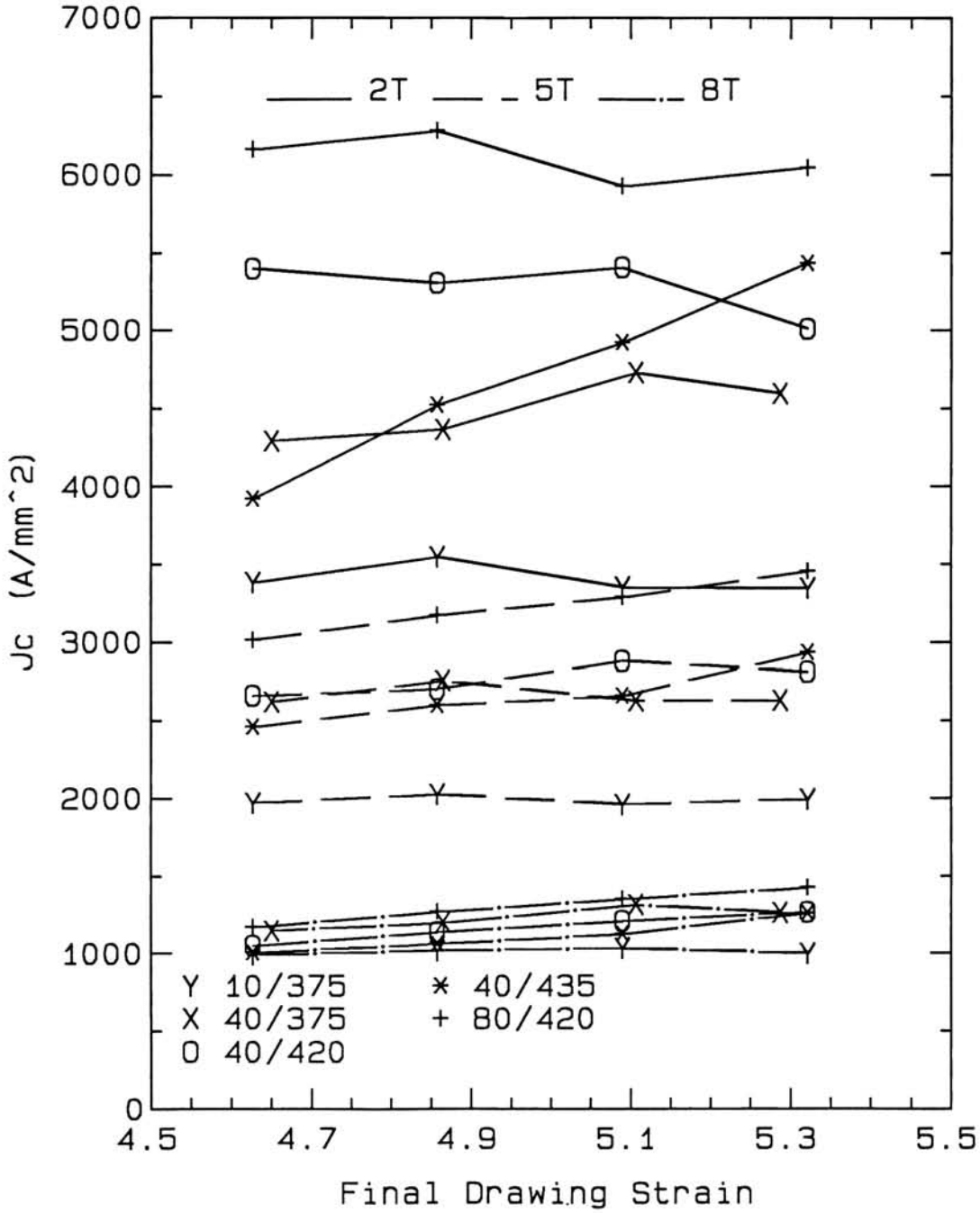

Figure 4.7: J_c as a function of the final drawing strain for the Nb46.5wt%Ti wires in the standard experiment (4.2K).

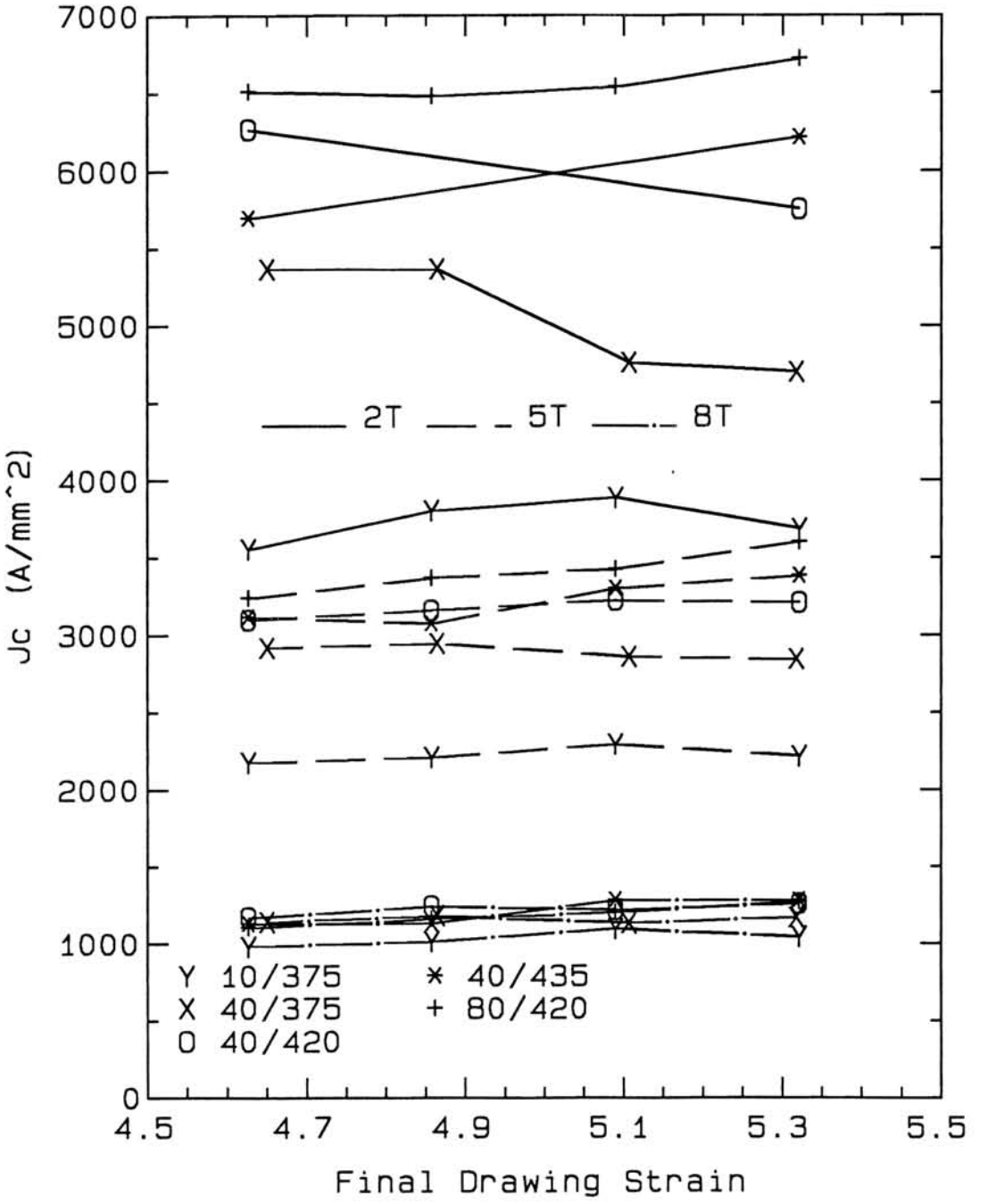

Figure 4.8: J_c as a function of the final drawing strain for the Nb49wt%Ti wires in the standard experiment (4.2K).

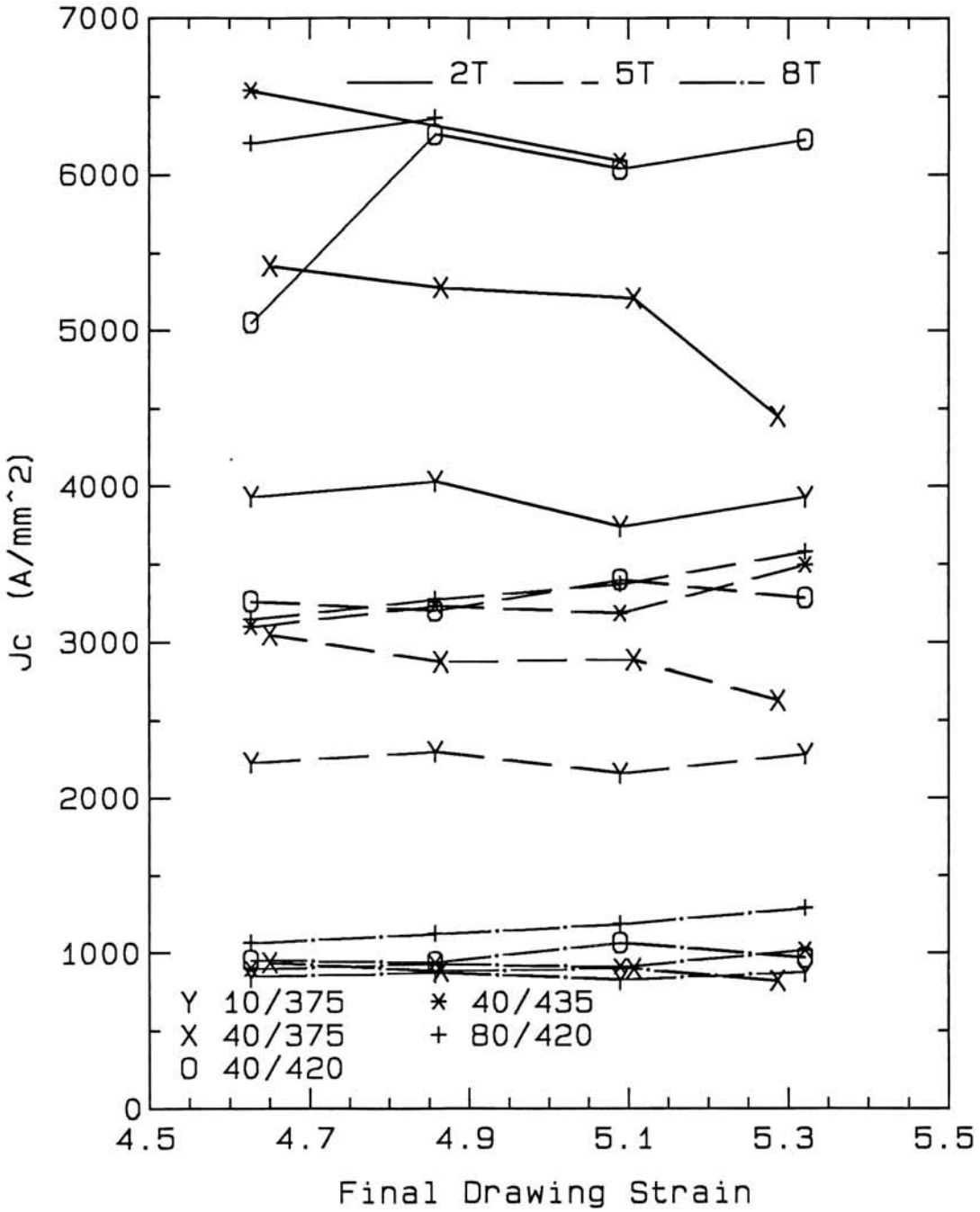

Figure 4.9: J_c as a function of the final drawing strain for the Nb53wt%Ti wires in the standard experiment (4.2K).

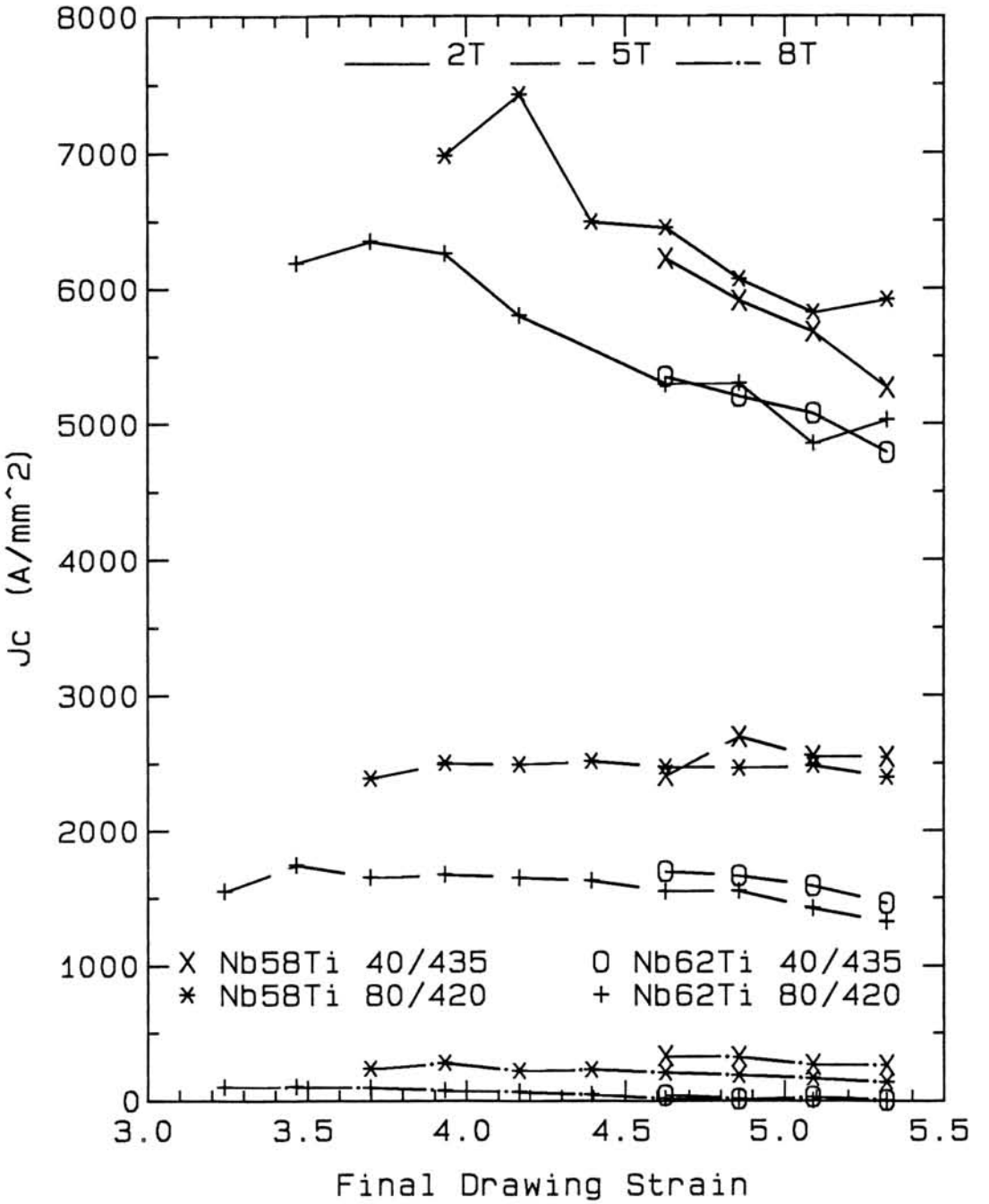

Figure 4.10: J_c as a function of the final drawing strain for the Nb58wt%Ti and Nb62wt%Ti wires in the standard experiment (4.2K).

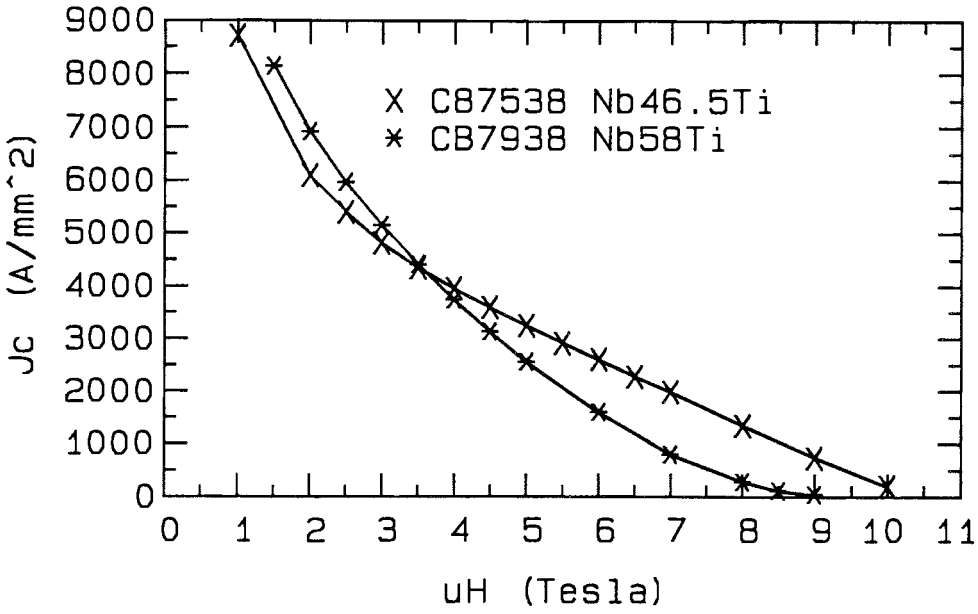

Figure 4.11: Jc versus applied field for CB7538 and CB7938. The advantage of Nb58wt%Ti at low fields can be clearly seen (4.2K).

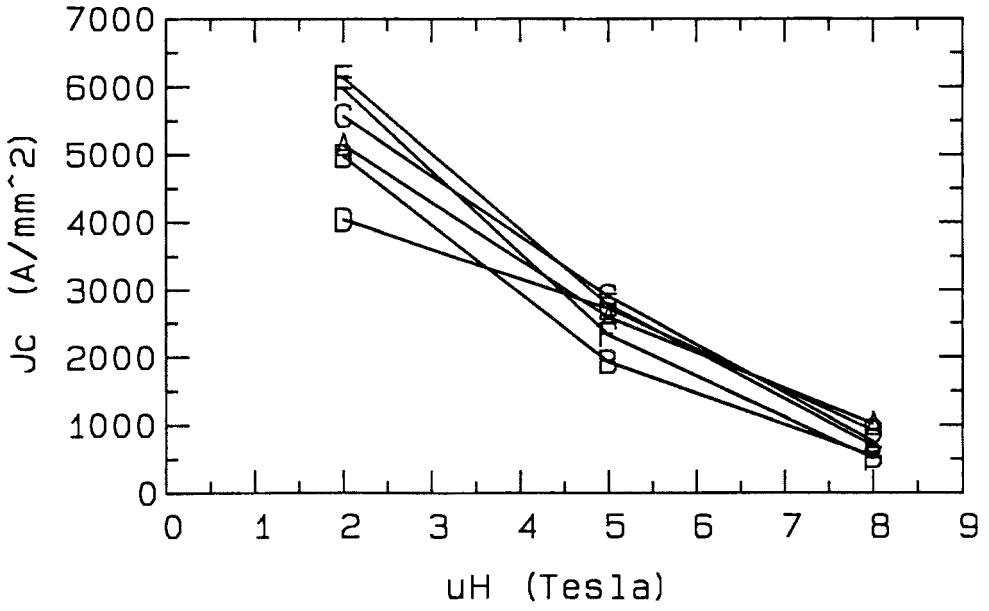

Figure 4.12: J_c versus applied field for the wires from increased prestrain experiment. A=CB10028 0.005", B=CB10128 0.010", C=CB10228 0.0035", D=CB10038 0.0063", E=CB10138 0.0063", and F=CB10238 0.0079" (4.2K).

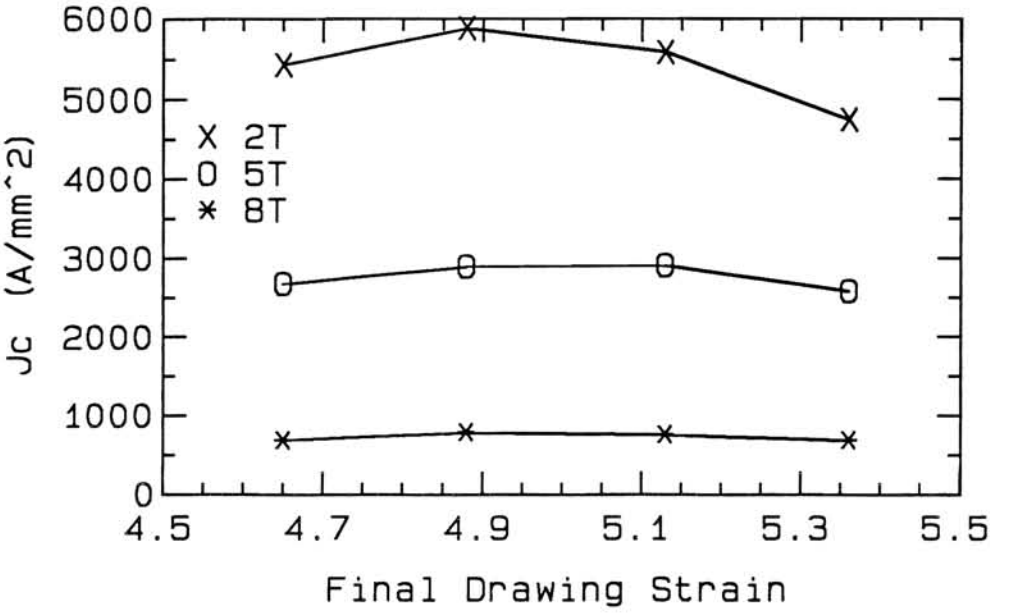

Figure 4.13: J_c as a function of the final drawing strain for CB10228 (Nb53wt% Ti) for the increased prestrain experiment (4.2K).

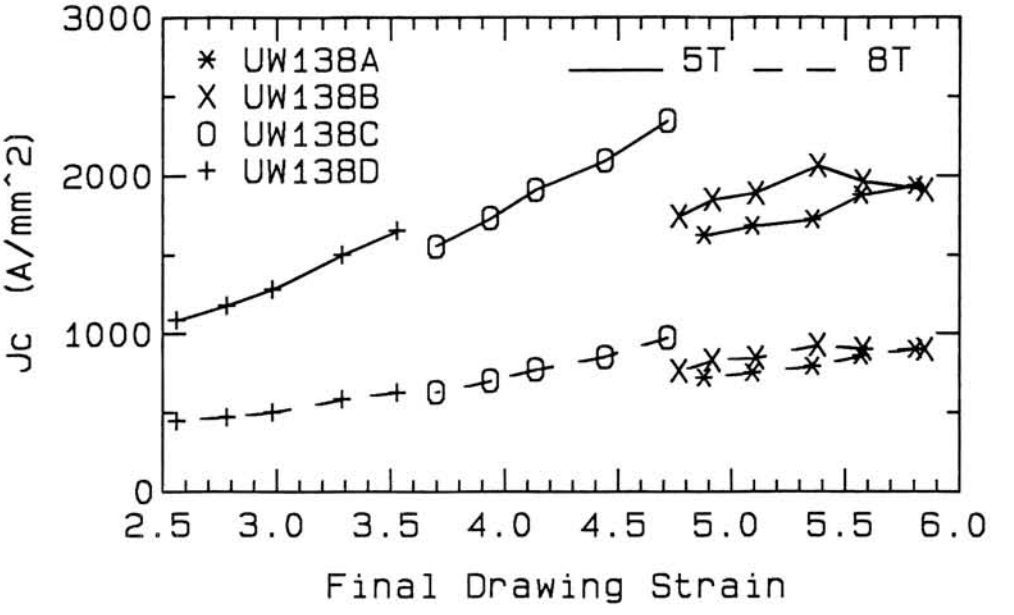

Figure 4.14: J_c as a function of the final drawing strain for the Nb44wt%Ti standard experiment. (4.2K)

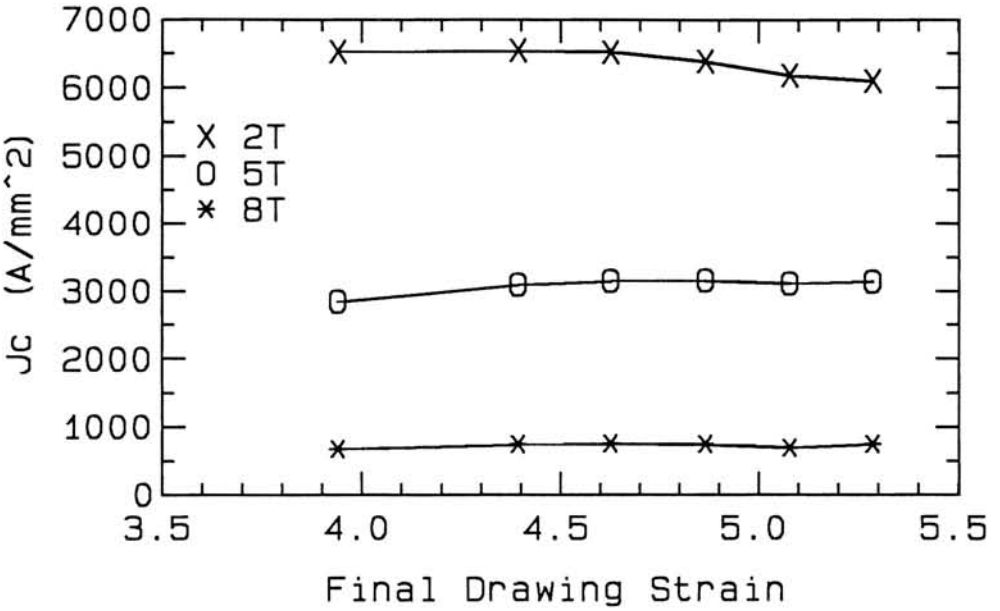

Figure 4.15: J_c as a function of the final drawing strain for the Nb52wt%Ti standard experiment. (4.2K)

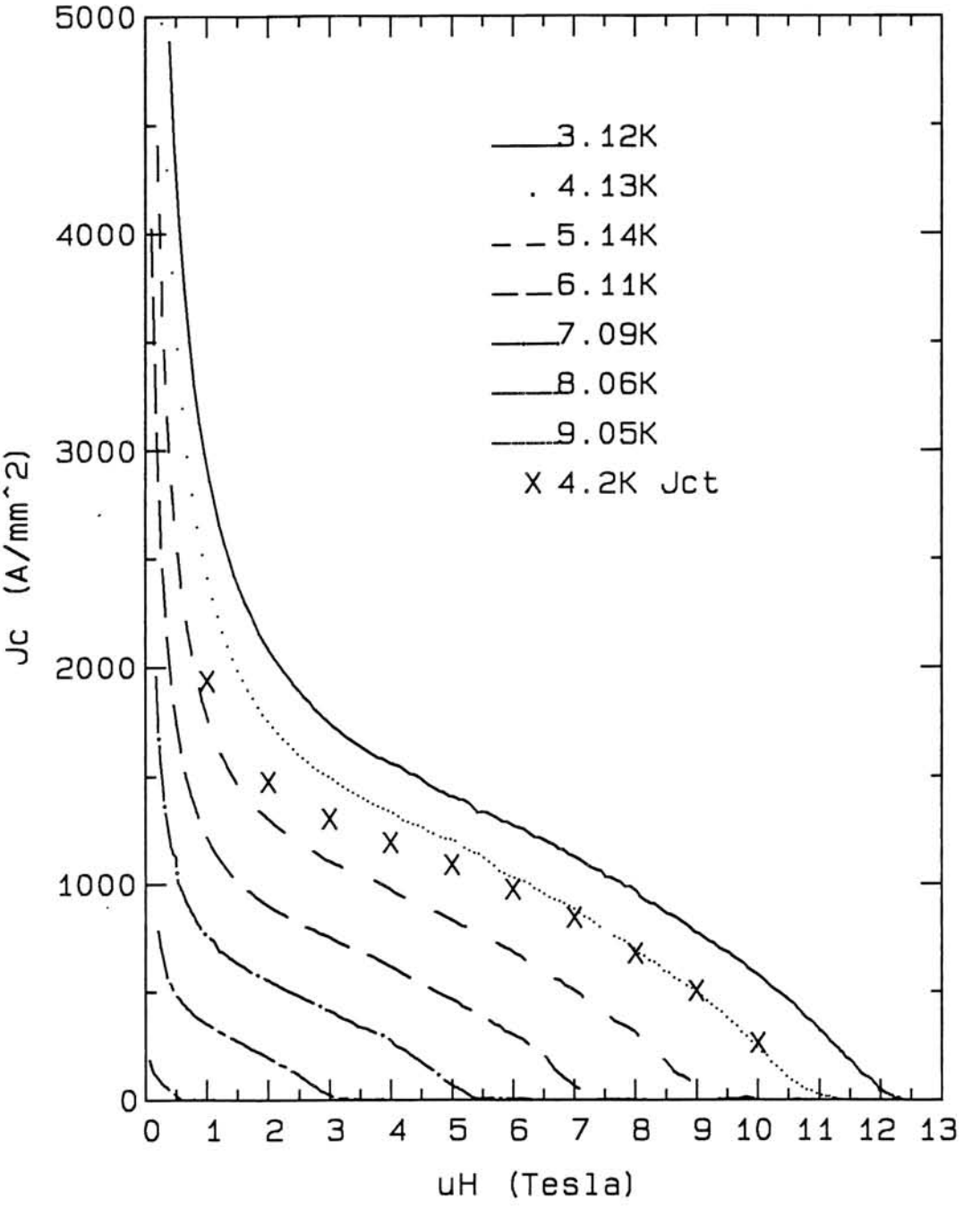

Figure 4.16: J_c versus field and temperature for the finest Nb44wt%Ti wire from the isomorphology experiment (UW1719 0.0063"). The 4.2K transport current results are shown for comparison.

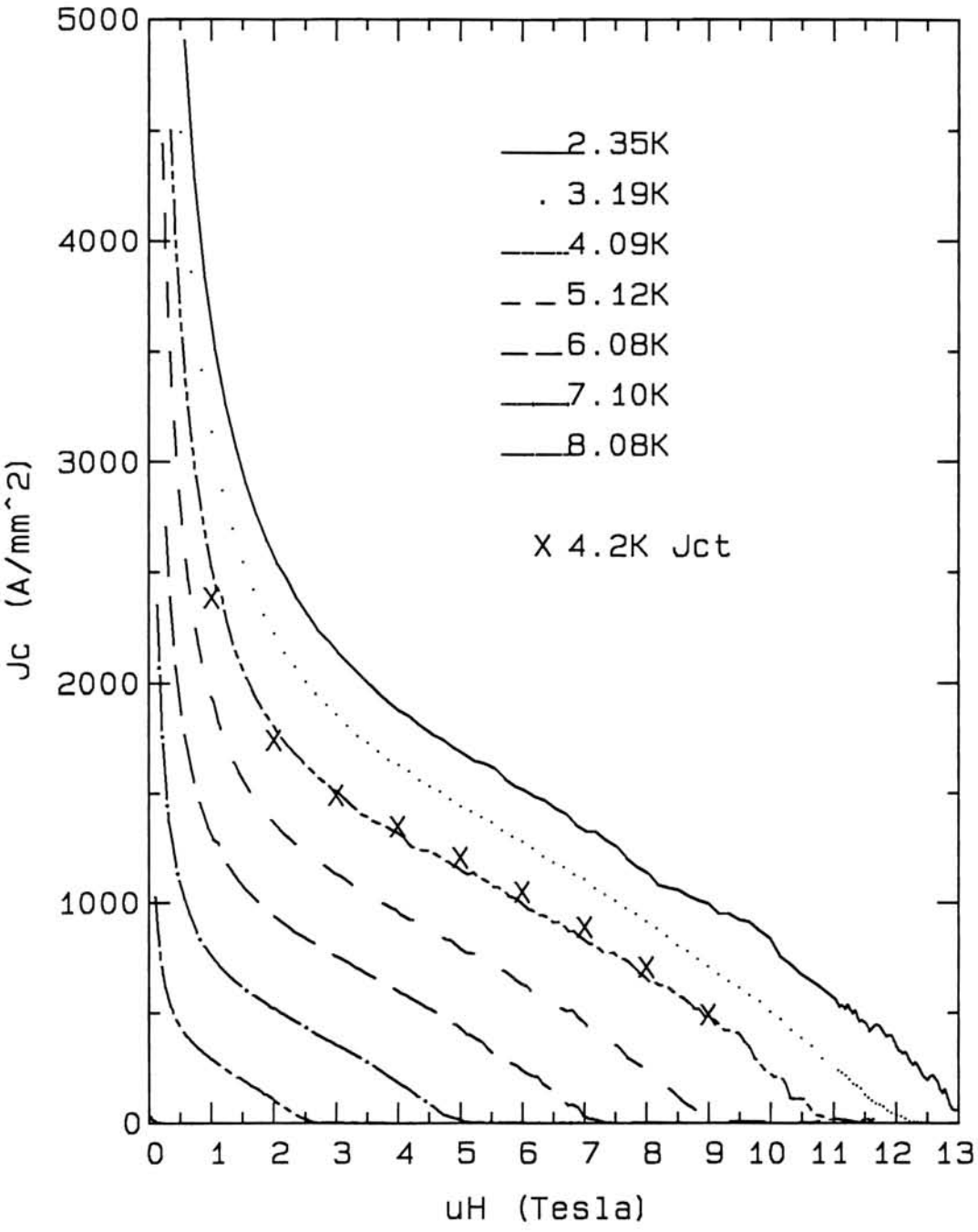

Figure 4.17: J_c versus field and temperature for the finest Nb46.5wt%Ti wire from the isomorphology experiment (UW2119 0.0063). The 4.2K transport current results are shown for comparison.

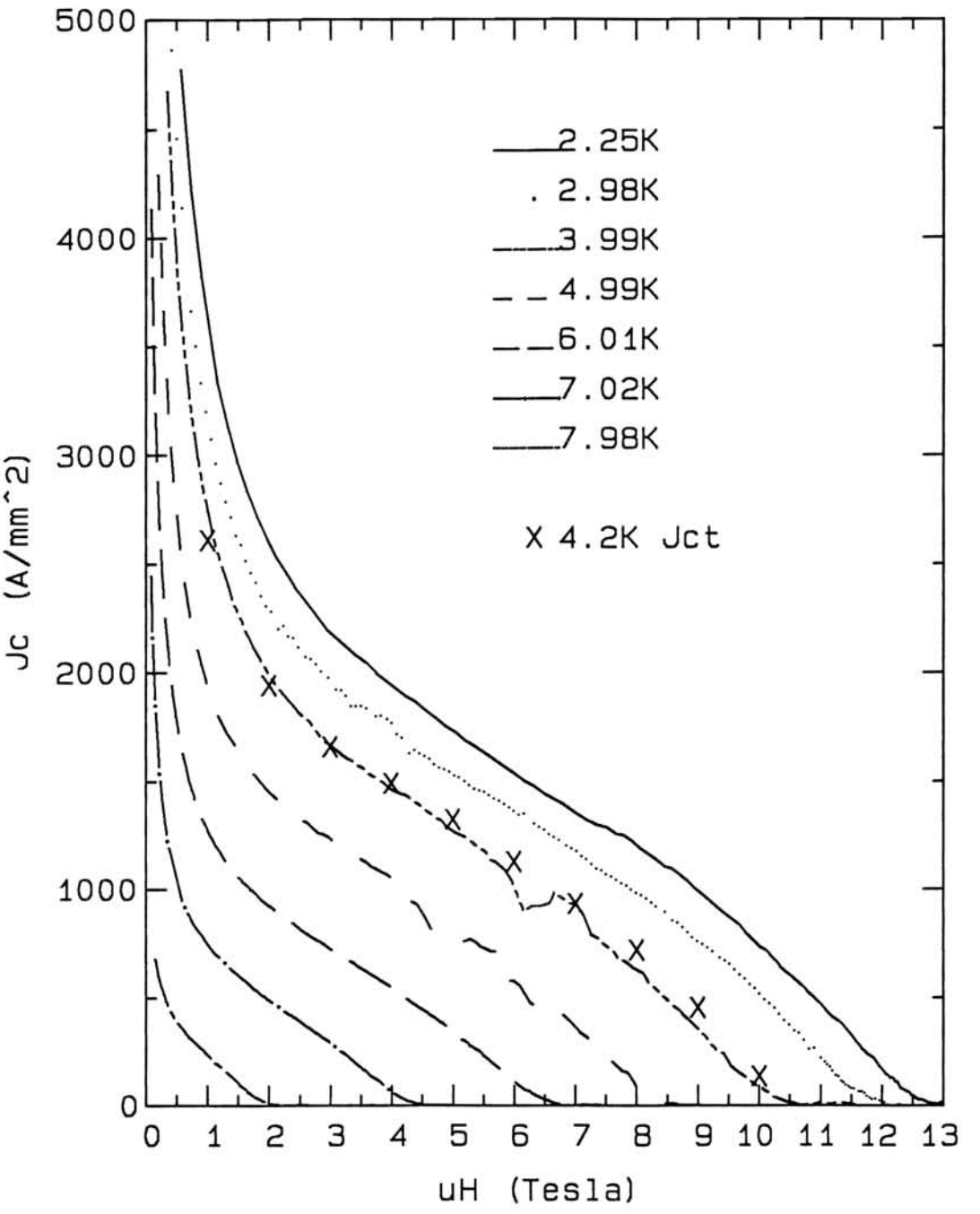

Figure 4.18: J_c versus field and temperature for the finest Nb49wt%Ti wire from the isomorphology experiment (UW2219 0.0063). The 4.2K transport current results are shown for comparison.

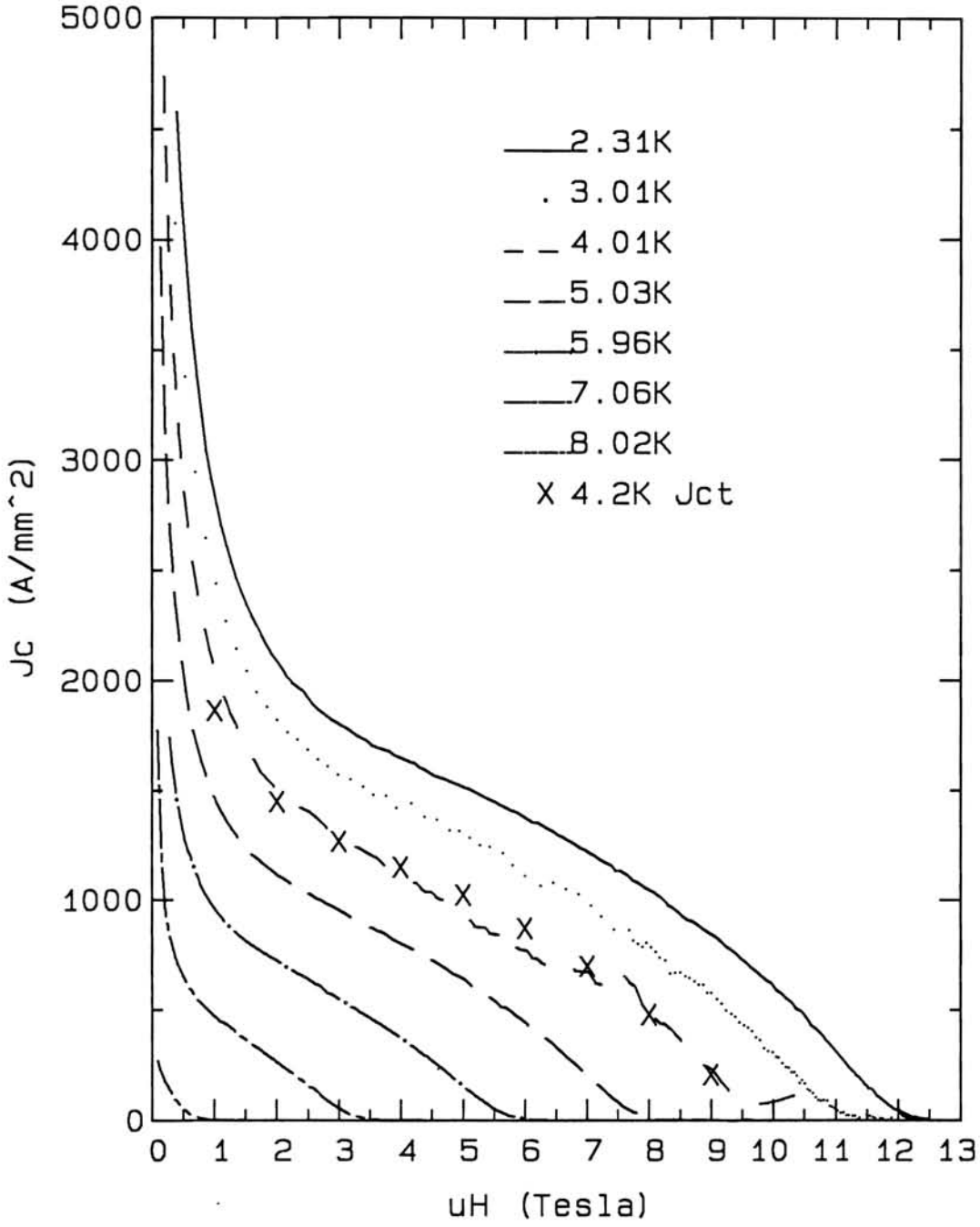

Figure 4.19: J_c versus field and temperature for the finest Nb52wt%Ti wire from the isomorphology experiment (UW3419 0.0063"). The 4.2K transport current results are shown for comparison.

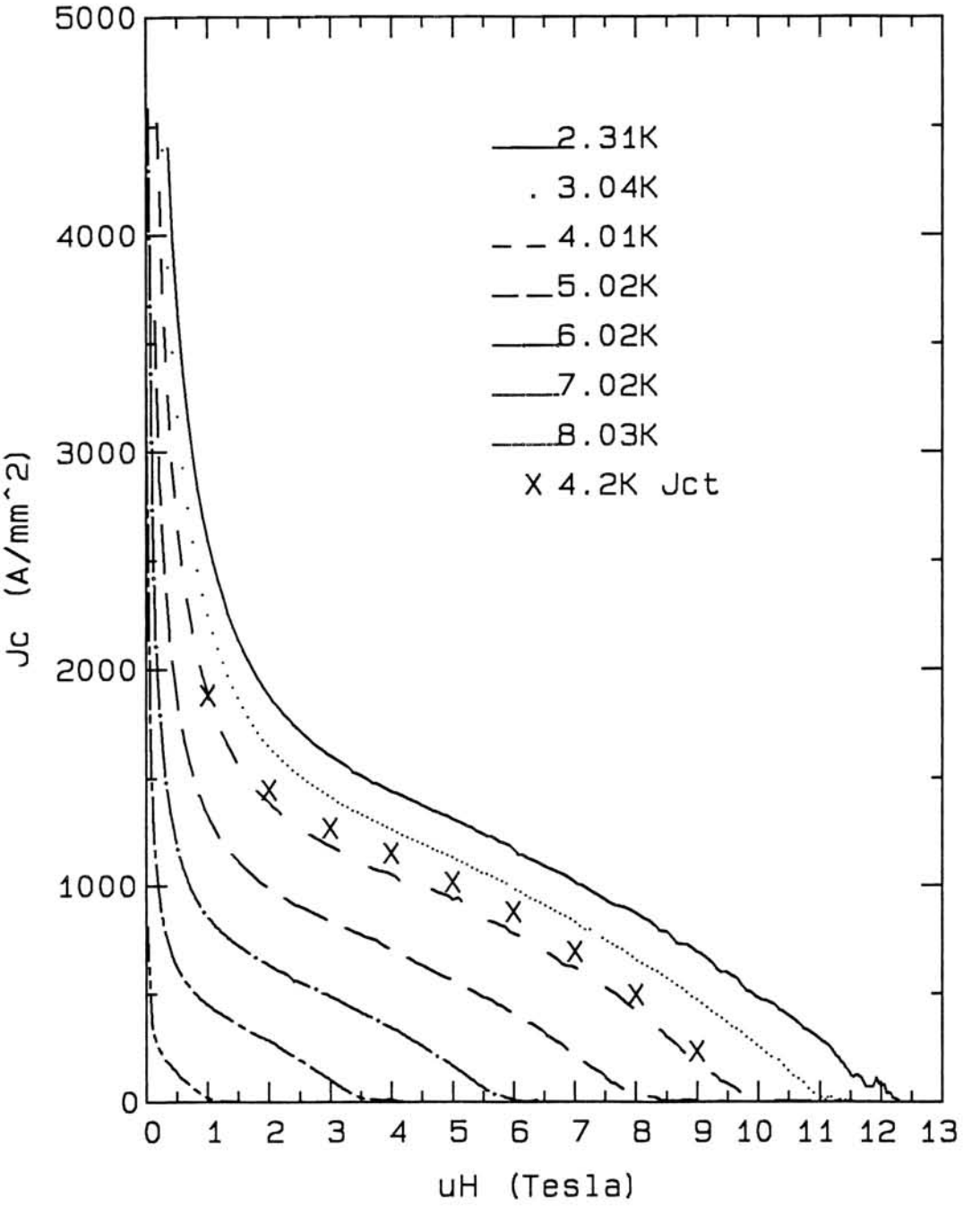

Figure 4.20: J_c versus field and temperature for the finest Nb53wt%Ti wire from the isomorphology experiment (UW2319 0.0063"). The 4.2K transport current results are shown for comparison.

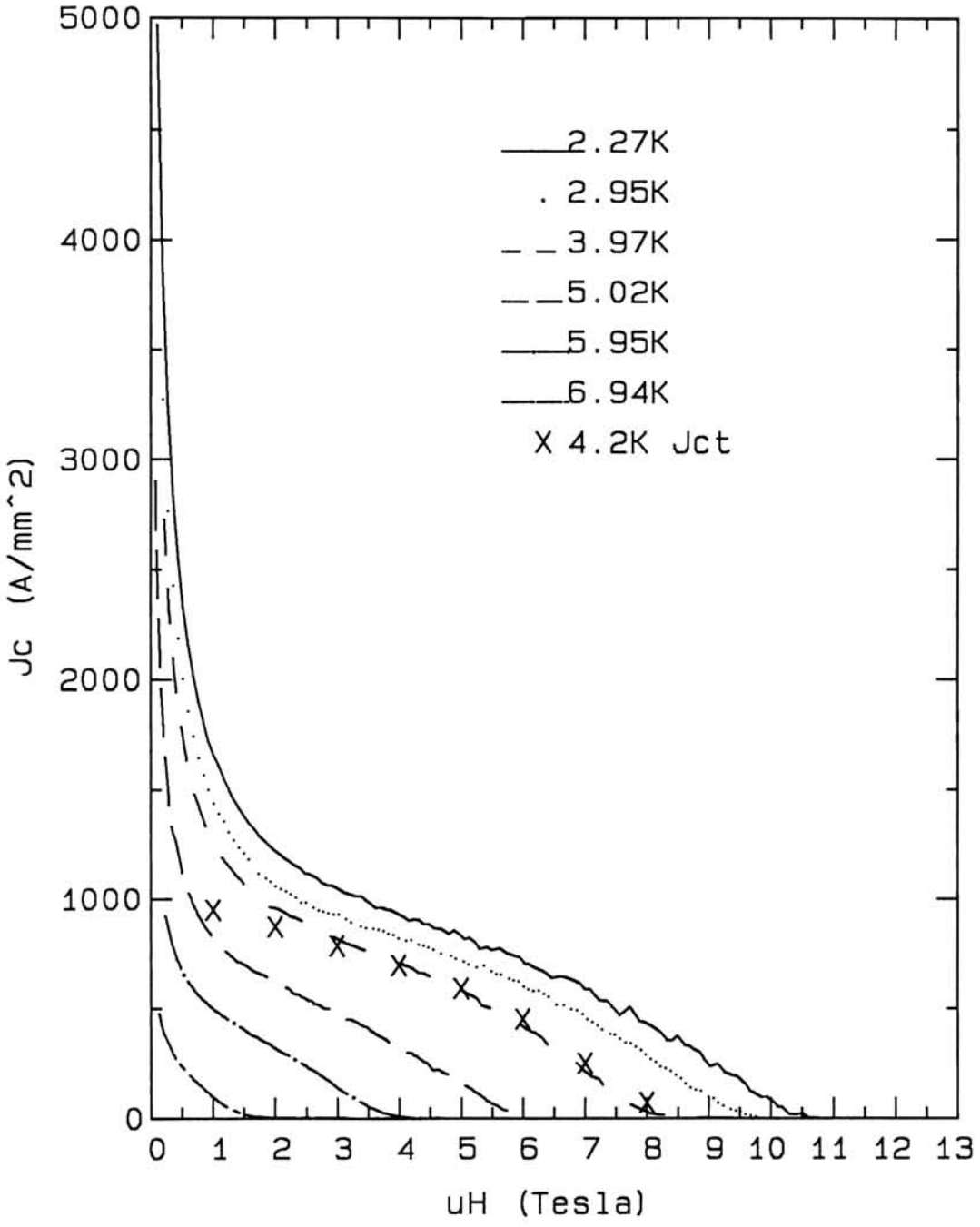

Figure 4.21: J_c versus field and temperature for the finest Nb58wt%Ti wire from the isomorphology experiment (UW2419 0.0063"). The 4.2K transport current results are shown for comparison.

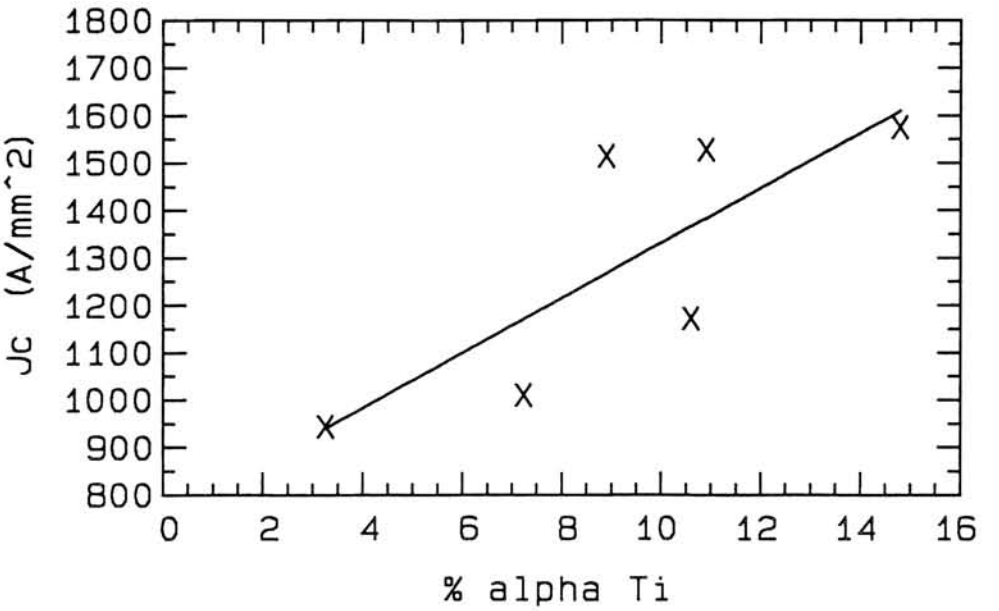

Figure 4.22: J_c versus the percentage of α-Ti at 5T. The temperature was chosen for each alloy such that $10.01 \leq H_{c_2} \leq 10.25$T.

Chapter 5

Flux Pinning Results

The flux pinning results of this study are composed of two parts. The first and smaller part contains the flux pinning results of the standard experiments. These results are similar to those earlier observed in Nb-Ti alloys. The Nb46.5wt%Ti alloy has a curve shape similar to $b(1-b)$ and as the composition is increased, the curve shifts toward $b^{1/2}(1-b)^2$. The second part of the flux pinning results, which were observed on the isomorphology experiment, show that the shift in the pinning force curve with increasing Ti content can, in part, be avoided through proper processing.

5.1 Standard Experiments

In chapter 3 on microstructure, it was shown that the percentage of α -Ti precipitate in the wires increases as the overall Ti content of the alloy increases. This increase, combined with the change in the other superconducting properties (T_c, H_{c_2}) as the Ti content was increased, caused a shift in the peak of the pinning force curve. This shift toward lower field with increasing Ti content is shown in figure 5.1. For Nb46.5wt%Ti the shape of the curve is much like those reported by Matsushita and Küpfer in the non-saturated case [58][1]. In contrast the curve for the Nb62wt%Ti wire looked much like Matsushita and Küpfer's saturated curves and the curves observed by Panek et al. for Nb65wt%Ti [70]. As shown below, this behavior changed considerably when the microstructure was controlled.

5.2 Isomorphology Experiment

The measurements for this experiment were done using the vibrating sample magnetometer. This allowed the temperature of the sample to be varied readily and the close spacing of the data points allows a detailed description of the pinning force curve. The flux pinning curves, shown below, each

[1] A pinning force curve which behaves as $(1-b)^2$ at high reduced fields Matsushita and Küpfer classify as saturated while one which has a linear dependance at high reduced fields $(1-b)$ is classified as non-saturated [58].

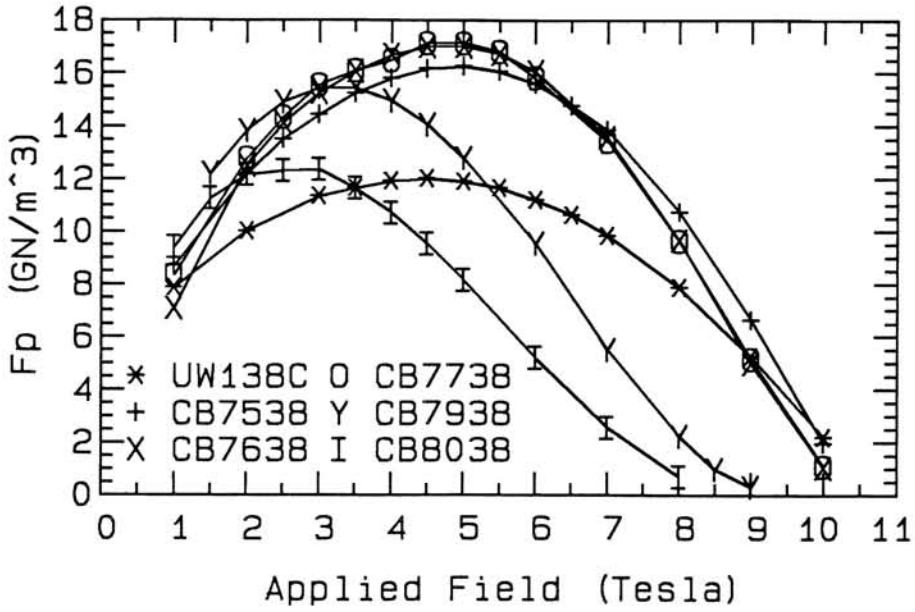

Figure 5.1: Pinning force as a function of applied field for wires from the standard experiment. UW138C = Nb44wt%Ti, CB7538 = Nb46.5wt%Ti, CB7638 = Nb49wt%Ti, CB7738 = Nb53wt%Ti, CB7938 = Nb58wt%Ti, CB8038 = Nb62wt%Ti.

contain a minimum of 50 data points and more typically several hundred data points. For this study magnetization loops were run for each sample at H_{c_2}= 1T, 2.5T, 5T, 7.5T, and 10T. This was accomplished by first testing each sample from 2K to T_c in 1K intervals to obtain the H_{c_2} versus T curve, and then interpolating the values on the curve to obtain the temperature for H_{c_2}= 1T, 2.5T, 5T, 7.5T, and 10T.

5.2.1 T_c Measurements

The T_c measurements of the wires were made by trapping flux in the sample, returning the current through the magnet to zero, and then slowly raising the

temperature until the signal from the trapped flux disappeared. A typical trace obtained by this method is shown in figure 5.2. The T_c results for the wires of this experiment are shown in figure 5.3. The T_c of the wires was usually highest after heat treatment, becoming constant with increasing cold work. Following the heat treatment, where the precipitate size and spacing are much larger than ξ, the T_c of the wires should be dominated by the composition of the β grains. This was the case for the these alloys as is shown in figure 5.4. The composition of the β grains was determined using the wet chemistry of the alloys and the measured percentage of precipitate listed in table 3.1. With the exception of the results on UW2319 (Nb53wt%-Ti, standard grade) the correlation is good.

5.2.2 H_{c_2} Results

The results of the H_{c_2} measurements on the wires in the isomorphology experiment are shown in figures 5.5 to 5.11. The H_{c_2} values were determined from where the hysteresis loops closed or the width of the loop became smaller than the background noise. In a few isolated cases, following heat treatment so the resistivity of the copper was low and near T_c where the signal from the superconductor was small, the eddy currents flowing in the copper formed a loop of constant width beyond H_{c_2}. In these cases H_{c_2} was determined by drawing a line through the linear eddy current contribution.

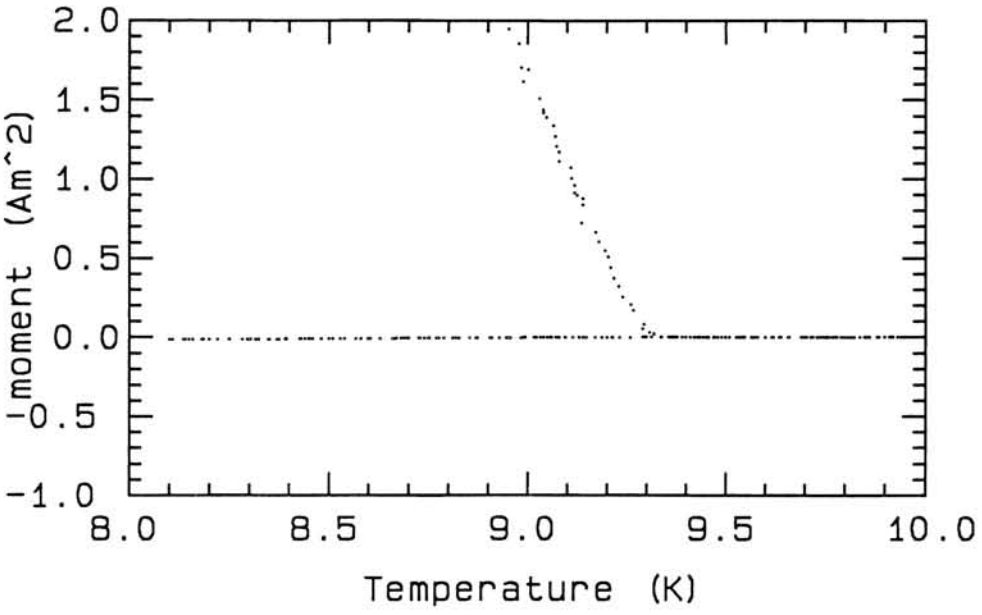

Figure 5.2: A typical trace from the T_c measurement (moment versus temperature) for UW1719 (Nb44wt%Ti) following the precipitation heat treatment.

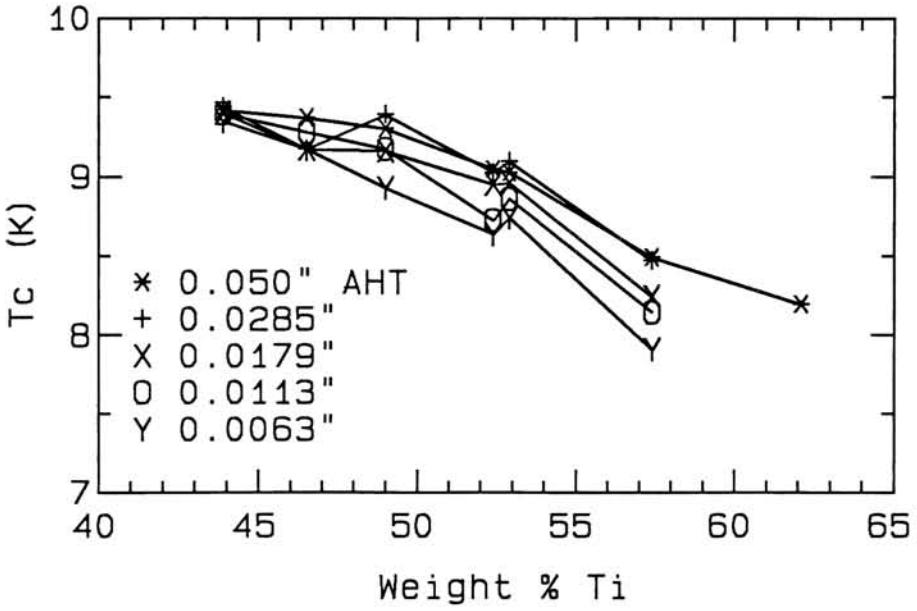

Figure 5.3: Critical temperature as a function of overall alloy composition.

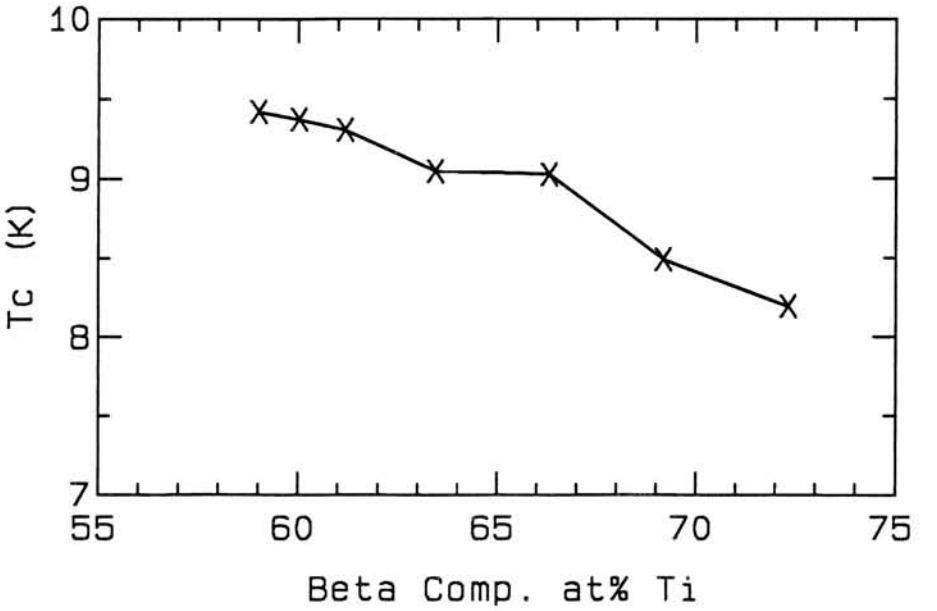

Figure 5.4: Critical temperature following precipitation as a function of the β Nb-Ti composition.

The place where the hysteresis loop deviated from this line was called H_{c_2}. The agreement between the up and down ramp for this method was quite good ($\pm$ 0.05 T). Most of the H_{c_2} versus T results are grouped quite tightly. The largest amount of scatter is for UW2419 (Nb58wt%Ti, figure 5.10). It is difficult to understand why the scatter for this wire is so large since the measurements were done identically in all cases. Two other anomalies in the data are worth mentioning. Several of the plots show curves with a 2K point which seems low. These points occurred early in the testing. As the testing progressed, it became obvious that controlling the temperature at 2K was difficult. Thus subsequent low temperature tests were done at 2.3K. The other anomaly occurred for UW2319 (Nb53wt%Ti) where near T_c the curves

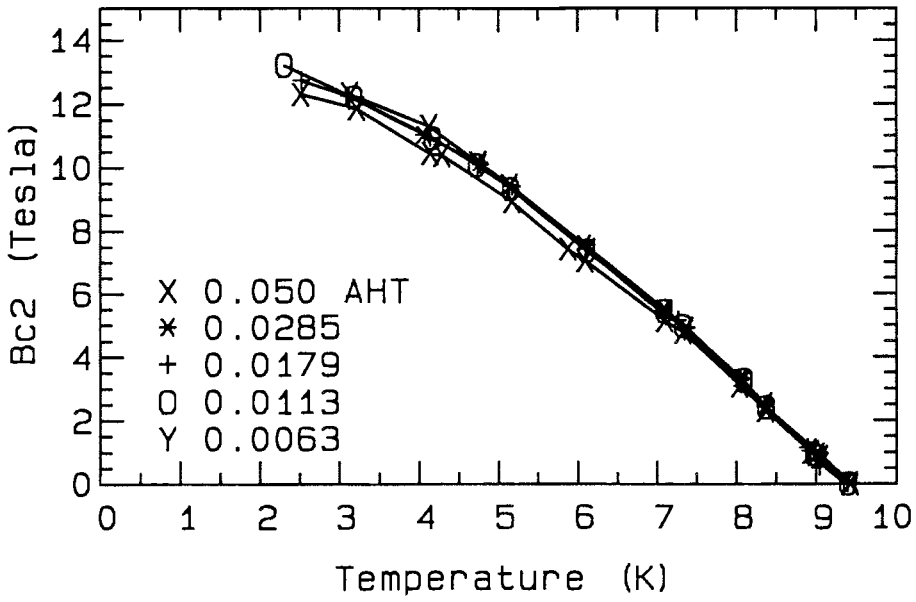

Figure 5.5: Upper critical field as a function of temperature for Nb44wt%Ti (UW1719) wires.

of the two smallest wires take a peculiar dip. The determination of H_{c_2} with this method is not as well defined as taking the 50% value of a resistivity trace. Rather, some amount of judgement is required to determine where the loop closure occurred. For temperatures where $H_{c_2} > 1$ T an upper limit on the error in determining the value of H where the loop closed is ± 0.06T. For higher temperatures the ramp rate was slowed and the error in determining the loop closure is ± 0.03T.

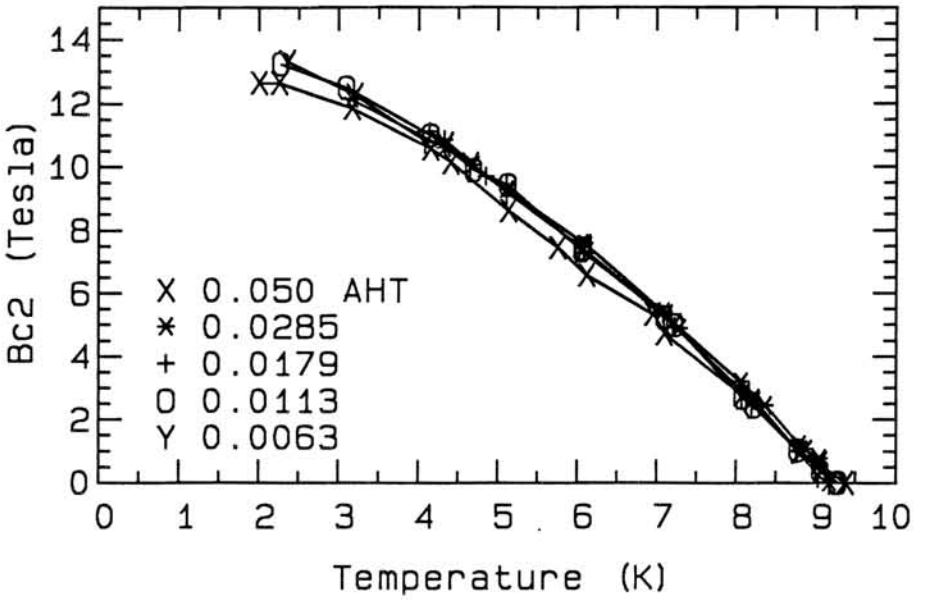

Figure 5.6: Upper critical field as a function of temperature for Nb46.5wt%Ti (UW2119) wires.

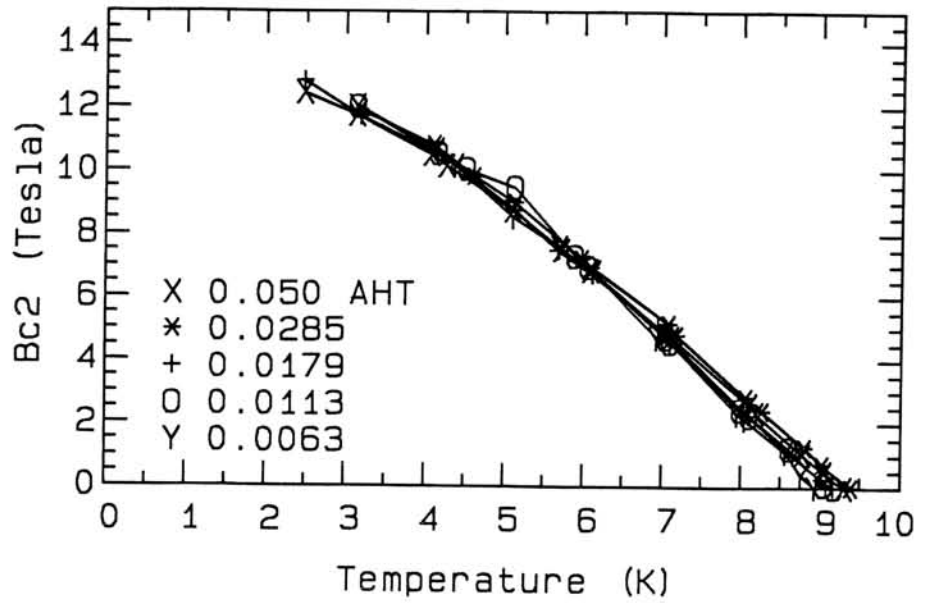

Figure 5.7: Upper critical field as a function of temperature for Nb49wt%Ti (UW2219) wires.

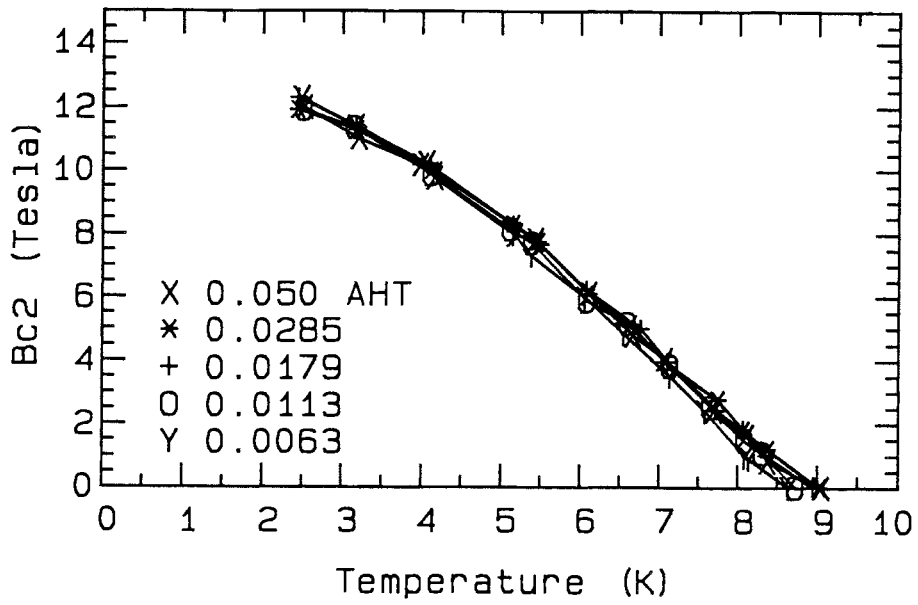

Figure 5.8: Upper critical field as a function of temperature for Nb52wt%Ti (UW3419) wires.

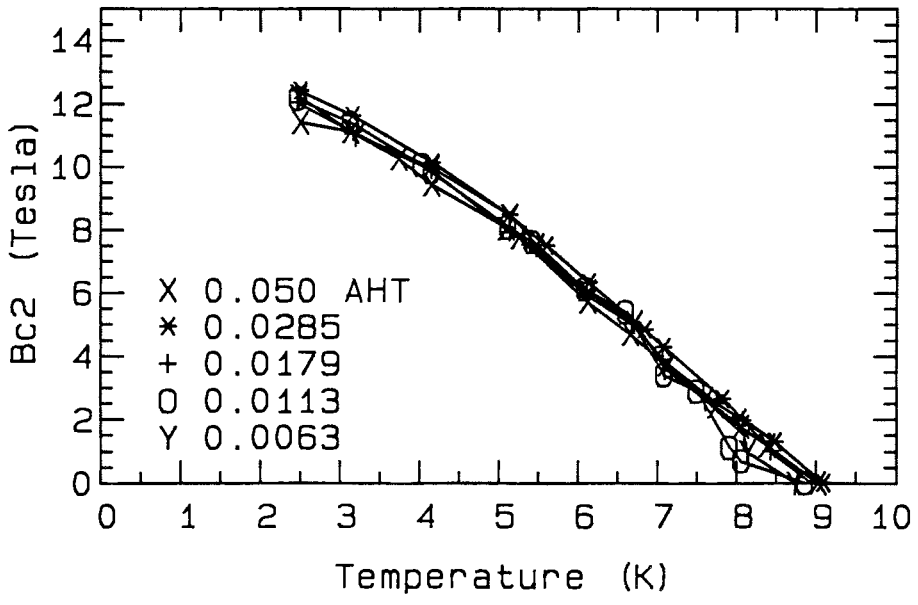

Figure 5.9: Upper critical field as a function of temperature for Nb53wt%Ti (UW2319) wires.

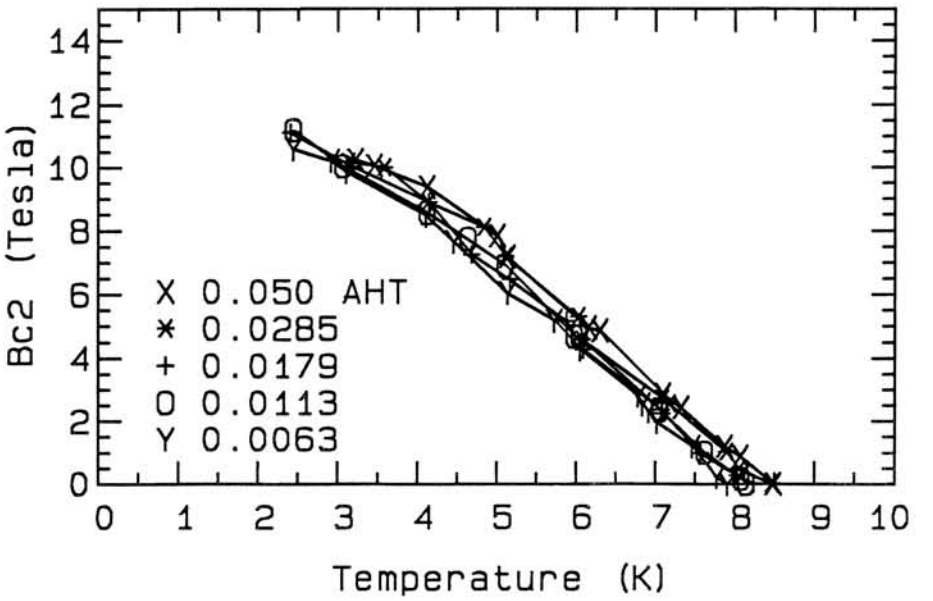

Figure 5.10: Upper critical field as a function of temperature for Nb58wt%Ti (UW2419) wires.

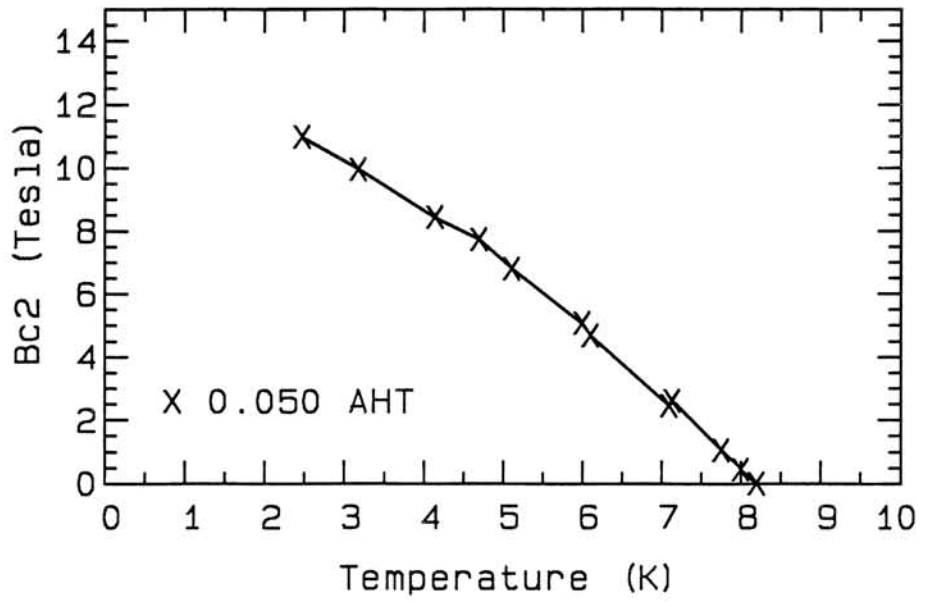

Figure 5.11: Upper critical field as a function of temperature for the Nb62wt%Ti (UW1819) wire.

5.2.3 Temperature Dependence of the Pinning Force

The temperature dependence of the global pinning force (F_p) is absorbed in the ${B_{c_2}}^q$ term of equation 1.10. If scaling occurs, the exponent q can be determined by plotting $\log(F_{p_{max}})$ versus $\log(B_{c_2})$ and fitting a straight line to the data [13]. Figures 5.12 to 5.18 show $\log(F_{p_{max}})$ versus $\log(B_{c_2})$ for the wire samples in the isomorphology experiment. At low Ti compositions, the curves were linear indicating that scaling may be occurring at the low end of the alloy range (Nb44wt%Ti, Nb46.5wt%Ti). As the alloy content changes from Nb46.5wt%Ti to Nb62wt%Ti the linearity of the curves disappeared. At high Ti contents (Nb58wt%Ti to Nb62wt%Ti) the exponent q was a function of temperature. Thus scaling did not occur for the high Ti alloys.

A closer examination of $\log(F_p)$ versus $\log(B_{c_2})$ reveals that scaling did not really occur in Nb44wt%Ti either. Figure 5.19 shows F_p versus B_{c_2} for three different reduced fields. It can be seen in this graph that the pinning force at the different reduced fields have different temperature dependencies and so scaling did not really occur for low Ti concentrations. At the high Ti end of the alloy range, the different temperature dependencies at the three different reduced fields was even more pronounced. This is shown in figure 5.20 where the difference in slope for the different reduced fields is obvious.

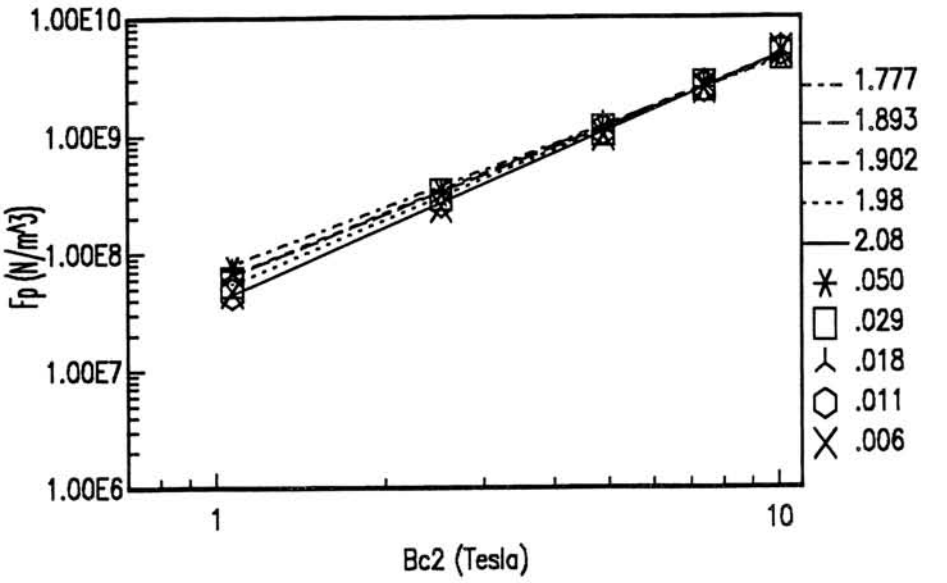

Figure 5.12: Maximum pinning force (F_p) as a function of the upper critical field (B_{c_2}) for Nb44wt%Ti (UW1719). The numbers listed by the lines are the slopes of the least squares fit to the data and the numbers listed by the symbols are the wire diameters in inches.

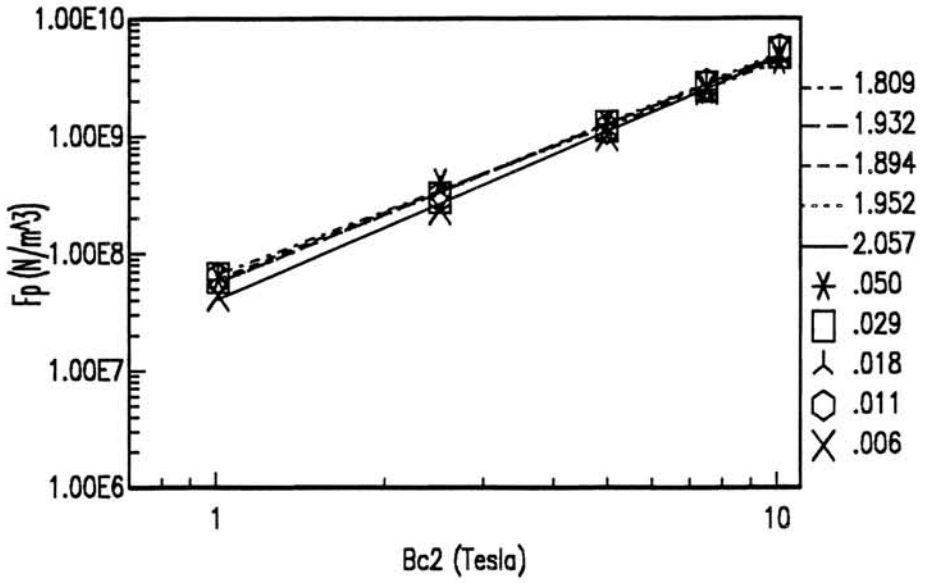

Figure 5.13: Maximum pinning force (F_p) as a function of the upper critical field (B_{c_2}) for Nb46.5wt%Ti (UW2119). The numbers listed by the lines are the slopes of the least squares fit to the data and the numbers listed by the symbols are the wire diameters in inches.

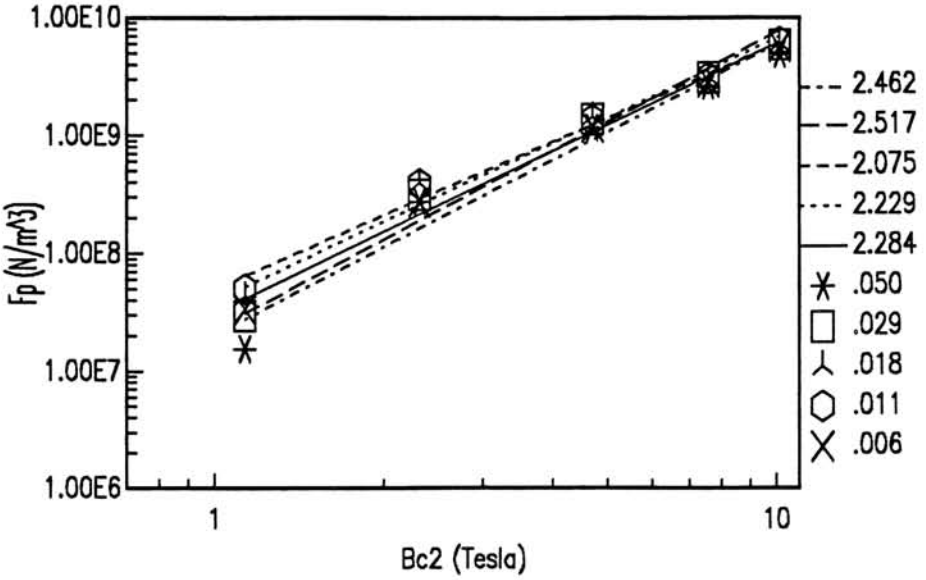

Figure 5.14: Maximum pinning force (F_p) as a function of the upper critical field (B_{c_2}) for Nb49wt%Ti (UW2219). The numbers listed by the lines are the slopes of the least squares fit to the data and the numbers listed by the symbols are the wire diameters in inches.

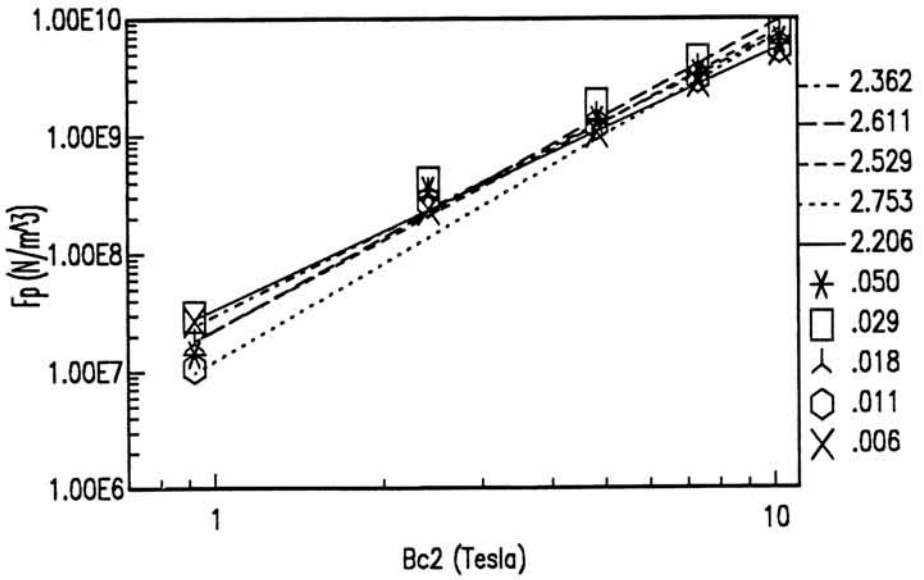

Figure 5.15: Maximum pinning force (F_p) as a function of the upper critical field (B_{c_2}) for Nb52wt%Ti (UW3419). The numbers listed by the lines are the slopes of the least squares fit to the data and the numbers listed by the symbols are the wire diameters in inches.

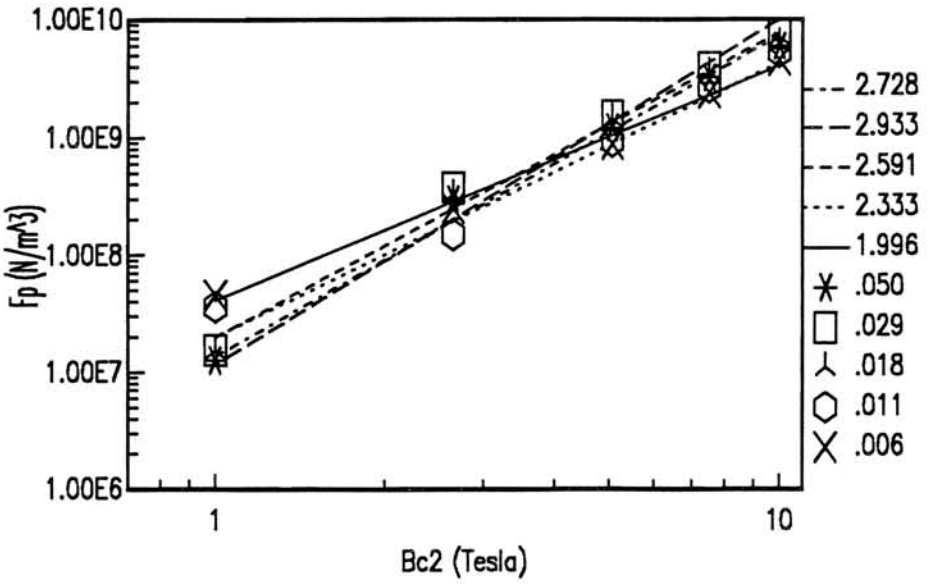

Figure 5.16: Maximum pinning force (F_p) as a function of the upper critical field (B_{c_2}) for Nb53wt%Ti (UW2319). The numbers listed by the lines are the slopes of the least squares fit to the data and the numbers listed by the symbols are the wire diameters in inches.

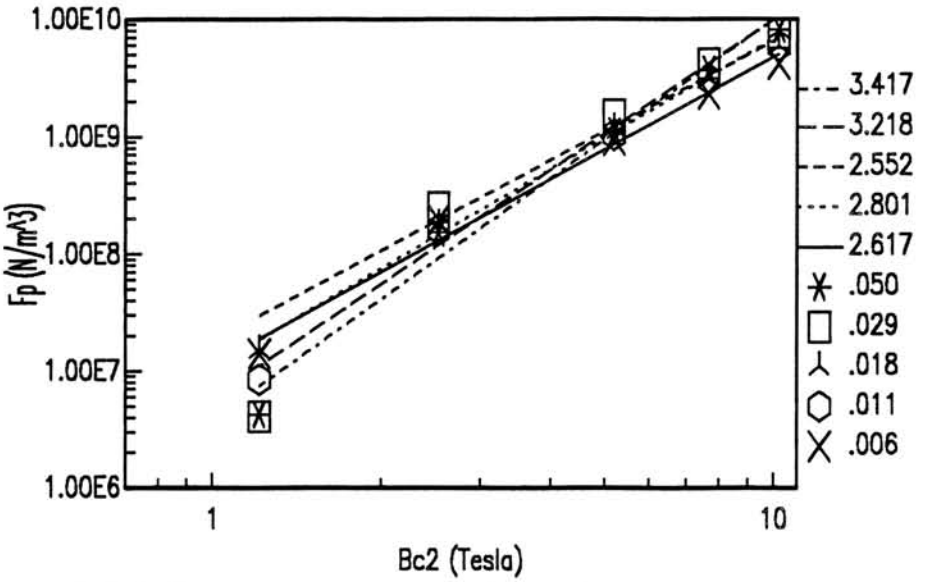

Figure 5.17: Maximum pinning force (F_p) as a function of the upper critical field (B_{c_2}) for Nb58wt%Ti (UW2419). The numbers listed by the lines are the slopes of the least squares fit to the data and the numbers listed by the symbols are the wire diameters in inches.

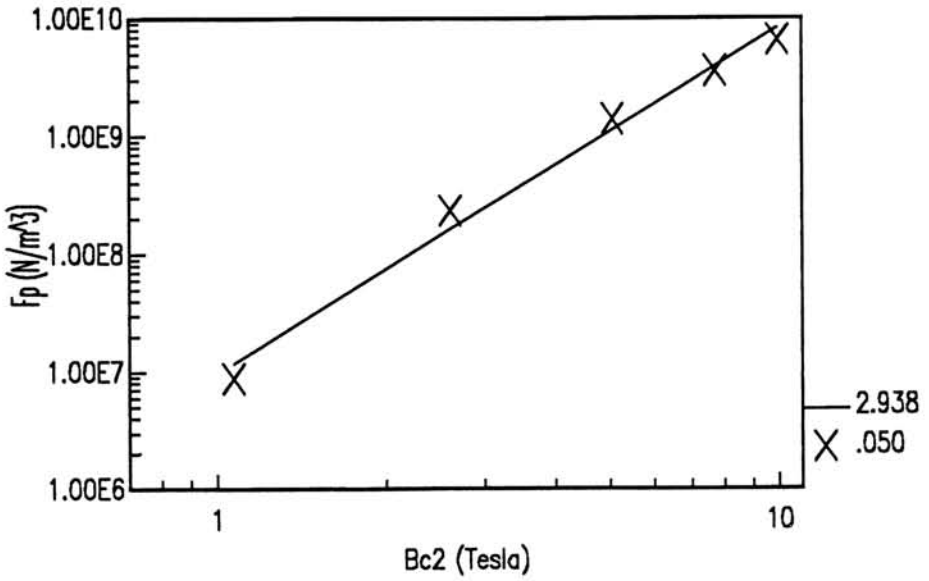

Figure 5.18: Maximum pinning force (F_p) as a function of the upper critical field (B_{c_2}) for Nb62wt%Ti (UW1819). The number listed by the line is the slope of the least squares fit to the data and the number listed by the symbol is the wire diameter in inches.

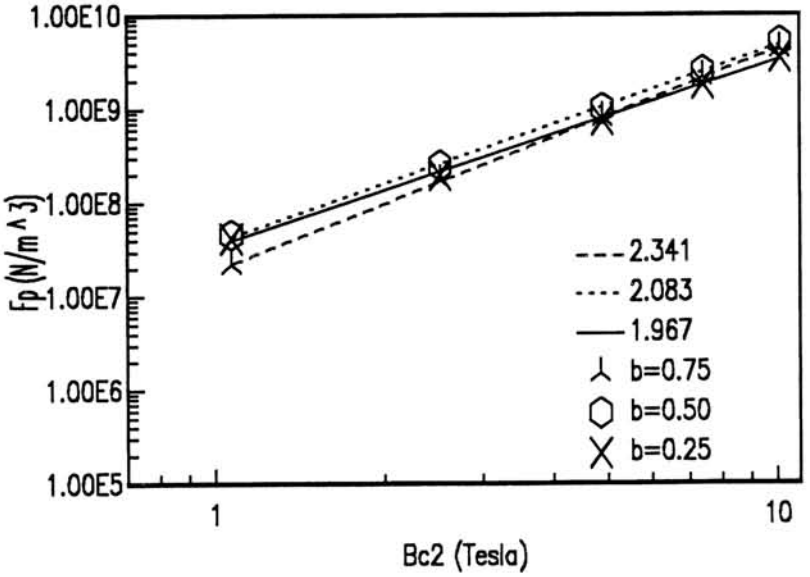

Figure 5.19: The Pinning force (F_p) as a function of the upper critical field (B_{c_2}) and reduced field b for Nb44wt%Ti (UW1719, 0.0063"). The numbers listed by the lines are the slopes of the least squares fit to the data.

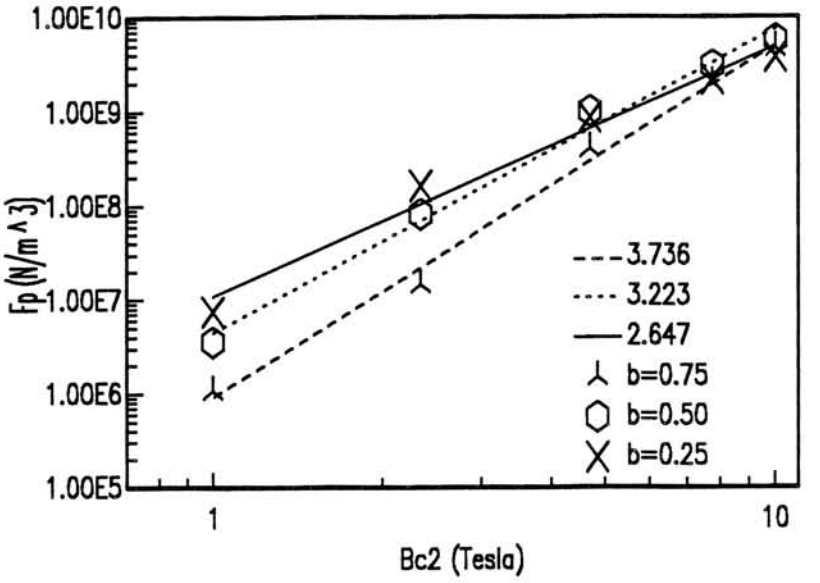

Figure 5.20: The Pinning force (F_p) as a function of the upper critical field (B_{c_2}) and reduced field b for Nb58wt%Ti (UW2419, 0.0113"). The numbers listed by the lines are the slopes of the least squares fit to the data.

5.2.4 Optimum Pinning Force

Figures 5.21 to 5.26 show the effect of the final drawing strain on the critical current density for the wires of the isomorphology experiment at $\sim$ 4K. Following the heat treatment, most of the wires showed a weak maximum in the pinning force at 5T for a strain of 1-2. Further wire drawing decreased the magnitude of the pinning force but continued to shift the peak in the pinning force curve to higher reduced fields. Thus, a good portion of the samples in this experiment were past their optimum size for critical current density.

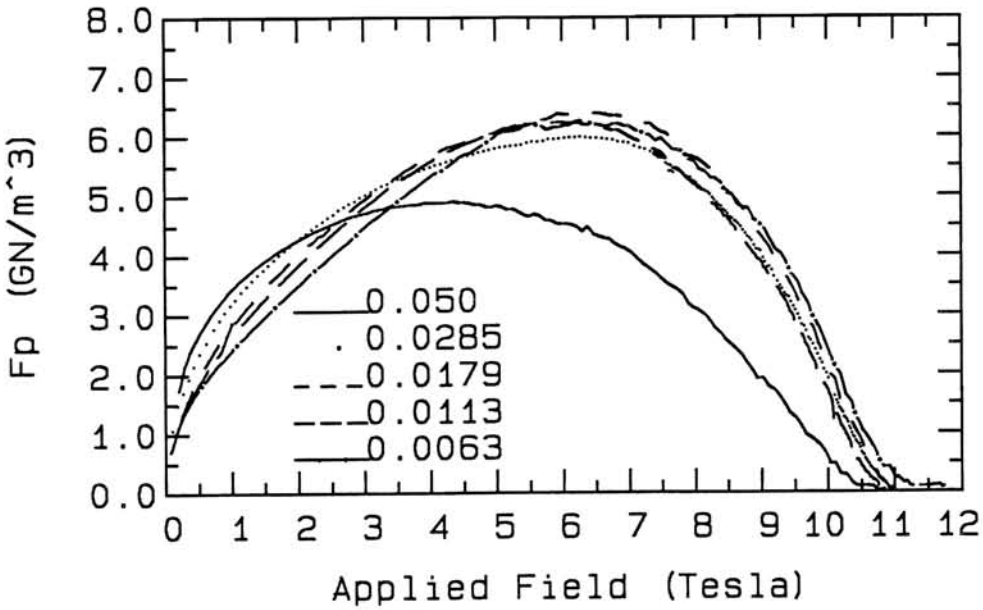

Figure 5.21: The pinning force (F_p) versus the applied field for Nb44wt%Ti (UW1719) near 4K. d=0.050" - T=4.14K, d=0.0285" - T=4.06K, d=0.0179" - T=4.15K, d=0.0113" - T=4.19, d=0.0063 - T=4.13K.

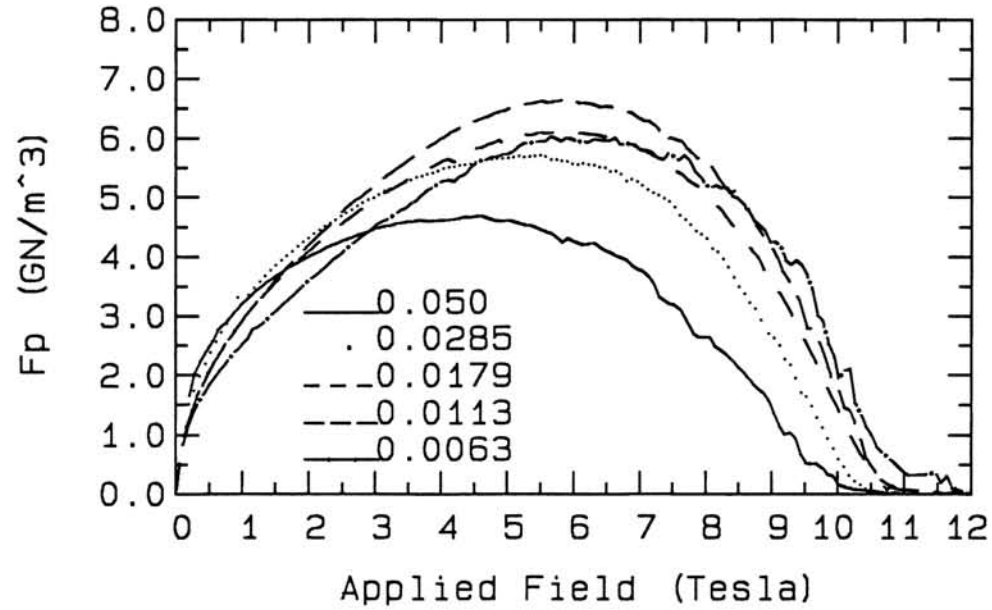

Figure 5.22: The pinning force (F_p) versus the applied field for Nb46.5wt%Ti (UW2119) near 4K. d=0.050" - T=4.16K, d=0.0285" - T=4.34K, d=0.0179" - T=4.14K, d=0.0113" - T=4.16, d=0.0063 - T=4.09K.

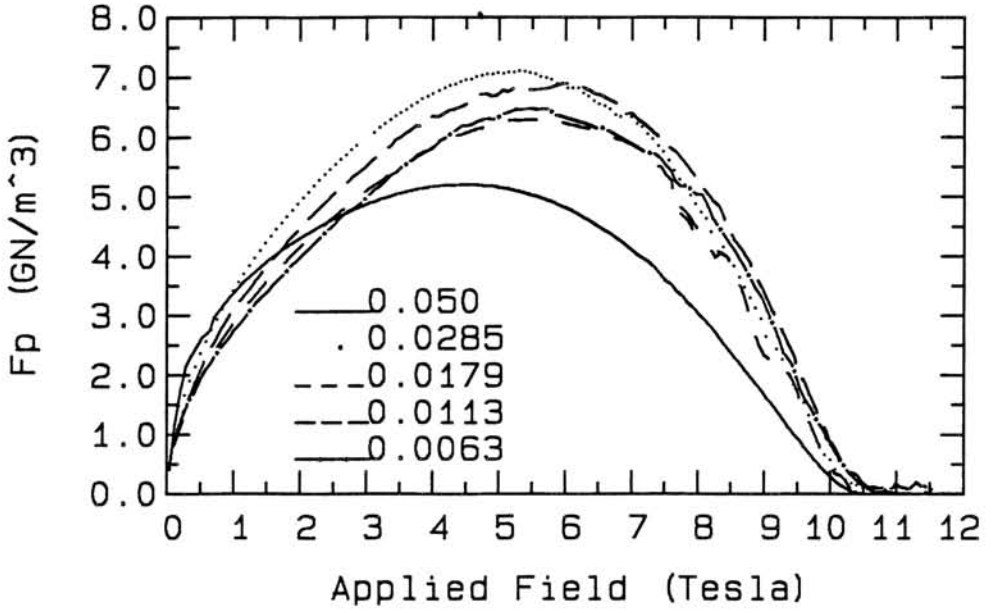

Figure 5.23: The pinning force (F_p) versus the applied field for Nb49wt%Ti (UW2219) near 4K. d=0.050" - T=4.08K, d=0.0285" - T=4.11K, d=0.0179" - T=4.16K, d=0.0113" - T=4.17, d=0.0063 - T=4.13K.

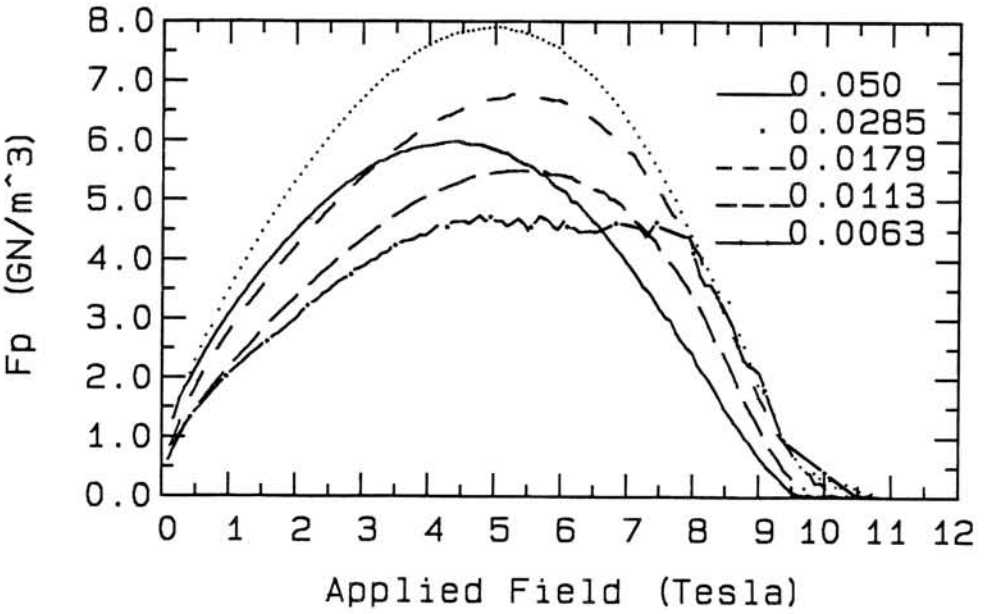

Figure 5.24: The pinning force (F_p) versus the applied field for Nb52wt%Ti (UW3419) near 4K. d=0.050" - T=4.17K, d=0.0285" - T=4.13K, d=0.0179" - T=4.12K, d=0.0113" - T=4.12, d=0.0063 - T=4.15K.

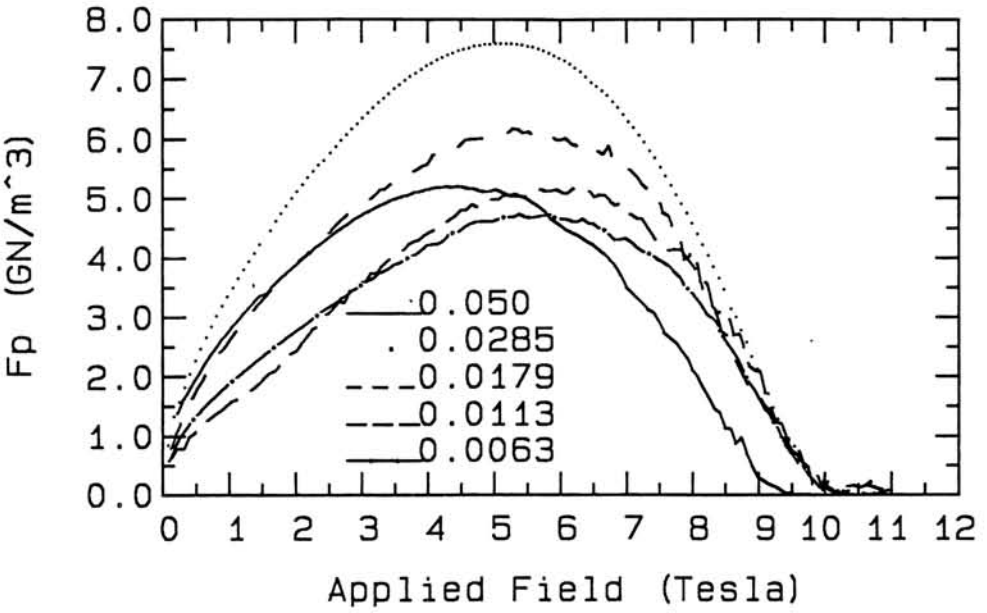

Figure 5.25: The pinning force (F_p) versus the applied field for Nb53wt%Ti (UW2319) near 4K. d=0.050" - T=4.16K, d=0.0285" - T=4.17K, d=0.0179" - T=4.02K, d=0.0113" - T=4.15, d=0.0063 - T=4.15K.

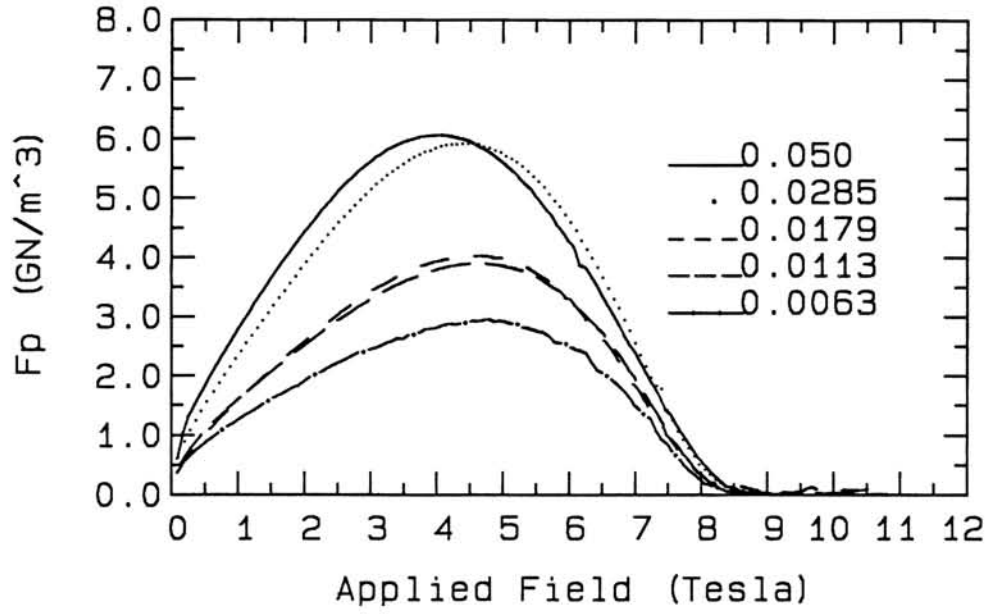

Figure 5.26: The pinning force (F_p) versus the applied field for Nb58wt%Ti (UW2419) near 4K. d=0.050" - T=4.12K, d=0.0285" - T=4.14K, d=0.0179" - T=4.15K, d=0.0113" - T=4.13, d=0.0063 - T=4.11K.

5.2.5 Reduced Pinning Force Results.

The reduced pinning force results from this study are extensive. The availability of data at constant H_{c_2} across the alloy range and with increasing strain, allows observation of the subtle systematic changes which occur with increasing Ti content and cold work. The data shown in this section is for samples after heat treatment, after a strain of 2.05, and after a strain of 4.14, with the exception of UW2119 which is shown at ϵ_f=0, 1, 2, 3, and 4.

Several major trends can be seen in the reduced pinning force results(figures 5.27-5.47). The first trend was that with increasing cold work following the heat treatment, the peak in the curve shifted to higher reduced fields. This shift was also observed by Küpfer and Matsushita and by Meingast and Larbalestier [34, 62]. The second major trend was that as the temperature was increased, the peak in the curve shifted toward lower field. This effect was small for Nb44wt%Ti but very pronounced for Nb62wt%Ti. The final trend is an artifact of measurement. As the wire size decreased, the noise level increased. This was due not only to the decreasing volume of sample present but also to the reduction in the filament diameter since in equation 4.4 the magnetic moment goes as r^3.

In addition to the reduced pinning force curves presented on the wire, values of the maximum pinning force ($F_{p_{max}}$), the upper critical field (H_{c_2}), the

actual measurement temperature for each trace, and the scaling coefficients (C, n, m, b_p) calculated for each trace are tabulated. The scaling coefficients were obtained by doing a non-linear least squares fit to the equation

$$f_p = Cb^n(1-b)^m \tag{5.1}$$

by an iterative method. The reduced field where the peak in the pinning force occurs (b_p) was calculated in each case from the derivative of equation 5.1 with respect to b. In each case, the standard deviation (σ) of the fit was computed to allow an estimate in each case of the goodness of fit. Thus, coefficients with large σ values ($\sigma > 0.08$) are probably not representative of the data. A detailed description of the method and program used for the curve fits is listed in the appendix.

UW1719 - Nb44wt%Ti

Figures 5.27 to 5.29 show the reduced pinning force curves for the Nb44-wt%Ti alloy. The most noticeable thing about these curves was the lack of scaling for the after heat treatment wire (0.050") and the wire which received a final strain of 2 (0.0179"). The smallest wire (ϵ_f= 4, d=0.0063") was the closest to exhibiting scaling behavior of any of the wires in this study. The only curve in figure 5.29 which deviated significantly from the others was the high temperature curve. The similarity of curve shape for the four colder curves in figure 5.29 can also be seen in the fit coefficients listed in table 5.1.

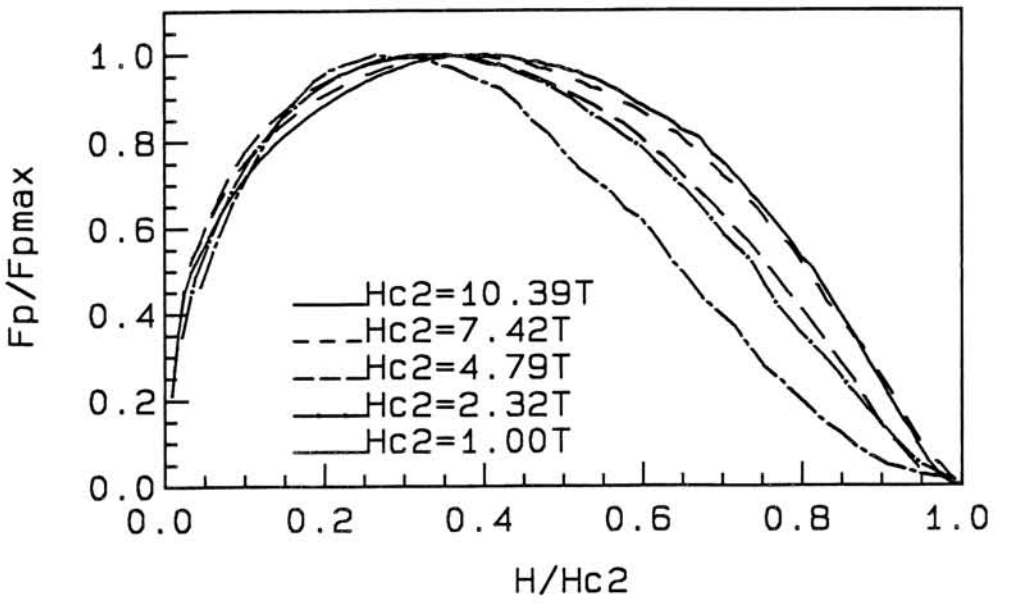

Figure 5.27: Reduced pinning force versus reduced field for UW1719 0.050" (Nb44wt%Ti) after heat treatment.

This table also lists the measurement temperatures, upper critical field and maximum value of F_p for each reduced pinning force curve.

UW2119 - Nb46.5wt%Ti

Figures 5.30 to 5.34 show the reduced pinning force curves for Nb46.5wt%Ti at strain intervals of 1. With the small increase in Ti content, the pinning force curves following heat treatment of Nb46.5wt%Ti were already shifted toward lower reduced field relative to those of Nb44wt%Ti following heat treatment. Cold working the wires following heat treatment caused the pinning force curves to gradually move toward higher reduced field. This can be seen readily if the figures are overlaid. Similar to the behavior of the

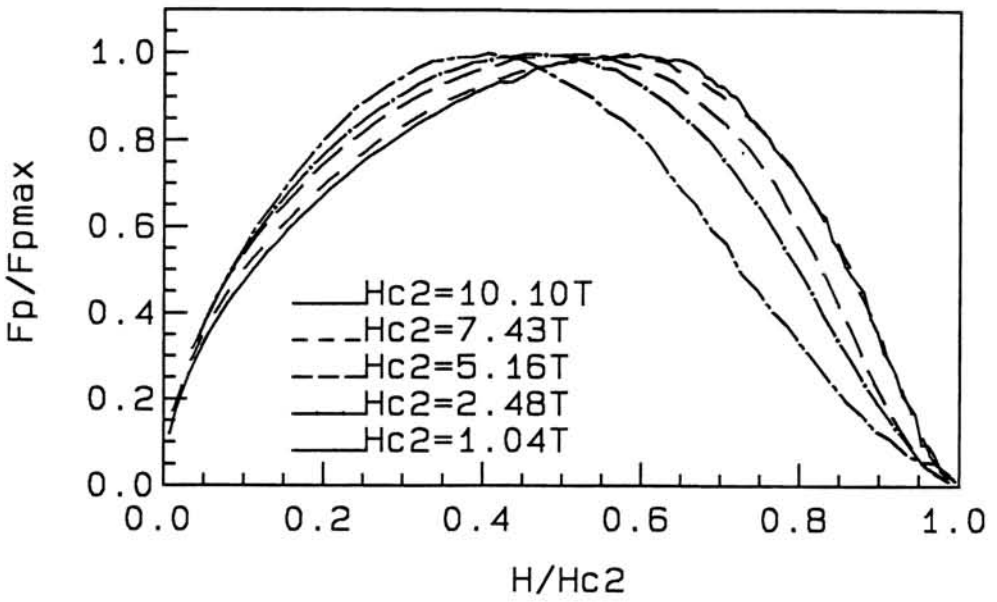

Figure 5.28: Reduced pinning force versus reduced field for UW1719 0.0179" (Nb44wt%Ti) with one heat treatment and $\epsilon_f = 2.05$.

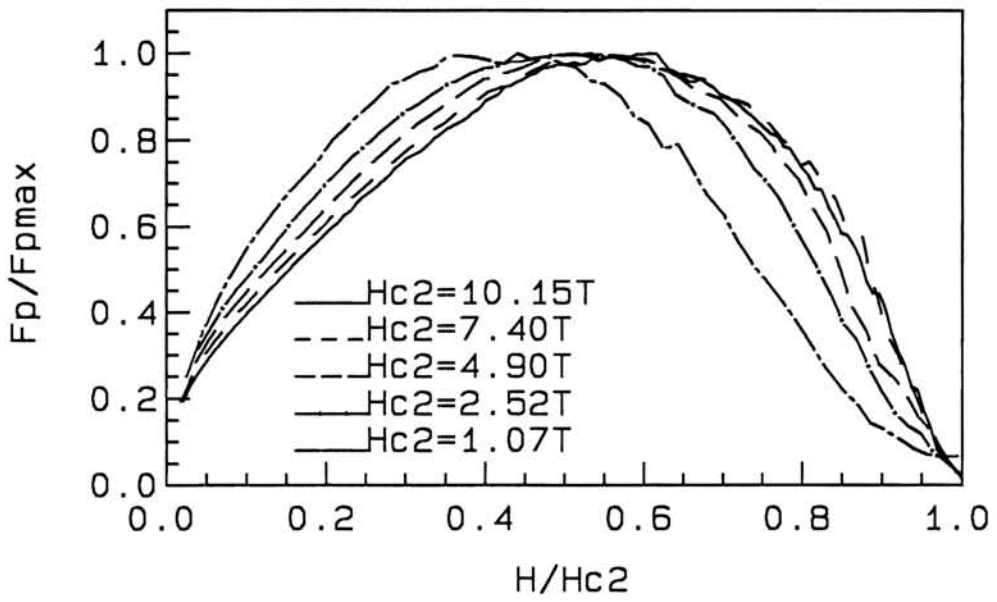

Figure 5.29: Reduced pinning force versus reduced field for UW1719 0.0063" (Nb44wt%Ti) with one heat treatment and $\epsilon_f = 4.14$.

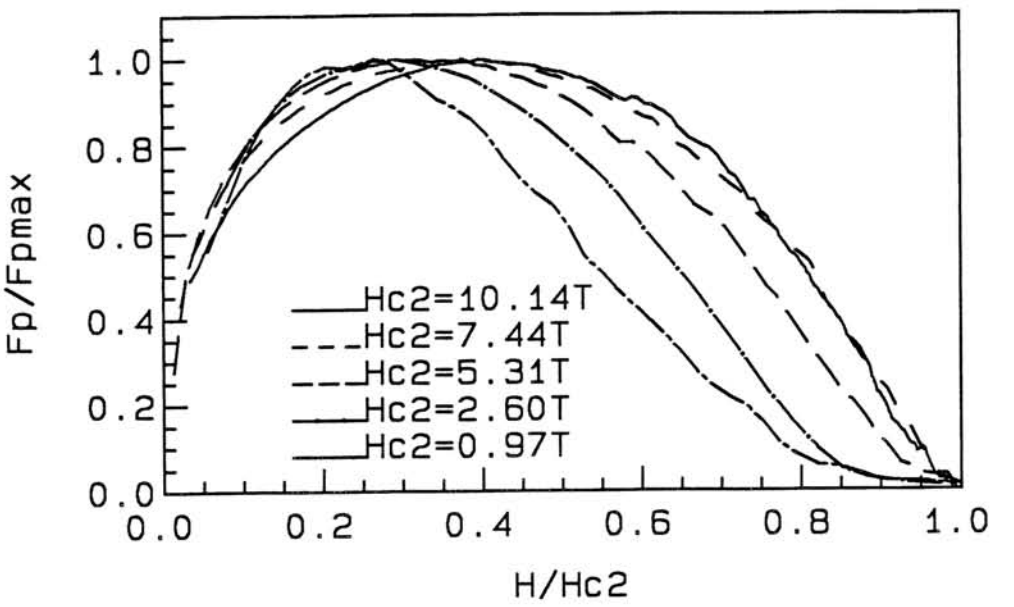

Figure 5.30: Reduced pinning force versus reduced field for UW2119 0.050" (Nb46.5wt%Ti) after heat treatment.

other wires in this experiment, the curves shifted toward lower reduced fields with increasing temperature. This can easily be seen in figure 5.34. The shift toward lower field with increasing temperature was similar to the observations of Meingast and Larbalestier [62]. However, the shift was more pronounced for their Nb48wt%Ti alloy than for this Nb46.5wt%Ti alloy. The measurement temperatures, upper critical field, maximum pinning force and fit coefficients for Nb46.5wt%Ti are listed in table 5.2.

UW2219 -Nb49wt%Ti

The high temperature reduced pinning force curve for Nb49wt%Ti following the heat treatment had its peak at extremely low reduced field ($b_p \approx .12$)

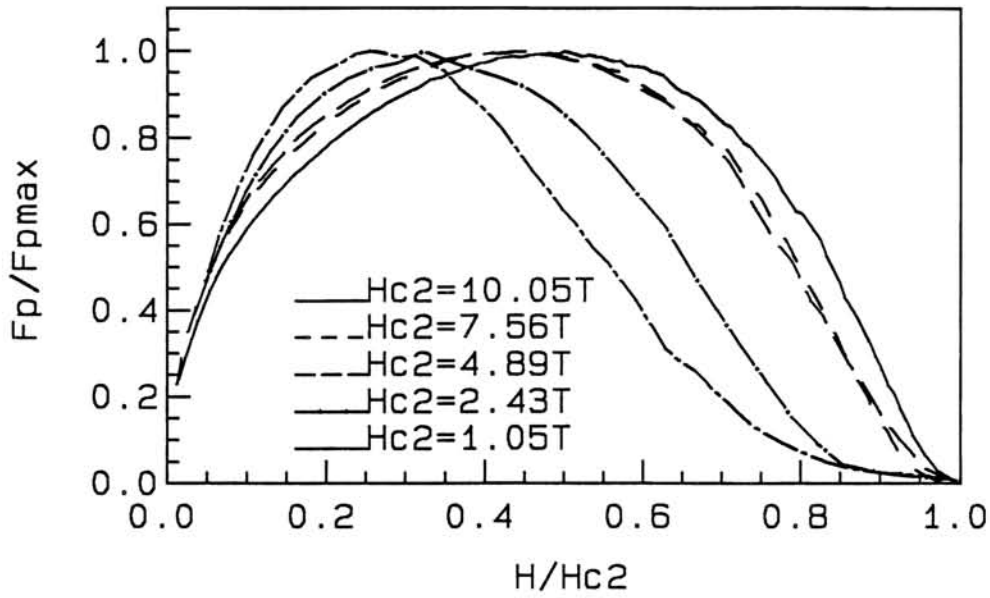

Figure 5.31: Reduced pinning force versus reduced field for UW2119 0.0285" (Nb46.5wt%Ti) with one heat treatment and $\epsilon_f = 1.12$.

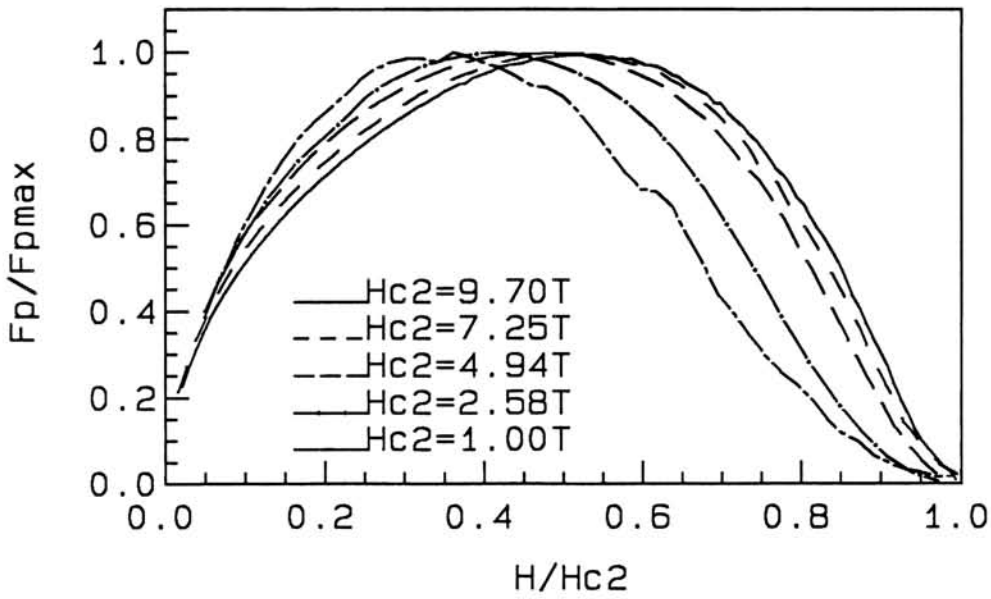

Figure 5.32: Reduced pinning force versus reduced field for UW2119 0.0179" (Nb46.5wt%Ti) with one heat treatment and $\epsilon_f = 2.05$.

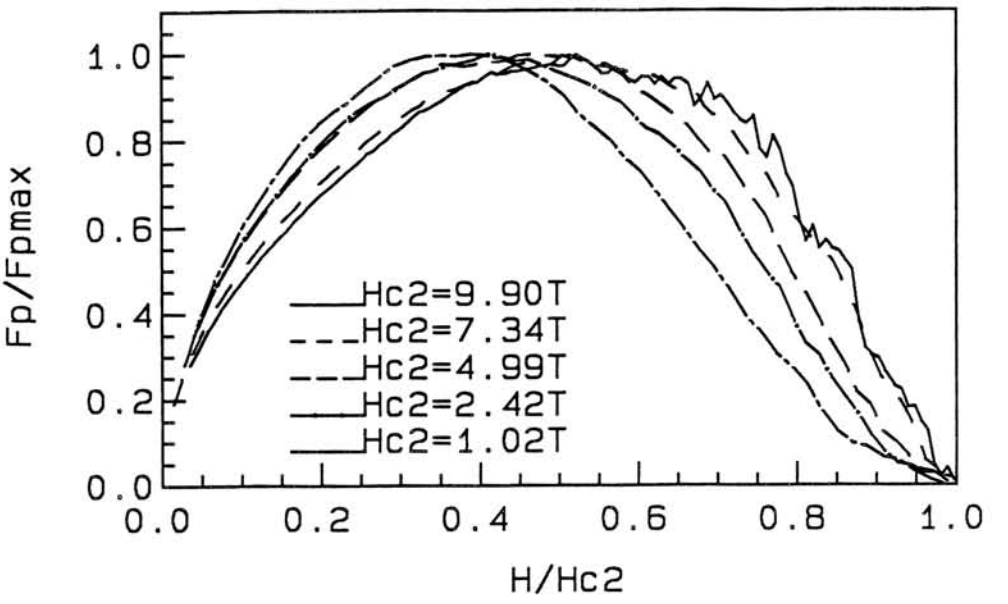

Figure 5.33: Reduced pinning force versus reduced field for UW2119 0.0113" (Nb46.5wt%Ti) with one heat treatment and $\epsilon_f = 2.97$.

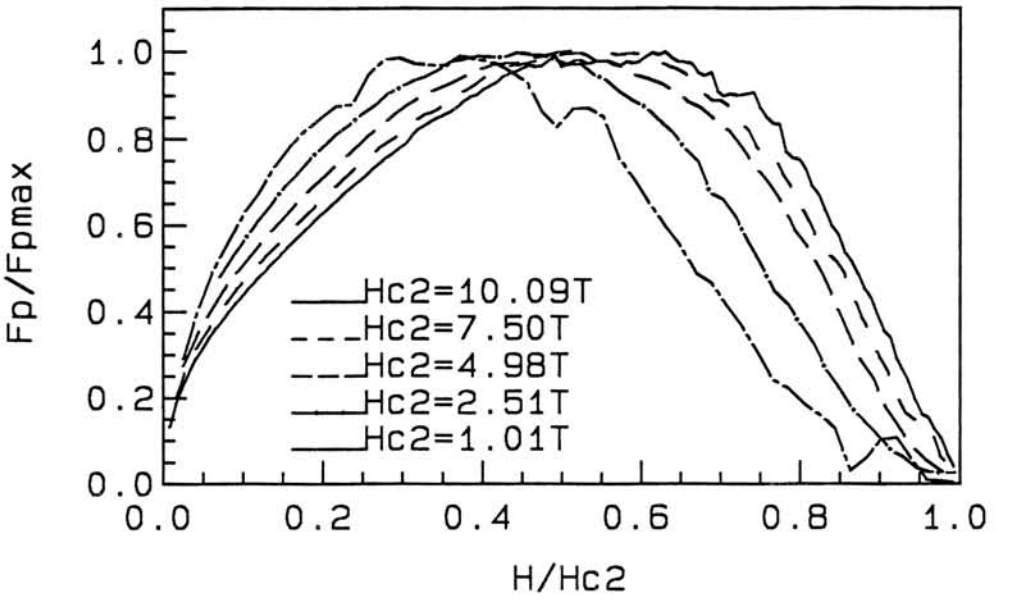

Figure 5.34: Reduced pinning force versus reduced field for UW2119 0.0063" (Nb46.5wt%Ti) with one heat treatment and $\epsilon_f = 4.14$.

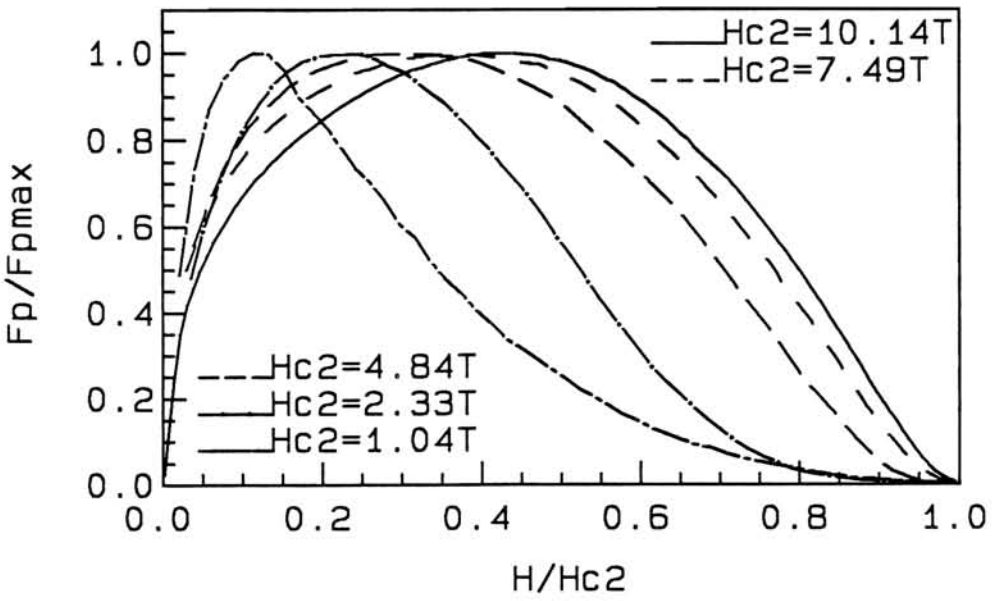

Figure 5.35: Reduced pinning force versus reduced field for UW2219 0.050" (Nb49wt%Ti) after heat treatment.

(see figures 5.35 to 5.37). Following a strain of 4, the high temperature peak shifted up considerably in reduced field ($b_p \approx .26$). The cold work following heat treatment also affected the low temperature measurements taking them from non-scaling following heat treatment to nearly indistinguishable curve shapes at a strain of 4 (figure 5.37). This scaling was limited to low temperatures and breaks down as the temperature is increased.

UW3419 - Nb52wt%Ti

The reduced pinning force curves for UW3419 are shown in figures 5.38 to 5.40. The trends typical of the rest of the alloys can be seen in these curves. Following the heat treatment the reduced pinning force curves were

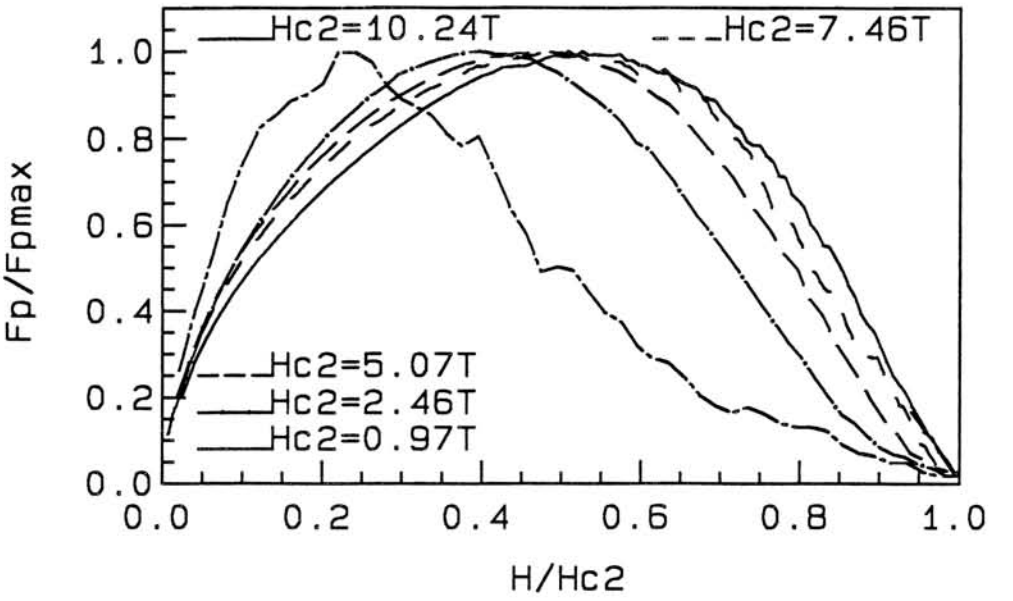

Figure 5.36: Reduced pinning force versus reduced field for UW2219 0.0179" (Nb49wt%Ti) with one heat treatment and $\epsilon_f = 2.05$.

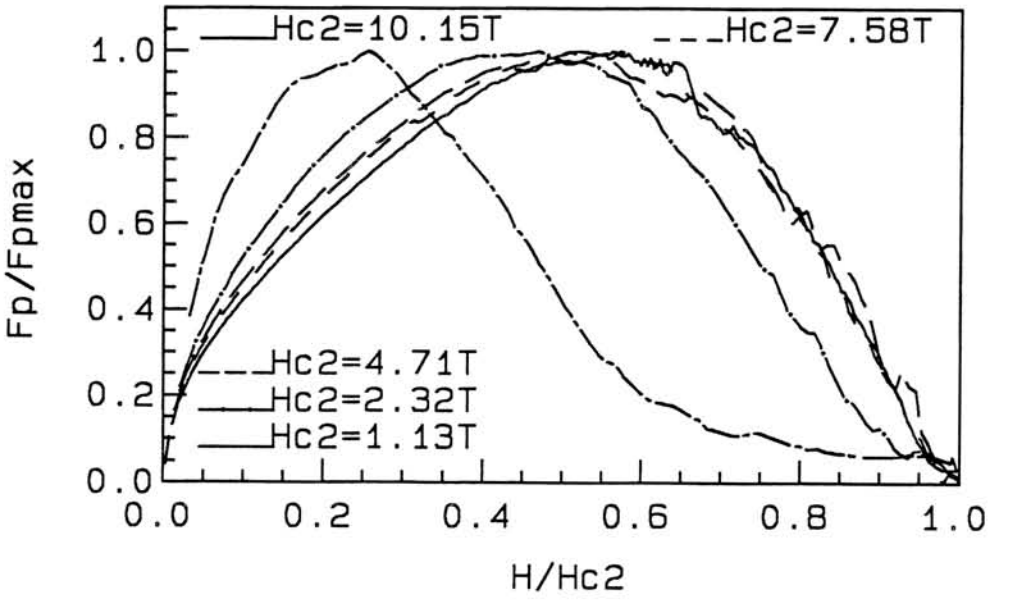

Figure 5.37: Reduced pinning force versus reduced field for UW2219 0.0063" (Nb49wt%Ti) with one heat treatment and $\epsilon_f = 4.14$.

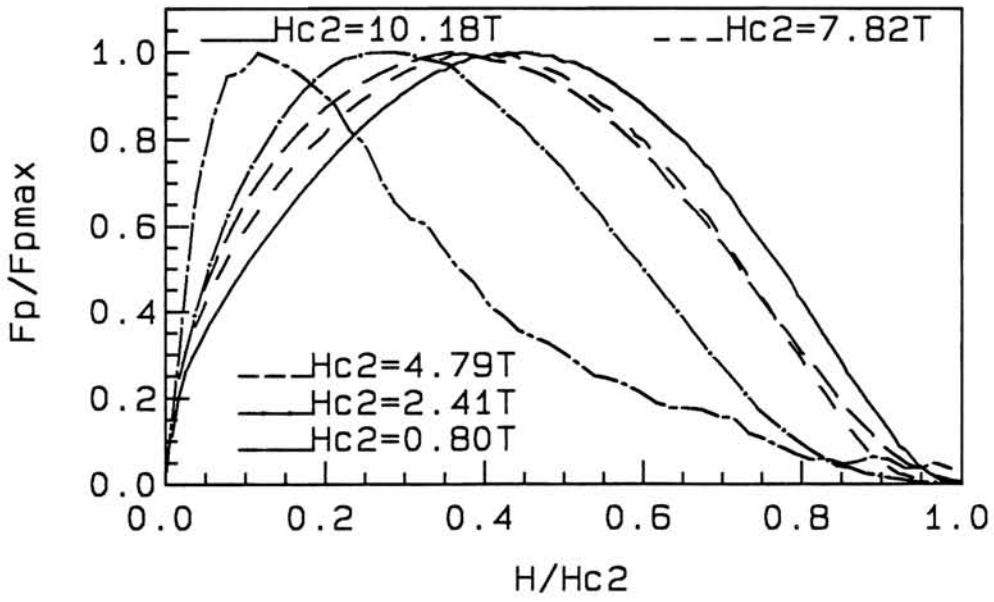

Figure 5.38: Reduced pinning force versus reduced field for UW3419 0.050" (Nb52wt%Ti) after heat treatment.

shifted toward lower field. Cold work caused the curves to shift toward higher field. None of the wires showed any indication of scaling behavior, the trend was a shift toward lower field with increasing temperature. The upper critical field, measurement temperature, maximum pinning force, and the scaling coefficients for this alloy are listed in table 5.4.

UW2319 - Nb53wt%Ti

As seen in figures 5.41 to 5.43 some of the noisiest magnetization loops of the whole experiment occurred for the wire from this alloy. Even with the noise in these traces, the lack of scaling and the similarity to the reduced pinning force curves of Nb52wt%Ti (as listed in table 2.1 the actual compositional

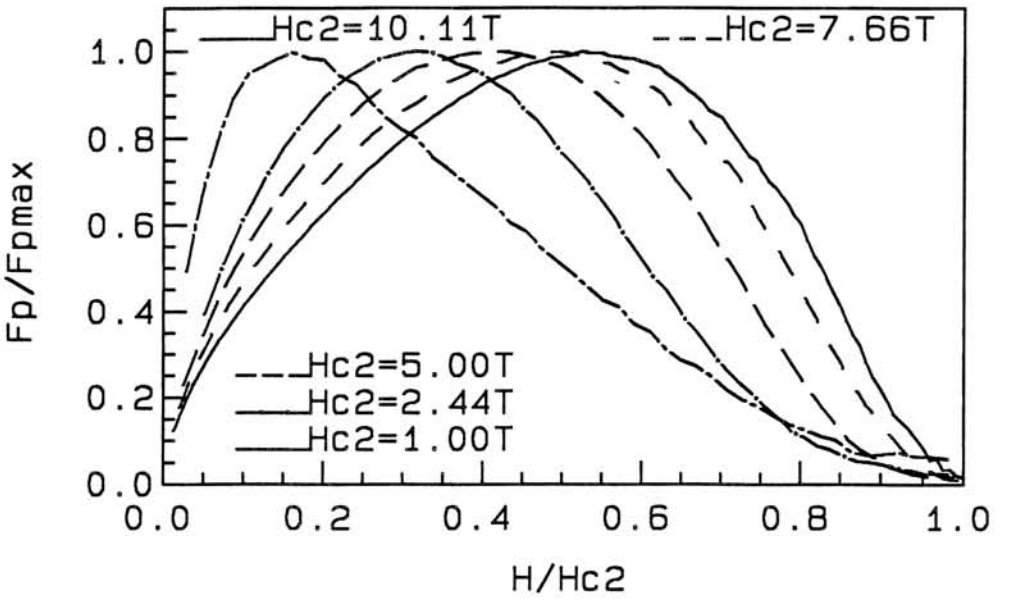

Figure 5.39: Reduced pinning force versus reduced field for UW3419 0.0179" (Nb52wt%Ti) with one heat treatment and $\epsilon_f = 2.05$.

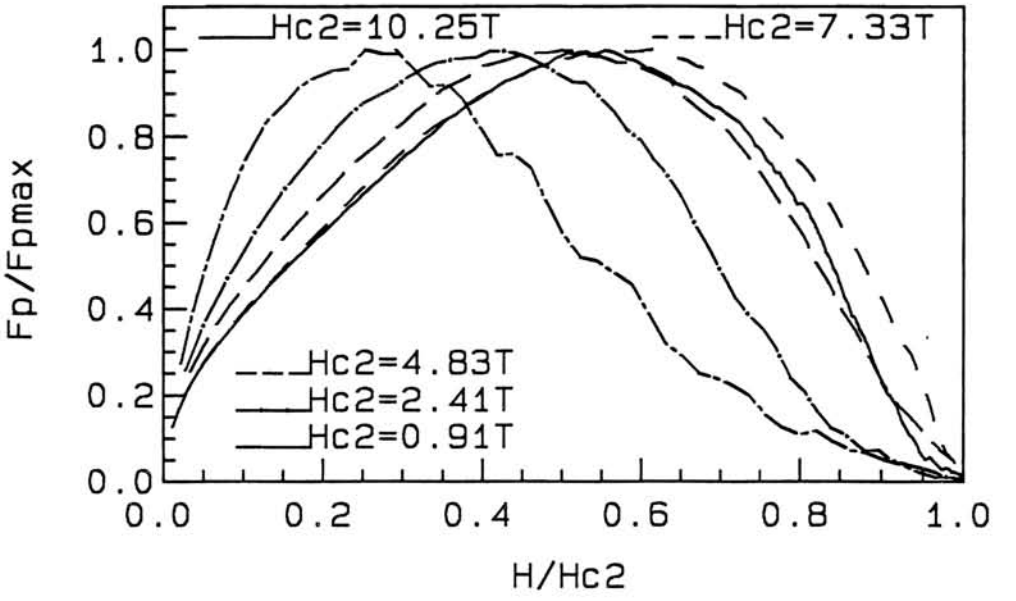

Figure 5.40: Reduced pinning force versus reduced field for UW3419 0.0063" (Nb52wt%Ti) with one heat treatment and $\epsilon_f = 4.14$.

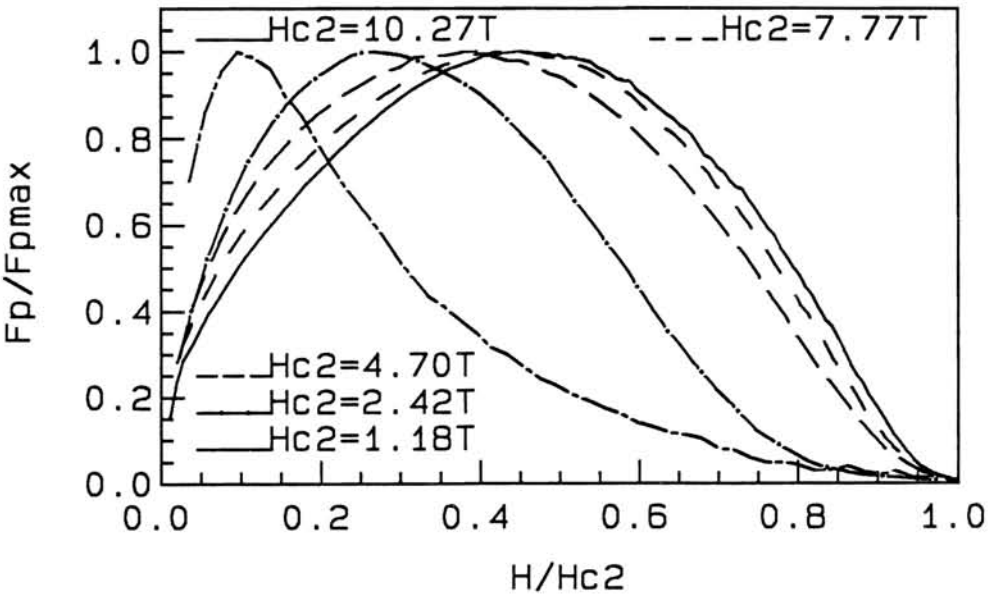

Figure 5.41: Reduced pinning force versus reduced field for UW2319 0.050" (Nb53wt%Ti) after heat treatment.

difference in these two alloys is only 0.1wt%Ti) can be easily seen. The high noise level can also be seen by examining the standard deviations listed the scaling coefficients in table 5.5. A ranking of the fits based on the standard deviation had a fair number of UW2319 entries for the high end of the standard deviation scale. Also listed in table 5.5 are the measurement temperatures, H_{c_2} and $F_{p_{max}}$ for each wire.

UW2419 - Nb58wt%Ti

Figures 5.44 to 5.46 show the reduced pinning force curves for the Nb58wt%-Ti alloy. Although the general trend of a shift in b_p toward higher field with increasing cold work was observed in this alloy, it was not as pronounced as in

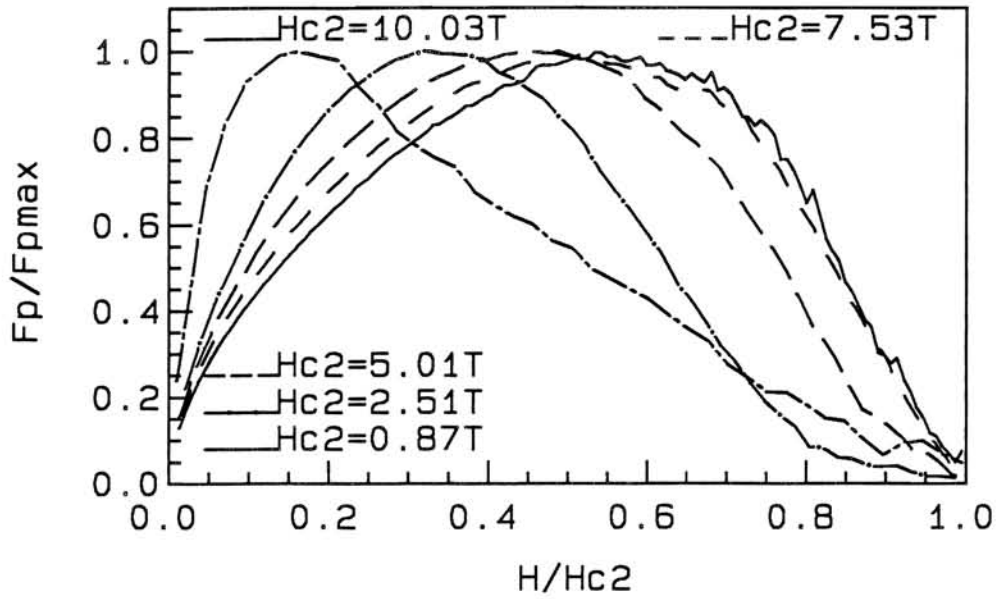

Figure 5.42: Reduced pinning force versus reduced field for UW2319 0.0179" (Nb53wt%Ti) with one heat treatment and $\epsilon_f = 2.05$.

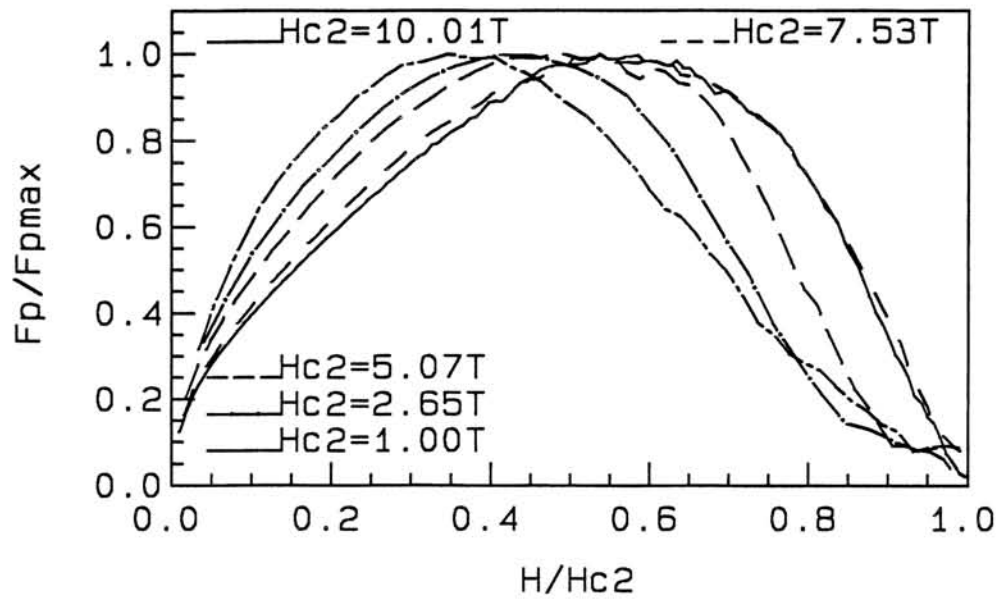

Figure 5.43: Reduced pinning force versus reduced field for UW2319 0.0063" (Nb53wt%Ti) with one heat treatment and $\epsilon_f = 4.14$.

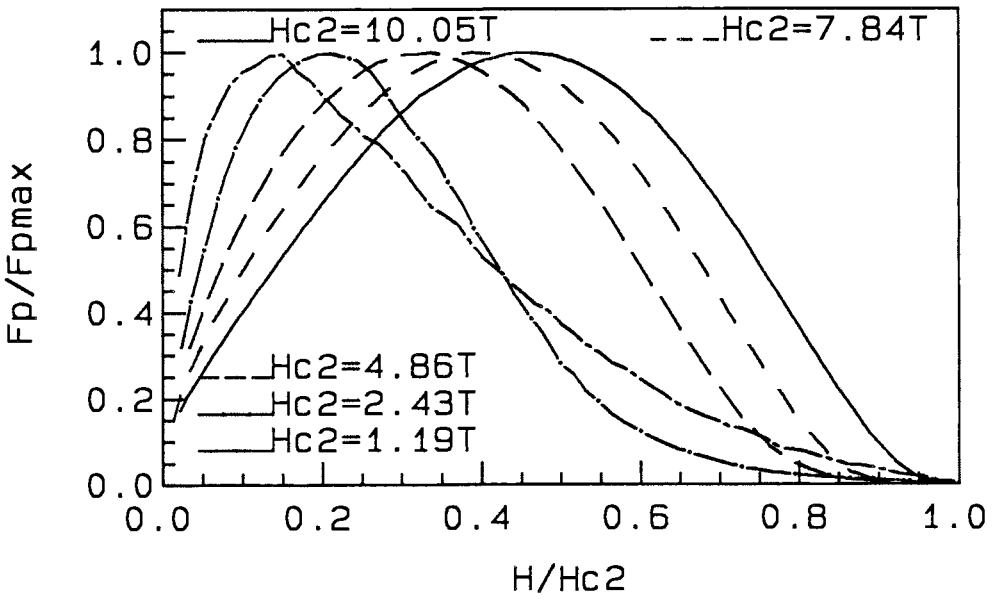

Figure 5.44: Reduced pinning force versus reduced field for UW2419 0.050" (Nb58wt%Ti) after heat treatment.

the rest of the alloys. The high temperature curve (H_{c_2}(T) $\approx$ 1T) remained at low reduced field throughout all the wire drawing. The coefficients of fits to the reduced pinning force curves, the measurement temperatures, H_{c_2} and $F_{p_{max}}$ are listed in table 5.6.

UW1819 - Nb62wt%Ti.

As discussed in section 2.4, this wire was too brittle to draw following heat treatment. Thus reduced pinning force data was available only following heat treatment (see figure 5.47). For Nb62wt%Ti both the curves for $H_{c_2} \approx$ 1T and $H_{c_2} \approx$ 2.5T peak at low field. In the lower Ti content alloys only the $H_{c_2} \approx$ 1T curve was shifted to very low reduced fields. Reducing the temperatures

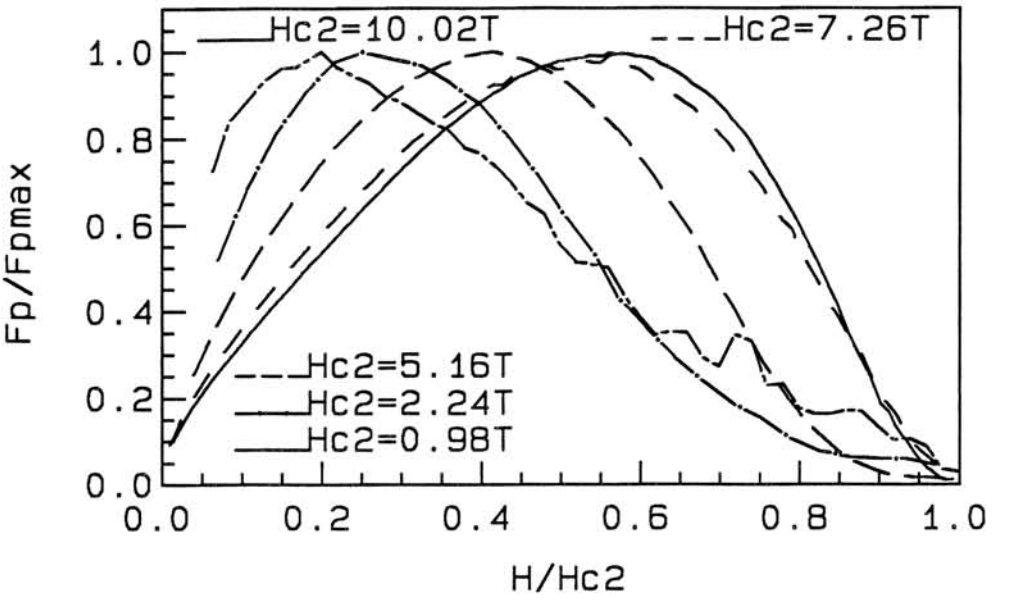

Figure 5.45: Reduced pinning force versus reduced field for UW2419 0.0179" (Nb58wt%Ti) with one heat treatment and $\epsilon_f = 2.05$.

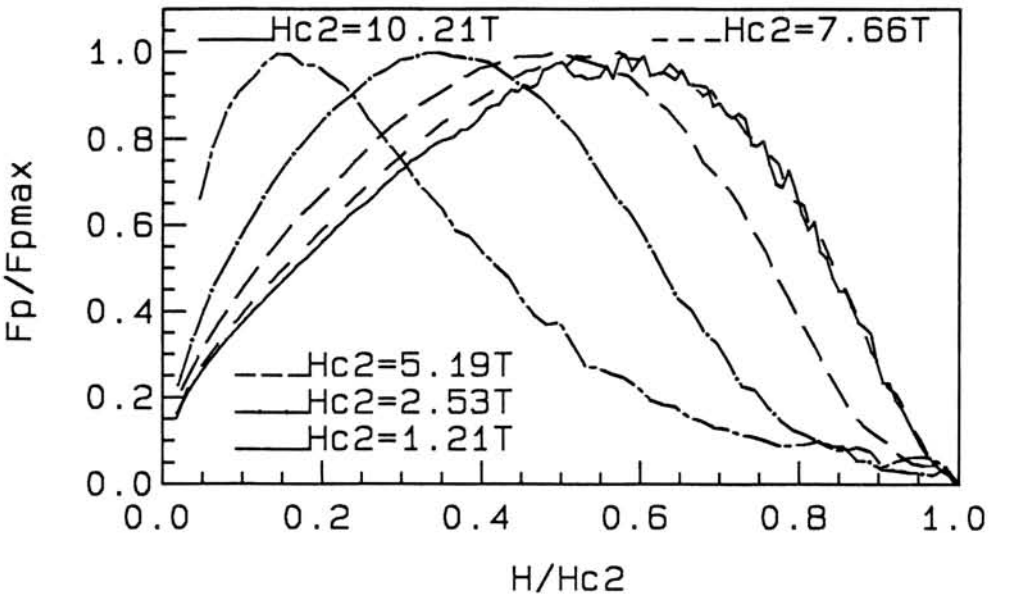

Figure 5.46: Reduced pinning force versus reduced field for UW2419 0.0063" (Nb58wt%Ti) with one heat treatment and $\epsilon_f = 4.14$.

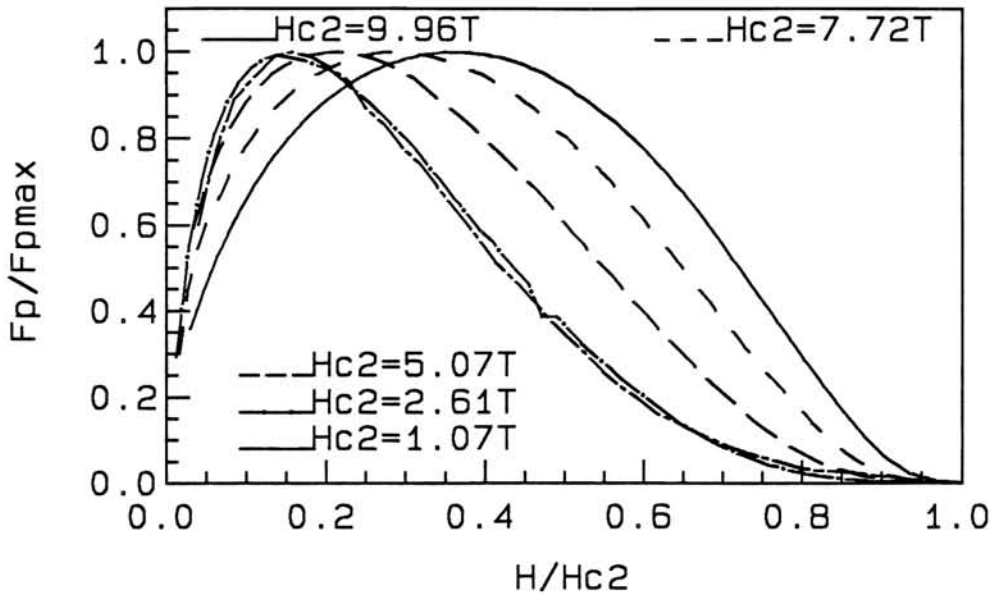

Figure 5.47: Reduced pinning force versus reduced field for UW1819 0.050" (Nb62wt%Ti) after heat treatment.

caused the curves to shift to higher field but the peak in the $H_{c_2} \approx$ 10T curve for Nb62wt%Ti was substantially lower in reduced field (b_p=.35) than Nb58-wt%Ti (b_p=.46). The tabulated values for the peak in the pinning force, the upper critical field and the fit coefficients are listed in table 5.6

5.3 Summary

In the standard experiment the peak in the pinning force curve shifted to lower field with increasing Ti content. As shown in section 3.5, the increasing Ti content was accompanied by a large change in the percentage of α -Ti precipitate in the wires for the standard experiment. By controlling the pre-

cipitation in the isomorphology experiment the shift to low field was avoided in the high Ti alloys at low temperatures ($H_{c_2} \approx 10$T). However, as the temperature was increased, the peak in the pinning force curve shifted to low reduced fields for the high Ti content alloys. This shift to lower fields was partially counteracted by cold working the wires after the precipitation heat treatment, but as the Ti content was increased cold work was less effective at preventing the shift toward low reduced field. The final feature of all these wires is the unmistakable lack of scaling which will be taken up in the discussion chapter.

Table 5.1: The upper critical field, maximum pinning force, calculated peak field, and scaling coefficients for the Nb44wt% Ti wires (UW1719).

Size (in)	Temp	H_{c_2}(T)	$F_{p_{max}}(N/m^3)$	b_p	C	n	m	σ
0.0063	4.75K	10.15	5.10×10^9	0.53	3.4	0.96	0.84	0.043
0.0063	6.11K	7.40	2.48×10^9	0.53	3.3	0.92	0.82	0.047
0.0063	7.35K	4.90	9.88×10^8	0.50	3.8	0.96	0.97	0.047
0.0063	8.34K	2.52	2.48×10^8	0.46	4.2	0.94	1.11	0.043
0.0063	8.90K	1.07	4.70×10^7	0.39	5.2	0.95	1.50	0.037
0.0113	4.73K	10.08	5.08×10^9	0.49	3.7	0.93	0.97	0.044
0.0113	6.11K	7.48	2.52×10^9	0.46	4.0	0.92	1.09	0.048
0.0113	7.33K	4.99	1.09×10^9	0.45	3.8	0.87	1.05	0.044
0.0113	8.38K	2.41	2.69×10^8	0.43	4.6	0.94	1.26	0.032
0.0113	8.97K	0.95	4.53×10^7	0.35	5.8	0.95	1.76	0.031
0.0179	4.78K	10.10	5.19×10^9	0.50	3.1	0.82	0.83	0.053
0.0179	6.10K	7.43	2.66×10^9	0.49	3.0	0.78	0.82	0.051
0.0179	7.27K	5.16	1.17×10^9	0.45	3.7	0.84	1.04	0.052
0.0179	8.36K	2.48	3.08×10^8	0.42	4.0	0.84	1.16	0.038
0.0179	8.93K	1.04	6.69×10^7	0.38	5.8	0.99	1.63	0.026
0.0285	4.77K	10.15	4.78×10^9	0.45	3.0	0.71	0.86	0.062
0.0285	6.08K	7.58	2.60×10^9	0.44	2.8	0.66	0.85	0.057
0.0285	7.38K	4.92	1.09×10^9	0.40	3.3	0.70	1.04	0.051
0.0285	8.36K	2.44	3.15×10^8	0.37	4.3	0.80	1.36	0.040
0.0285	9.03K	1.00	5.72×10^7	0.28	7.7	0.96	2.49	0.018
0.050AHT	4.30K	10.39	4.72×10^9	0.37	2.8	0.55	0.96	0.034
0.050AHT	5.88K	7.42	2.53×10^9	0.35	2.5	0.50	0.93	0.026
0.050AHT	7.33K	4.79	1.07×10^9	0.31	2.7	0.50	1.09	0.027
0.050AHT	8.37K	2.32	3.24×10^8	0.32	3.4	0.61	1.29	0.019
0.050AHT	8.94K	1.00	7.19×10^7	0.28	4.5	0.71	1.81	0.009

Table 5.2: The upper critical field, maximum pinning force, calculated peak field, and scaling coefficients for the Nb46.5wt% Ti wires (UW2119).

Size (in)	Temp.	H_{c_2}(T)	$F_{p_{max}}(N/m^3)$	b_p	C	n	m	σ
0.0063	4.66K	10.09	5.06×10^9	0.52	3.0	0.84	0.79	0.048
0.0063	6.03K	7.50	2.48×10^9	0.49	3.5	0.88	0.93	0.049
0.0063	7.21K	4.98	1.00×10^9	0.45	3.9	0.89	1.09	0.051
0.0063	8.20K	2.51	2.39×10^8	0.40	5.5	0.99	1.51	0.042
0.0063	8.75K	1.01	4.38×10^7	0.33	7.0	1.00	2.04	0.049
0.0113	4.70K	9.90	5.36×10^9	0.49	3.5	0.88	0.93	0.046
0.0113	6.06K	7.34	2.72×10^9	0.47	3.5	0.84	0.97	0.043
0.0113	7.23K	4.99	1.13×10^9	0.41	4.2	0.86	1.22	0.044
0.0113	8.22K	2.42	3.00×10^8	0.39	4.8	0.91	1.42	0.038
0.0113	8.77K	1.02	6.11×10^7	0.35	6.6	1.00	1.88	0.032
0.0179	4.86K	9.70	4.76×10^9	0.47	3.3	0.81	0.92	0.046
0.0179	6.10K	7.25	2.51×10^9	0.45	3.4	0.80	0.98	0.047
0.0179	7.23K	4.94	1.14×10^9	0.42	3.8	0.82	1.12	0.046
0.0179	8.23K	2.58	3.34×10^8	0.38	5.4	0.94	1.56	0.043
0.0179	8.77K	1.00	6.29×10^7	0.34	7.1	1.01	2.01	0.029
0.0285	4.69K	10.05	5.07×10^9	0.43	3.1	0.71	0.92	0.047
0.0285	6.10K	7.56	2.60×10^9	0.39	3.6	0.72	1.13	0.055
0.0285	7.29K	4.89	1.20×10^9	0.39	3.6	0.72	1.15	0.045
0.0285	8.37K	2.43	2.99×10^8	0.30	6.6	0.92	2.10	0.043
0.0285	8.87K	1.05	6.24×10^7	0.25	8.9	0.97	2.87	0.017
0.050AHT	4.41K	10.14	4.37×10^9	0.37	3.1	0.62	1.05	0.039
0.050AHT	5.76K	7.44	2.45×10^9	0.35	2.5	0.48	0.92	0.028
0.050AHT	6.96K	5.31	1.24×10^9	0.30	2.8	0.50	1.16	0.030
0.050AHT	8.20K	2.60	3.39×10^8	0.28	5.2	0.76	1.98	0.033
0.050AHT	8.80K	0.97	5.98×10^7	0.25	9.4	0.99	2.94	0.028

Table 5.3: The upper critical field, maximum pinning force, calculated peak field, and scaling coefficients for the Nb49wt% Ti wires (UW2219).

Size (in)	Temp.	H_{c_2}(T)	$F_{p_{max}}(N/m^3)$	b_p	C	n	m	σ
0.0063	4.37K	10.15	5.69×10^9	0.49	4.0	1.00	1.04	0.048
0.0063	5.70K	7.58	2.88×10^9	0.48	4.0	0.96	1.05	0.045
0.0063	6.93K	4.71	1.19×10^9	0.48	3.5	0.87	0.96	0.040
0.0063	7.95K	2.32	2.72×10^8	0.40	5.4	0.99	1.48	0.042
0.0063	8.56K	1.13	3.35×10^7	0.22	21.2	1.27	4.42	0.048
0.0113	4.52K	10.03	6.16×10^9	0.48	3.7	0.91	0.99	0.043
0.0113	5.90K	7.28	3.07×10^9	0.45	4.1	0.92	1.14	0.041
0.0113	7.04K	4.71	1.36×10^9	0.43	4.1	0.89	1.17	0.036
0.0113	7.99K	2.43	3.82×10^8	0.38	5.6	0.97	1.62	0.031
0.0113	8.61K	1.22	4.96×10^7	0.22	13.4	1.08	3.79	0.047
0.0179	4.34K	10.24	6.00×10^9	0.48	3.5	0.87	0.94	0.036
0.0179	5.68K	7.46	3.10×10^9	0.45	3.7	0.84	1.04	0.040
0.0179	6.95K	5.07	1.43×10^9	0.42	4.3	0.90	1.24	0.042
0.0179	8.02K	2.46	3.90×10^8	0.37	5.9	0.99	1.69	0.030
0.0179	8.66K	0.98	4.28×10^7	0.23	7.8	0.89	2.99	0.038
0.0285	4.62K	9.80	5.88×10^9	0.44	4.1	0.89	1.15	0.045
0.0285	5.98K	7.22	3.11×10^9	0.40	4.3	0.85	1.29	0.047
0.0285	7.18K	4.81	1.39×10^9	0.36	5.3	0.90	1.60	0.046
0.0285	8.26K	2.40	3.12×10^8	0.26	10.5	1.04	3.02	0.027
0.0285	8.80K	1.27	2.96×10^7	0.16	2.2	0.33	1.67	0.061
0.050AHT	4.27K	10.14	4.92×10^9	0.38	3.1	0.64	1.06	0.036
0.050AHT	5.73K	7.49	2.65×10^9	0.33	3.2	0.59	1.18	0.037
0.050AHT	7.05K	4.84	1.17×10^9	0.29	3.7	0.61	1.50	0.033
0.050AHT	8.18K	2.33	2.75×10^8	0.22	9.5	0.93	3.24	0.027
0.050AHT	8.78K	1.04	1.54×10^7	0.13	6.1	0.61	4.26	0.034

Table 5.4: The upper critical field, maximum pinning force, calculated peak field, and scaling coefficients for the Nb52wt% Ti wires (UW3419).

Size (in)	Temp.	H_{c_2}(T)	$F_{p_{max}}(N/m^3)$	b_p	C	n	m	σ
0.0063	4.06K	10.25	5.26×10^9	0.51	5.5	1.24	1.21	0.057
0.0063	5.39K	7.33	2.84×10^9	0.54	3.2	0.92	0.79	0.039
0.0063	6.55K	4.83	1.07×10^9	0.47	4.3	0.98	1.12	0.038
0.0063	7.58K	2.41	2.37×10^8	0.36	7.5	1.11	1.93	0.047
0.0063	8.13K	0.92	2.68×10^7	0.25	9.4	0.99	2.95	0.036
0.0113	4.12K	9.88	5.50×10^9	0.50	4.4	1.08	1.07	0.050
0.0113	5.39K	7.71	3.07×10^9	0.46	5.2	1.10	1.28	0.055
0.0113	6.60K	5.16	1.22×10^9	0.40	7.8	1.20	1.82	0.061
0.0113	7.64K	2.54	2.73×10^8	0.32	14.9	1.36	2.91	0.044
0.0113	8.30K	1.08	1.06×10^7	0.14	10.1	0.81	4.82	0.052
0.0179	4.12K	10.11	6.79×10^9	0.48	4.7	1.08	1.15	0.047
0.0179	5.50K	7.66	3.56×10^9	0.44	5.3	1.05	1.36	0.047
0.0179	6.77K	5.00	1.40×10^9	0.37	6.7	1.06	1.79	0.042
0.0179	7.73K	2.44	3.26×10^8	0.30	9.7	1.11	2.58	0.022
0.0179	8.36K	1.00	1.71×10^7	0.18	3.2	0.46	2.16	0.034
0.0285	4.13K	9.98	7.91×10^9	0.47	4.3	0.98	1.13	0.031
0.0285	5.47K	7.74	4.36×10^9	0.42	4.9	0.98	1.35	0.033
0.0285	6.64K	5.14	1.85×10^9	0.38	5.6	0.96	1.60	0.030
0.0285	7.73K	2.77	4.04×10^8	0.25	9.8	1.02	2.97	0.037
0.0285	8.36K	1.19	2.93×10^7	0.15	7.2	0.71	3.99	0.043
0.050AHT	3.99K	10.18	6.37×10^9	0.41	5.0	0.97	1.39	0.037
0.050AHT	5.44K	7.82	3.33×10^9	0.36	5.4	0.92	1.63	0.045
0.050AHT	6.67K	4.79	1.34×10^9	0.34	4.6	0.80	1.54	0.027
0.050AHT	7.69K	2.41	3.42×10^8	0.27	6.4	0.85	2.33	0.018
0.050AHT	8.38K	0.80	1.40×10^7	0.13	4.0	0.49	3.28	0.048

Table 5.5: The upper critical field, maximum pinning force, calculated peak field and scaling coefficients for the Nb53wt% Ti wires (UW2319).

Size (in)	Temp.	H_{c_2}(T)	$F_{p_{max}}(N/m^3)$	b_p	C	n	m	σ
0.0063	4.15K	10.01	4.49×10^9	0.53	3.7	1.00	0.91	0.048
0.0063	5.47K	7.53	2.39×10^9	0.52	3.4	0.93	0.86	0.041
0.0063	6.71K	5.07	8.75×10^8	0.44	5.0	1.02	1.31	0.064
0.0063	7.60K	2.65	2.50×10^8	0.38	6.5	1.06	1.73	0.054
0.0063	8.13K	1.00	4.49×10^7	0.34	5.0	0.85	1.68	0.028
0.0113	4.02K	10.08	5.22×10^9	0.58	4.3	1.24	0.91	0.053
0.0113	5.42K	7.63	2.63×10^9	0.54	5.4	1.35	1.14	0.067
0.0113	6.60K	5.40	9.06×10^8	0.41	10.0	1.37	2.01	0.087
0.0113	7.50K	2.90	1.47×10^8	0.27	5.8	0.81	2.19	0.057
0.0113	7.91K	1.13	3.57×10^7	0.12	1.1	0.09	0.63	0.055
0.0179	4.16K	9.89	6.20×10^9	0.50	3.8	0.99	0.98	0.049
0.0179	5.40K	7.53	3.50×10^9	0.48	3.8	0.92	1.01	0.041
0.0179	6.68K	5.01	1.43×10^9	0.41	5.1	0.98	1.40	0.042
0.0179	7.76K	2.51	3.24×10^8	0.31	9.3	1.11	2.45	0.035
0.0179	8.43K	1.00	1.51×10^7	0.18	2.5	0.38	1.77	0.051
0.0285	4.17K	10.14	7.60×10^9	0.46	4.2	0.97	1.12	0.041
0.0285	5.61K	7.50	3.85×10^9	0.43	4.7	0.96	1.29	0.040
0.0285	6.85K	4.83	1.53×10^9	0.38	5.1	0.93	1.50	0.031
0.0285	7.83K	2.66	3.76×10^8	0.27	9.4	1.04	2.74	0.025
0.0285	8.49K	1.30	1.54×10^7	0.10	3.3	0.39	3.42	0.030
0.050AHT	3.75K	10.27	5.92×10^9	0.42	4.3	0.90	1.22	0.040
0.050AHT	5.26K	7.77	3.22×10^9	0.39	4.4	0.86	1.32	0.044
0.050AHT	6.66K	4.70	1.20×10^9	0.35	4.1	0.76	1.41	0.034
0.050AHT	7.74K	2.42	2.98×10^8	0.26	7.7	0.92	2.60	0.026
0.050AHT	8.39K	1.18	1.26×10^7	0.11	5.8	0.58	4.57	0.042

Table 5.6: The upper critical field, maximum pinning force, calculated peak field, and scaling coefficients for the Nb58wt% Ti wires (UW2419).

Size (in)	Temp.	H_{c_2}(T)	$F_{p_{max}}(N/m^3)$	b_p	C	n	m	σ
0.0063	2.91K	10.21	4.13×10^9	0.52	4.3	1.12	1.05	0.055
0.0063	4.46K	7.66	2.29×10^9	0.51	4.3	1.07	1.04	0.050
0.0063	5.73K	5.19	9.32×10^8	0.43	6.4	1.16	1.54	0.056
0.0063	6.84K	2.53	1.93×10^8	0.32	10.3	1.18	2.52	0.043
0.0063	7.47K	1.21	1.40×10^7	0.15	4.8	0.58	3.20	0.035
0.0113	3.07K	10.03	5.85×10^9	0.53	4.7	1.19	1.05	0.050
0.0113	4.64K	7.75	3.03×10^9	0.47	6.2	1.23	1.39	0.055
0.0113	5.98K	4.69	1.02×10^9	0.40	8.0	1.22	1.85	0.046
0.0113	7.06K	2.34	1.61×10^8	0.24	13.4	1.12	3.53	0.026
0.0113	7.62K	1.00	8.37×10^6	0.19	6.1	0.71	3.08	0.036
0.0179	3.18K	10.02	5.84×10^9	0.51	5.9	1.32	1.25	0.052
0.0179	4.69K	7.26	3.06×10^9	0.49	5.1	1.16	1.22	0.039
0.0179	5.89K	5.16	1.16×10^9	0.37	10.3	1.30	2.20	0.046
0.0179	7.09K	2.24	1.75×10^8	0.25	6.5	0.85	2.49	0.032
0.0179	7.58K	0.98	1.51×10^7	0.19	2.7	0.42	1.76	0.045
0.0285	3.59K	10.00	7.62×10^9	0.47	8.5	1.44	1.65	0.045
0.0285	4.85K	8.11	4.16×10^9	0.41	10.2	1.40	2.01	0.050
0.0285	6.03K	5.29	1.53×10^9	0.35	10.3	1.26	2.31	0.034
0.0285	7.18K	2.55	2.49×10^8	0.24	12.2	1.09	3.39	0.016
0.0285	7.90K	1.03	4.09×10^6	0.10	1.4	0.12	1.16	0.066
0.050AHT	3.46K	10.05	8.12×10^9	0.43	7.5	1.26	1.68	0.039
0.050AHT	5.01K	7.84	3.68×10^9	0.36	9.7	1.25	2.21	0.050
0.050AHT	6.31K	4.86	1.09×10^9	0.30	12.3	1.21	2.87	0.044
0.050AHT	7.33K	2.43	1.52×10^8	0.19	24.1	1.24	5.15	0.026
0.050AHT	7.88K	1.19	4.25×10^6	0.16	3.5	0.47	2.54	0.056

Table 5.7: The upper critical field, maximum pinning force, calculated peak field, and scaling coefficients for the Nb62wt% Ti wires (UW1819).

Size (in)	Temp.	H_{c_2}(T)	$F_{p_{max}}(N/m^3)$	b_p	C	n	m	σ
0.050AHT	3.18K	9.96	6.47×10^9	0.34	4.4	0.77	1.52	0.031
0.050AHT	4.70K	7.72	3.57×10^9	0.27	4.4	0.67	1.83	0.029
0.050AHT	5.99K	5.07	1.40×10^9	0.21	5.0	0.65	2.45	0.020
0.050AHT	7.13K	2.61	2.31×10^8	0.15	4.3	0.53	2.99	0.017
0.050AHT	7.75K	1.07	8.78×10^6	0.17	7.3	0.75	3.59	0.024

Chapter 6

Discussion

One of the important contributions of this study was to prove that the microstructures of the high Ti alloys are controllable. Being able to control the microstructures has allowed the confirmation of two models for flux pinning behavior in Nb-Ti alloys. In addition several areas warranting additional research have been identified.

6.1 Microstructure

This study has shown that the microstructures of the high Ti alloys are controllable [46, 47, 48]. A correlation was observed between increasing hardness during the first precipitation heat treatment and the formation of fine intragranular precipitation during the first heat treatment. This has significance

on the industrial scale where TEM facilities are often not available. Based on the results of this study, increasing hardness during the first heat treatment is indicative of intragranular precipitation. Although the intragranular precipitation may not be detrimental to the intrinsic J_c, the higher hardness may cause sausaging in a large multifilamentary billet.

The lack of an increase in hardness during the first heat treatment is not sufficient to determine that intragranular precipitation did not occur. As shown in figures 3.2, 3.5, 3.8, 3.11, and 3.14, hotter and longer heat treatments minimize the hardness increase during heat treatment. Furthermore, there has been no determination of the lower detection limit for intragranular precipitation by this method.

The initial prestrain needed to obtain a "soft" microstructure following the first heat treatment was shown in figure 3.44. Essentially, this graph shows the amount of initial cold work needed to insure that precipitation will occur in the grain boundaries. This implies that the precipitate morphology of these alloys is determined primarily by the degree of cold work given the alloy prior to heat treatment and by the alloy composition. This was shown in the micrographs of chapter 3. The precipitate morphology was only mildly dependent on temperature within the narrow temperature range (288°C-435°C) considered.

Figure 3.44 has several limitations with respect to generalizing the results

to alloys made by other vendors and to wires receiving other heat treatments. First, as is clear from the hardness data, the line in the graph must be a function of the heat treatment temperature. Second, the graph is probably specific to alloys which have had a thermal mechanical history similar to the standard process for Nb46.5wt%Ti. The alloys for this study were all melted and processed as close to the standard Nb46.5wt%Ti processing method as possible. Considering the large difference in diffusion rate across the alloy range, the grain size following the last recrystallization probably varied considerably (unfortunately there is no data available on this). If the grain size did vary radically following the recrystallization anneal, then varying degrees of cold work would be necessary to obtain the same metallurgical state in each alloy. This would also affect the placement of the line in the graph. Thus, although this graph has been extremely useful in the processing of the particular alloy rods used in this experiment, caution should be used in generalizing the results to alloys produced in a different manner. This also has implications for further research on high Ti alloys. Care should be taken during the alloy processing to insure that the grain size of all the alloys stays as small as possible.

The microstructural results from the wires receiving multiple heat treatments (section 3.3.2) showed very interesting behavior. In the wires initially exhibiting the non-uniform intragranular precipitation, those whose

total strain at the last heat treatment size crossed the line in figure 3.44 (CB7638, CB10238) had fairly uniform precipitation following heat treatment. For CB7938 where the total strain at the last heat treatment size still fell short of the line in figure 3.44 the final microstructure was still very inhomogeneous. This has implications for commercial Nb46.5wt%Ti composites where the extrusion temperature (~600°C) is generally high enough to cause precipitation. Although, at the extrusion stage the material likely does not have a high enough degree of initial cold work to ensure uniform precipitation, by the time of the final heat treatment enough total cold work has been given to form a uniform microstructure.

6.2 Critical Current Density

The highest J_c results were obtained in the standard experiment. As shown in figures 4.7 - 4.9, the best heat treatment in the standard experiment was 3X80h/420°C. However, considering that 3X40h/435°C ultimately did better than 3x40h/420°C one must wonder whether 3x80h/435°C would have been better than 3x80h/420°C. This question was addressed explicitly by Li and Larbalestier [50]. In their results the J_c versus strain curve for 3X80h/420°C was higher than the curve for 3X80h/435°C. A similar result occurred for the 40 h heat treatments in this study where the curves for

CB7X37 (3X40h/420°C) were above the curves for CB7X32 (3X40h/435°C). But in this study CB7X32 (3X40h/435°C) peaks at a higher strain than CB7X37 (3X40h/420°C) thus achieving a higher ultimate J_c. Unfortunately, in the data of Li and Larbalestier, the peak is never reached and thus the question of whether 435°C is intrinsically better than 420°C is unanswered. In the case of extrinsic limitation, 420°C will have better performance than 435°C. This is because the 420°C curve is always above the 435°C curve until the 420°C curve peaks. The reason for the latter peak in J_c for the 435°C heat treatment may be due to precipitate ripening at the hotter heat treatment temperature which then requires more final strain to achieve a microstructure of the same fine scale as obtained with a cooler heat treatment. In general, the trend for these three composites is clear: a longer, hotter heat treatment gives better J_c results. The question of what is too long and too hot warrants further investigation.

For the two highest Ti content alloys the 3X40h/435°C process performed better than 3X80h/420°C process. A plausible explanation for the improved performance obtained with the 435°C heat treatment may be based on kinetics. As shown by the isomorphology experiment, the precipitation rate in the alloy system is highly temperature sensitive. Thus, increasing the temperature by 15°C may lead to the formation of a more uniform (equiaxed) microstructure. This is supported by the decrease in hardness with

increasing temperature as shown in figures 3.11 and 3.14.

As was shown in figure 4.11, the Nb58wt%Ti alloy performs better at low fields than the Nb46.5wt%Ti alloy. This may partially be due to the difference in the precipitate size observed in the two wires. In figures 4.7 and 4.10 the peak J_c at 2 T for Nb58wt%Ti occurs at much lower strain than the peak in J_c for Nb46.5wt%Ti. Combining this information with the large difference in the percentage of precipitate and average precipitate diameter following the last heat treatment observed in some wires (table 3.1), it can be concluded that Nb58wt%Ti has larger precipitates following heat treatment than Nb46.5wt%Ti.

This difference may be quantified using the available data for CB7638 (Nb49wt%Ti) and CB7937 (Nb58wt%Ti). For CB7638 (Nb49wt%Ti), the percentage of precipitate was 14.9, the average precipitate area was 20400 nm^2, and at a strain of 5.3 the 2 T J_c was still increasing. For CB7937 (Nb58wt%Ti) the percentage of precipitate was 40.2, the average precipitate area was 12638 nm^2, and J_c peaked at a strain of 4.2. Thus, based on these areas, at the peak stain for Nb58wt%Ti the average precipitate area may be calculated to be 195 nm^2, while for Nb49wt%Ti the average precipitate area would be 99 nm^2. This large difference occurs even though for this comparison the Nb49wt%Ti had twice as long a heat treatment as the Nb58-wt%Ti. Considering the two pinning mechanisms proposed by Meingast

and Larbalestier, the large precipitate microstructure should exhibit more ΔH_c pinning and less $\Delta\kappa$ pinning than the finer microstructure. In many respects the large ribbons seen in figure 3.28 may act like the ribbon clusters seen by Meingast and Larbalestier with respect to ΔH_c pinning but the $\Delta\kappa$ contribution would be reduced significantly with respect to the ribbon clusters.

The current densities observed in the isomorphology experiment were low ($\approx$1200 A/mm^2at 5 T and 4.2K). This raises the question of what are the important factors controlling J_c in Nb-Ti. From a microstructural point of view these alloys differ from standard Nb46.5wt%Ti in three ways. First, the percentage of α -Ti precipitate is about half that of standard Nb46.5wt%Ti wires [43, 44]. Second, as shown in figures 3.41 - 3.43, a ribbon morphology is not really formed in these wires. Third, the scale of the microstructure is about a factor of four smaller following the last heat treatment for UW2119 (effective diameter of the β grains $\overline{d}^* = 48.3nm$ following heat treatment) than for CB10038 ($d \approx 200nm$). Figure 4.22 shows a dependence of the critical current density on the percentage of α -Ti precipitate. Thus the lower J_c values obtained for the isomorphology experiment may be due to the low α -Ti fraction. However, the lack of the ribbon morphology may also be important. Without the ribbon clusters, there would be few regions of strong electron scattering coupled with higher local Ti concentration. If

the ribbon morphology is an important factor in the high J_c of Nb-Ti alloys then the idealized microstructures claimed for some artificial pinning center microstructures will be ineffective in producing high J_c [88].

6.3 Flux Pinning

The early flux pinning results of this study were similar to those seen in the literature [16, 70]. As shown in figure 5.1 the peak in the pinning force curve shifted to lower field with increasing Ti content. With increasing Ti content, there was also an increase in the percentage of precipitate which occurred (table 3.1). It seemed probable that the change in the pinning behavior was due to the observed change in microstructure. However, Meingast and Larbalestier had proposed that the shift in the pinning force curves toward lower field was due to the competition between the ΔH_c and $\Delta\kappa$ pinning mechanisms. The isomorphology experiment was designed to answer the question concerning which effect was causing the large shift toward lower field. If the microstructure was kept constant and the pinning force curves still shifted toward lower field, then Meingast and Larbalestier's hypothesis would be confirmed. But if the pinning force curves all showed the same behavior for a constant microstructure then the previously observed changes in f_p behavior could be attributed to the microstructural changes.

The microstructural results of the isomorphology experiment were presented in section 3.7. Most of the samples had similar precipitation morphology with the α -Ti precipitate occurring in the grain boundary triple points and some grain boundary film. As described above, the Nb44wt%Ti and the Nb62wt%Ti had different precipitate morphologies. The rest of the wires had fairly constant quantities of precipitate with an average amount of $\approx$11%. Although there is still some variation in the microstructures, they are much more similar than any previously produced in this alloy system. Additionally, the microstructures are sufficiently similar to address Meingast and Larbalestier's hypothesis.

The critical temperature results from section 5.2.1 show a depression in T_c with increasing cold work. As shown in figure 1.2, for the alloys of this study, decreasing the Ti content would increase T_c. During a heat treatment α -Ti precipitation causes the β-Nb-Ti grains to become richer in Nb thus raising the T_c [59]. If the results of image analysis to determine the percentage of α -Ti precipitate from TEM micrographs are consistent, then the T_c following heat treatment should be a smoothly varying function of the composition of the β grains. This is exactly what is seen in figure 3.1 with the exception of the result from the standard grade (i.e. inhomogeneous) Nb53wt%Ti alloy. In general the depression of T_c with cold work following heat treatment is consistent with similar studies [59, 61].

Temperature scaling of F_p has often been observed in the Nb-Ti system [13, 16, 21, 22, 23, 24, 28, 54]. However, two recent studies both using good quality high homogeneity materials have found a lack of scaling [34, 62]. A considerable lack of scaling was observed in this study as well. This can be seen in figures 5.12 - 5.20 and 5.27 - 5.47. For the standard $F_{p_{max}}$ versus H_{c_2} curves (figures 5.12-5.18), the lack of scaling is most evident if a straight line is fit only to the four coldest data points. If this is done the data points for $H_{c_2} \approx 1$ T often fall below the line fit through the four other points. This effect is most noticeable as the Ti content of the alloy is increased. For the low Ti alloys (Nb44wt%Ti and Nb46.5wt%Ti) plots of $F_{p_{max}}$ versus H_{c_2} appear to scale until F_p at various reduced fields is plotted against H_{c_2} (figure 5.19) or the actual reduced pinning force curves are examined. It is clear from the data of this study and that of Meingast and Larbalestier that a wide range of temperature must be used and several reduced fields must also be examined to be sure scaling is taking place [62].

Another way to look at the lack of scaling in this system is by examining the fit coefficients to equation 5.1 in tables 5.1 - 5.7. These tables show a wide range of values for both n and m. The fit values for n range from 0.09 to 1.44 and the values for m range from 0.62 to 5.15. It is difficult to explain these results in terms of the field dependence caused by a particular type of pinning center.

There are some differences between the samples used by Meingast and Larbalestier and the samples from this study [61, 62]. The first obvious difference in the two studies is that a wider range of Ti compositions was used in this study. However, a more significant difference was observed in the microstructures of the two studies. Following the last precipitation heat treatment, Meingast and Larbalestier found 18.8% of α -Ti precipitate in their samples with an average precipitate area of 49300 $(nm)^2$. In this study the wires from Nb46.5wt%Ti to Nb58wt%Ti had an average of $\sim$ 11% α -Ti and an average precipitate area of 462 $(nm)^2$. The consequence of the fine microstructure in this study is that following heat treatment the density of α -Ti precipitates (or pinning centers) is $\approx 2 \times 10^{14}$ $ppts/m^2$ (for UW2119, the other wires are of comparable size) while for Meingast and Larbalestier's wire the density of α -Ti precipitates was $\approx 3 \times 10^{12}$ $ppts/m^2$. Due to the large difference in the density of pins following the heat treatment, the pinning force curves for this study are shifted to higher reduced field than those of Meingast and Larbalestier. This difference is consistent with Matsushita and Küpfer's model which attributes the difference in saturated pinning behavior and non-saturated pinning behavior to the density of pins and the strength of the elementary pinning force f_p. These results can not be explained by models attributing the difference between saturated behavior and non-saturated behavior to the microstructural morphology since the shape

of the precipitates following heat treatment in this study and the shape of Meingast and Larbalestier's precipitates are similar [11, 12].

The fine scale microstructure of these alloys also had a large effect on the Nb58wt%Ti alloy. At low temperatures the peak in the pinning force curve (figures 5.44 - 5.46) is shifted to much higher reduced field than the pinning force curve for CB7938 in the standard experiment (figure 5.1). This means that the large observed shift toward low field in the high Ti alloys receiving standard processing is partially due to the large difference in the microstructure of the high Ti alloys relative to the microstructure of Nb46.5-wt%Ti. However, as discussed below, it is not the only factor in the shift to low fields generally observed in the high Ti alloys.

Considering the large size difference of the as heat treated microstructure of the wires from Meingast and Larbalestier's study and the as heat treated wires from this study, it is not surprising that the microstructures obtained with subsequent cold work were also different. In Meingast and Larbalestier's wires, cold work following heat treatment caused the formation of α -Ti ribbon clusters. The ribbon cluster morphology is commonly observed in high J_c Nb-Ti wires [43, 44]. For the wires of this study there is no indication of the ribbon morphology in figures 3.41 to 3.43. With the presence of the ribbon morphology Meingast and Larbalestier observed a gradual shift toward lower reduced field with increasing temperature. With the lack of ribbons

in this study the finest Nb46.5wt%Ti wire (UW2119 0.0063") does not show a large shift toward lower field with increasing temperature (figure 5.34). This indicates that the shift toward lower field observed by Meingast and Larbalestier was in part due to the ribbon clusters which would act as local regions of higher average Ti content.

Overall, the reduced flux pinning curves from this study showed three major trends. First, as the temperature was increased, b_p became smaller. Second, cold working the wire following heat treatment caused b_p to become larger. Finally, increasing the Ti content caused b_p to become smaller. The dependence of b_p on the overall Ti content of the alloy supports the hypothesis of Meingast and Larbalestier.

The dependence of the flux pinning on the alloy content can be seen most clearly by comparing figures 5.30 to 5.34 (Nb46.5wt%Ti) and figures 5.44 to 5.46 (Nb58wt%Ti). The $H_{c_2} \approx 1$ T curves for the Nb46.5wt%Ti wires show increasing b_p with increasing ϵ_f. However, for Nb58wt%Ti the $H_{c_2} \approx 1$ T curves remain shifted to low field through the entire cold working process. Since the curves remain at low field, ΔH_c pinning must be dominating the high temperature pinning behavior for Nb58wt%Ti.

The tendency for ΔH_c pinning to dominate can be viewed differently by making a plot similar to figure 1.7 for the alloys of this study. Figure 6.1 shows normalized ΔH_c and $\Delta\kappa$ values for the alloys of this study. The

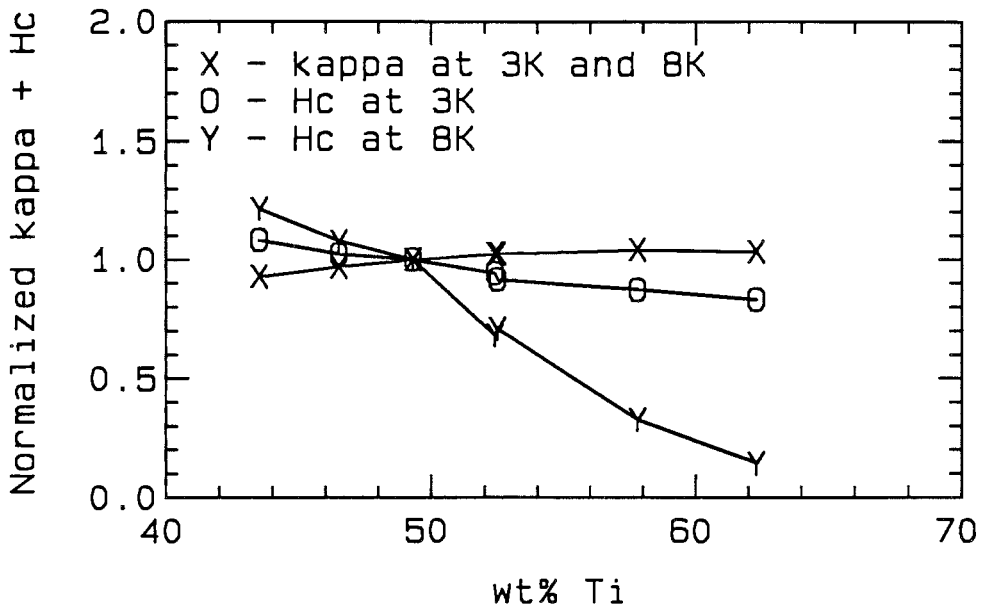

Figure 6.1: Values of κ and H_c calculated using κ from figure 1.5 and normalized to Nb49wt%Ti.

curves in figure 6.1 were calculated using the κ values in figure 1.5 and second order least squares fits to the data in figures 5.5 to 5.11 to calculate H_c. Although the shape of the curves is different from those calculated by Meingast and Larbalestier the same general trends are visible. At low temperatures the rate of change for H_c and κ with overall alloy content are similar. As the temperature is increased the relationship between H_c and the alloy composition becomes stronger while the relationship between κ and the alloy content is assumed temperature independent in this case.

The results of a more detailed calculation of κ and H_c versus composition are shown in figure 6.2. In this case a curvature of the H_c versus composition curves similar to that of figure 1.7 is seen at high temperature but the

low temperature and κ curves are too noisy to discern a relationship. In order to calculate these curves the following approach was used. dB_{c_2}/dT was determined from figures 5.5 - 5.11. These slopes were the used in the expression

$$-\frac{dH_{c_2}}{dT} = 4.48 \times 10^4 \gamma\rho \ (Oe/K) \tag{6.1}$$

where γ is the electronic specific heat in $(erg)/(cm^3K^2)$ and ρ is the resistivity in Ωcm [68]. The resistivity was then determined using second order least squares fits to Muller's specific heat data [66]. The resulting resistivity values were then used in equation 1.1 with the fit to Muller's specific heat data to obtain κ_{GL}. The temperature dependence of κ was then taken into account by assuming a straight line between the limiting cases in Maki's calculations which gives

$$\kappa_1 = \kappa_{GL}\left[1.2 - .2\left(\frac{T}{T_c}\right)\right]. \tag{6.2}$$

The resulting temperature dependent κ values were then used, together with the second order fits to B_{c_2} versus T, to determine the temperature dependent H_c values. Ratios of the κ_1 values and H_c values were then used to make figure 6.2.

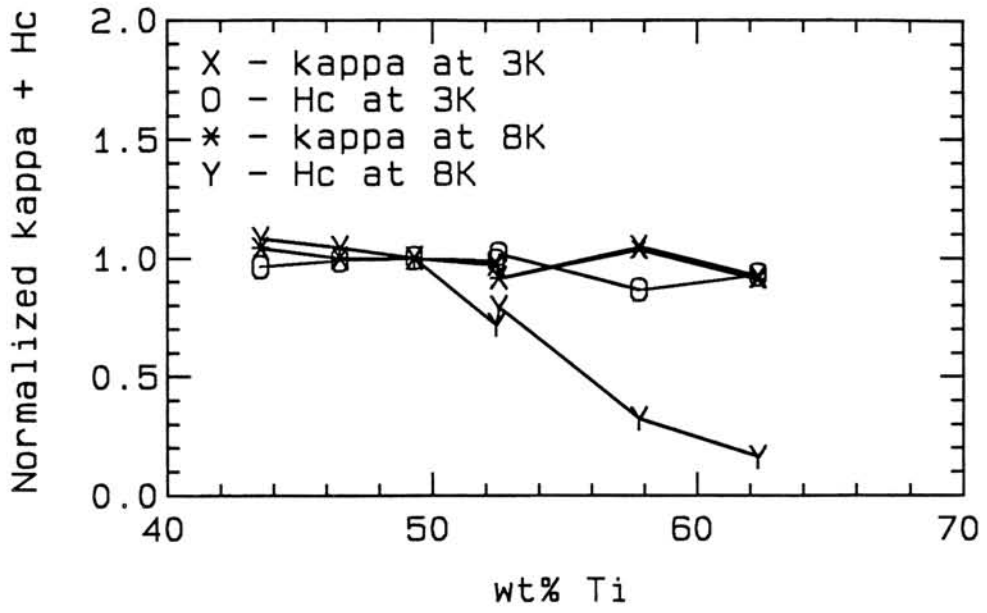

Figure 6.2: Values of κ and H_c calculated using κ_1 from [53] and normalized to Nb49wt%Ti.

6.4 Impact on Superconducting Magnetic Energy Storage

The original purpose of this study was to improve the low field (2-3 T) critical current density in the Nb-Ti alloy system. As shown in figure 4.11 this goal has been accomplished in a wire fabricated from Nb58wt%Ti (J_c(2T, 4.2K) = $7400 A/mm^2$). Further increases in the low field current density have been accomplished with Zr additions to the alloy [57]. Although these increases in J_c are substantial, the high hardness observed in the high Ti alloys receiving standard processing may prevent successful fabrication of large multifilamentary wires from these alloys due to mechanical instabilities dur-

ing the processing. In Nb58wt%Ti the high hardness can be eliminated by increasing the initial cold work prior to heat treatment to a true strain of 12 (see section 3.7). These strains are larger than can presently be performed on a commercial scale, since the total strain space available during a typical commercial process is $\epsilon_t = 12$. Furthermore, on an industrial scale the initial working of the alloys is typically performed using warm (550°C - 650°C) extrusion. This high extrusion temperature might cause intragranular precipitation in the early stages of fabrication. A potential solution to the high temperatures of conventional extrusion is the relatively cool (≈250°C) isostatic extrusion process. But even 250°C is fairly warm for the high Ti alloys, as evidenced by the precipitation in Nb62wt%Ti at 288°C. Additionally, the hot isostatic pressing process (550°C/1 hr), which is commonly performed to insure good bonding of fine filament composites, could allow the hardening phases to form.

As discussed previously (section 6.1), the grain size following the recrystallization anneal probably increased as the Ti content was increased for the alloys of this study. If such an increase in grain size exists, then it might explain the large increases in the initial cold work needed with increasing overall Ti content to insure grain boundary triple point precipitation in the high Ti alloys. This is an important issue that could not be checked in the present study and should form part of further research on the high Ti alloys.

Particular interest should be paid to the parameters of the recrystallization anneal such that the grain size of the high Ti alloys is similar to that of standard Nb46.5wt%Ti following the recrystallization anneal. Based on a 10:1 price ratio for Nb and Ti and on the current ratio of J_c values between Nb46.5wt%Ti and Nb58wt%Ti, there is a potential for saving 15-20% on the cost of the Nb-Ti alloy in a large low field machine by using a high Ti content Nb-Ti alloy.

Chapter 7

Summary

The microstructures of the high Ti content Nb-Ti alloys can be controlled by increasing the initial cold work prior to heat treatment. Thus the classification of Nb-Ti alloys into three separate groups is unwarranted [35]. High critical current densities ($7400 A/mm^2$) at low field (2-3 T) have been obtained by increasing the Ti content in Nb-Ti alloys from Nb46.5wt%Ti to Nb58wt%Ti. However, the increase in current density may not be attainable in industrial scale composites due to the high hardness values (DPN $>$ 300) which occurred in the high Ti alloys. The high hardness values have been attributed to the precipitation of intragranular Widmanstätten α-Ti and ω. The intragranular precipitation in the high Ti alloys was controlled by increasing the cold work prior to heat treatment but the level of cold work needed to control the hardness is about equal to the total amount of work

which can be given a commercial composite unless cold work can be retained through a low temperature extrusion. However, effects of the starting grain size may have also contributed to this dependence. Controlling grain growth during recrystallization may allow uniform precipitation to occur with standard processing techniques. Thus if future designs of large low field systems propose to take advantage of the potential cost reduction of 15% to 20% of the high Ti alloys, further research on controlling grain growth during recrystallization and optimization of the resulting fine grained alloy should be performed.

On a fundamental level this study produced a set of samples with similar microstructures in alloys having compositions from Nb46.5wt%Ti to Nb58-wt%Ti. The microstructure obtained in these samples was controlled by using a high degree of initial cold work to control the precipitate morphology and varying precipitation heat treatment temperatures to control the percentage of precipitate. Characterization of these samples using transmission electron microscopy techniques showed a two order of magnitude increase in the density of pins following heat treatment compared to the wire of Meingast, Lee and Larbalestier [61]. The increased density of pins following heat treatment caused non-saturated pinning behavior at low temperatures and is consistent with Matsushita and Küpfer's model [58]. The pinning behavior of the samples with similar microstructures showed a distinct dependance

on the overall Ti content of the alloy. As the Ti content was increased, the peak in the reduced pinning force curve shifted toward lower reduced field. Thus ΔH_c is the dominant pinning mechanism in the high Ti alloys which confirms Meingast and Larbalestier's hypothesis [62].

Bibliography

[1] D. Ablitzer, *Phil. Mag.*, **35**, 1239 (1976).

[2] A. Abrikosov, *Soviet Physics JETP*, **5**, 1174 (1957).

[3] J. Bardeen, L. Cooper and J. Schrieffer, *Phys. Rev.*, **108**, 1175 (1957).

[4] C. Bean, *Rev. Mod. Phys.*, **36**, 31 (1964).

[5] G. Beckwith, N. Lewis Buck and Roy Marangoni, "Mechanical Measurements", 3rd ed., Reading, Massachusetts: Addison-Wesley Publishing Co., 1982.

[6] R. Boom, B. Haimson, G. McIntosh, H. Peterson and W. Young, *IEEE Trans. Mag.*, **MAG-11**, 475 (1975).

[7] M. Buckett and D. Larbalestier, *IEEE Trans. Mag.*, **23**, 1638 (1986).

[8] M. Buckett, Masters Thesis-University of Wisconsin-Madison, (1985).

[9] A. Campbell and J. Evetts, *Adv. Phys.*, **21**, 199 (1972).

[10] D. Dew-Hughes, *Phil. Mag.*, **30**, 293 (1974).

[11] D. Dew-Hughes, *Phil. Mag.*, **55**, 459 (1987).

[12] J. Evetts and C. Plummer, "Proceedings of the Int. Symp. on Flux Pinning and Electromagnetic Properties of Superconductors," Fukoka, Japan, 146 (1986).

[13] W. Fietz and W. Webb, *Phys. Rev.*, **178**, 657 (1969).

[14] S. Foner, *Phys. Rev.*, **101**, 548 (1956).

[15] S. Foner, *Rev. Sci. Inst.*, **30**, 548 (1959).

[16] G. Fuchs, *Phys. Stat. Sol. (a)*, **54**, 321 (1979).

[17] G. Gibbs, D. Grahm and D. Tomlin, *Phil. Mag.*, **8** 1269 (1963).

[18] V. Ginzburg and L. Landau, *Zh. Eksperim. i Thor. Fiz.*, **20**, 1064 (1950).

[19] L. Goodrich, D. Vecchia, E. Pitttman, J. Ekin and A. Clark, "Critical Current Measurements on an NbTi Superconducting Wire Standard Reference Material," NBS Special Publication 260-91 (1984).

[20] E. Gregory, *Cryogenics*, **27**, 290 (1987).

[21] R. Hampshire and M. Taylor, *J. Phys. F*, **2**, 89 (1972).

[22] D. Hampshire and H. Jones, MT9, published by SIN, 531 (1985).

[23] D. Hampshire and H. Jones, *Cryogenics*, **27**, 608 (1987).

[24] D. Hampshire and D. Larbalestier, *IEEE Trans Mag*, **25**, 1956 (1989).

[25] M. Hanson, E. Kamen, H. Kessler and D. McPherson, *J. Metals*, **3**, 881 (1951).

[26] M. Hanson and K. Anderko, "Constitution of Binary Alloys," New York: McGraw-Hill Book Co., Inc., 1958.

[27] D. Hawksworth and D. Larbalestier, *Adv. Cryo. Eng.*, **26**, 429 (1980).

[28] D. Hawksworth and D. Larbalestier, *Proc. 8th Symp. Eng. Prob. Fusion Res.*, IEEE Publ. #79CH14441-5, 249 (1979).

[29] D. Hawksworth, Ph. D. Thesis — University of Wisconsin - Madison (1981).

[30] S. Hong, Work presented at the 8th NbTi Workshop, Asilomar, CA, March 14–16, 1988.

[31] P. Jablonski, University of Wisconsin - Madison, Private Communication, (1990).

[32] H. Kanthi, F. Krahula, M. Erdmann, R. Schaedler and B. Zeitlen, *Proceedings of the IISSC*, **1**, 223 (1989).

[33] E. Kramer, *J. Appl. Phys.*, **44**, 1360 (1973).

[34] H. Küpfer and T. Matsushita, *J. Appl. Phys.*, **63**, 5060 (1988).

[35] D. C. Larbalestier, "Superconductor Materials Science" (ed. by S. Foner and B. B. Schwartz), Plenum Press, NY, 1981, p. 133.

[36] D. Larbalestier and A. West, *Acta Met.*, **32**, 1871 (1984).

[37] D. Larbalestier, A. West, W. Starch, W. Warnes, P. Lee, W. McDonald, P. O'Larey, K. Hemachalam, B. Zeitlen, R. Scanlan and C. Taylor, *IEEE Trans. Mag.*, **MAG21**, 269 (1985).

[38] D. Larbalestier, P. Lee and R. Samuel, *Adv. Cryo. Eng.*, **32**, 715 (1986).

[39] D. Larbalestier, P. Lee, C. Li and W. Warnes, Paper presented at ICFA Workshop on Superconducting Magnets and Cryogenics, Brookhaven National Laboratory (1986).

[40] D. Larbalestier, D. Smathers, M. Daeumling, C. Meingast, W. Warnes and K. Marken, "Proceedings of the Int. Symp. on Flux Pinning and Electromagnetic Properties of Superconductors," Fukuoka, Japan, 58 (1986).

[41] D. Larbalestier, University of Wisconsin - Madison, Private Communication, (1986).

[42] P. Lee and D. Larbalestier, *Proc. of 43 Conf. EMSA*, Ed. G. Bailey San Francisco Press, 186 (1985).

[43] P. Lee and D. Larbalestier, *Acta Met.*, **35**, 2533 (1987).

[44] P. Lee and D. Larbalestier, *J. Mat. Sci.*, **23**, 781 (1988).

[45] P. Lee, *Proc. of EMSA 45*, 358 (1987).

[46] P. Lee, D. Larbalestier and J. McKinnell, *Adv. Cryo. Eng*, **34**, 967 (1988).

[47] P. Lee, J. McKinnell and D. Larbalestier, *IEEE Trans. Mag.*, **25**, 1918 (1989).

[48] P. Lee, J. McKinnell and D. Larbalestier, "Proc. Int. Sym. New Dev. in Superconductivity", ed. Y. Murakami, 357 (1989).

[49] C. Li, X. Wu and N. Zhou, *IEEE Trans. Mag.*, **19**, 284 (1983).

[50] C. Li and D. Larbalestier, *Cryogenics*, **27**, 171 (1987).

[51] F. London and H. London, *Proc. Roy. Soc.* (London), **A149**, 71 (1935).

[52] T. Lundy, F. Winslow, R. Pawel and C. McHargue, *Trans. Met.*, **233**, 1533 (1965).

[53] K. Maki, *Physics*, **1**, 21 (1964).

[54] M. Mathur, M. Ashkin and D. Deis, *J. Appl. Phys.*, **45**, 3627 (1974).

[55] A. McInturff and G. Chase, *J. Appl. Phys.*, **44**, 2378 (1973).

[56] J. McKinnell, P. Lee, R. Remsbottom, D. Larbalestier, W. McDonald and P. O'Leary, *Adv. Cryo. Eng.*, **34**, 1001 (1988).

[57] J. McKinnell, P. Lee and D. Larbalestier, *IEEE Trans. Mag.*, **25**, 1930 (1989).

[58] T. Matsushita and H. Küpfer, *J. Appl. Phys.*, **63**, 5048 (1988).

[59] C. Meingast, M. Daeumling, P. Lee and D. Larbalestier, *Appl. Phys. Lett.*, **51**, 688 (1987).

[60] C. Meingast, Ph. D. Thesis-University of Wisconsin-Madison (1988).

[61] C. Meingast, P. Lee and D. Larbalestier, *J. Appl. Phys.*, **66**, 5962 (1989).

[62] C. Meingast and D. Larbalestier, *J. Appl. Phys.*, **66**, 5971 (1989).

[63] D. Moffat, Ph. D. Thesis-University of Wisconsin-Madison (1986).

[64] D. Moffat and D. Larbalestier, *Met. Trans.*, **19A**, 1677 (1988).

[65] D. Moffat, D. Larbalestier, *Met. Trans.*, **19A**, 1687 (1988).

[66] H. Muller, Ph. D. Thesis-University of Wisconsin-Madison (1989).

[67] D. Neal, A. Barber, A. Woolcock and J. Gidley, *Acta Met.*, **19**, 143 (1971).

[68] T. Orlando, E. McNiff, S. Foner and M. Beasley, *Phys. Rev. B*, **19**, 4545 (1979).

[69] A. Pacyna, *J. Phys. E*, **15**, 663 (1982).

[70] M. Panek, D. Pattanayak, R. Meier-Hirmer and H. Küpfer, *J. Appl. Phys.*, **54**, 7083 (1983).

[71] R. Peart and D. Tomlin, *Acta Met.*, **10**, 123 (1962).

[72] R. Peart, D. Graham and D. Tomlin, *Acta Met.*, **10**, 519 (1962).

[73] I. Pfeiffer and H. Hillmann, *Acta Met.*, **16**, 1429 (1968).

[74] A. Pontau and D. Lazarus, *Phys. Rev. B*, **19**, 4027 (1979).

[75] R. Remsbottom, Superconducting Super Collider Laboratory, Private Communication (1986).

[76] R. Resnick and L. Castleman, *Trans. Met.*, **218**, 307 (1960).

[77] B. Roberts, NBS Technical Note #482, pg VII-1 (1969).

[78] F. Roux and A. Vignes, *Rev. Phys. Appl.*, **10**, 393 (1970).

[79] M. Springford, J. Stockton and W. Wampler, *J. Phys. E*, **4**, 1036 (1971).

[80] H. Ullmaier, "Irreversible Properties of Type II Superconductors", Springer Tracts in Modern Physics, **76** (1975).

[81] J. Vetrano and R. Boom, *J. Appl. Phys.*, **36**, 1179, (1965).

[82] N. Walsoe de Reca and C. Libanati, *Acta Met.*, **16**, 1297 (1968).

[83] W. Warnes, Oregon State University, Private Communication (1986).

[84] A. West and D. Larbalestier, *Adv. Cryo. Eng.*, **26**, 471 (1980).

[85] J. Willbrand and W. Schlump, *Z. Metallkunde*, **66**, 714 (1975).

[86] J. Willbrand and R. Ebeling, *Metall*, **29**, 677 (1975).

[87] W. Yetter, D. Thomas and E. Kramer, *Phil. Mag. B*, **46**, 523 (1982).

[88] B. Zeitlin, M. Walker and L. Motouidlo et al., US Patent #4803310, (1989).

[89] G. Zerweck, *J. Low Temp. Phys.*, **42**, 1 (1981).

Appendix A

f_p Curve Fitting

The reduced pinning force curves in chapter 5 were fit to the equation:

$$f_p = Cb^n(1-b)^m \tag{A.1}$$

writing this equation in standard least squares form gives:

$$q = \sum_{i=1}^{n_p} [y_i - Cb_i^n(1-b_i)^m]^2 \tag{A.2}$$

where q is the sum of the squares being minimized, i is the index, n_p is the number of data pairs being fit, y_i is the ith y value, b_i is the ith $b\,(x)$ value, and C, n and m are the coefficients of the fit. Taking derivatives of equation A.2 with respect to the three fit coefficients yields:

$$\frac{dq}{dC} = \sum_{i=1}^{n_p} -2y_i b_i^n(1-b_i)^m + 2Cb_i^{2n}(1-b_i)^{2m} \tag{A.3}$$

$$\frac{dq}{dn} = \sum_{i=1}^{n_p} -2y_i C(1-b_i)^m b_i^n \ln(b_i) + 2C^2(1-b_i)^{2m} b_i^{2n} \ln(b_i) \quad \text{(A.4)}$$

$$\frac{dq}{dm} = \sum_{i=1}^{n_p} -2y_i C b_i^n (1-b_i)^m \ln(1-b_i) + 2C^2 b_i^{2n} (1-b_i)^{2m} \ln(1-b_i) \quad \text{(A.5)}$$

This set of equations is non-linear in the coefficients. Thus an iterative method must be used to minimize q by varying C, n, and m. For each iteration the coefficient with the largest derivative is modified. To test the goodness of fit the standard deviation of the fit was calculated as follows [5]

$$D_i = y_i - f_p(x_i) \quad \text{(A.6)}$$

$$\overline{D} = \frac{\sum_{i=1}^{n_p} D_i}{n_p} \quad \text{(A.7)}$$

$$\sigma = \sqrt{\frac{\sum_{i=1}^{n_p} (D_i - \overline{D})^2}{n_p - 1}} \quad \text{(A.8)}$$

The above equations are implemented in the following program:

```
/*******************************************************/
/*Program Purpose:find the coefs in fp = C*b^n*(1-b)^m*/
/*Programmer: Jim McKinnell                            */
/*Date: 9/23/89                                        */
/*******************************************************/
#include "stdio.h"
#include "libraries/dos.h"
#include "math.h"

#define MAXPOINTS 2000
  struct FileHandle *File;

#define MAXPOINTS 2000
#define SPREAD 0.1
#define MA 3


main(argc, argv)
int argc;
```

```
char *argv[];
{
  double *x,*y, C, n, m, q, dqdC, dqdn, dqdm,
         old_q, old_C, old_n, old_m;
  double C_scale, n_scale, m_scale, ymax, bp, step, yy,
         diff, avg_diff;
  long  len, error;
  int numpoints, ia, ib, ic, it;
  double temp, logC;
  FILE *fp, *fopen();
  char xhead[80], yhead[80], *malloc(), OutBuf[256];
  int atoi();
  struct FileHandle *Open();

  if(argc != 2) {
    printf("Usage: %s InFile\n", argv[0]);
    exit(100);
  }
  x=(double *) malloc((unsigned)(MAXPOINTS *
    sizeof(double)));
  x--;
  y=(double *) malloc((unsigned)(MAXPOINTS
     * sizeof(double)));
  y--;

  numpoints = 0;
  fp = fopen(argv[1], "r");
  if(fp == NULL) {
    printf("Could not open file %s!\n", argv[1]);
    goto exit2;
  }
  fscanf(fp, "%s %s", xhead, yhead);
  while((ia = fscanf(fp, "%le %le", &(x[numpoints+1]),
        &(y[numpoints+1]))) != EOF) {
    if((x[numpoints+1] > 0.0) && (x[numpoints+1] < 1.0)
       && (y[numpoints+1] > 0.0)&&(y[numpoints+1] < 1.0))
        ++numpoints;
    if(numpoints == MAXPOINTS) {
      printf("ERROR! data file too large.\n");
      goto exit5;
    }
```

```
  }
fclose(fp);

  it = 0;
  ymax = y[1];
  bp = x[1];
  step = 0.05;
  for(ia = 1; ia <= numpoints; ++ia) {
    if(y[ia] > ymax) {
      ymax = y[ia];
      bp = x[ia];
    }
  }
  n = 0.000001;
  q = 1e10;
  old_q = q;
  while(q > 0.0) {
    m = n*(1/bp - 1);
    C = 1/(pow(bp,n)*pow((1-bp),m));
    it++;
    q = 0;
    for(ia = 1; ia <= numpoints; ++ia) {
      yy = C * pow(x[ia],n) * pow((1-x[ia]),m);
      q += (y[ia]-yy) * (y[ia]-yy);
    }
    if((temp=fabs(q - old_q)) < 0.00001) {
      printf("%s\n", argv[1]);
      printf(" Primary:fp = %f*b^%f*(1-b)^%f, q = %f\n",
         C, n, m, q);
      goto finetune;
    }
    if(q < old_q) {
      n = n + step;
      old_q = q;
    } else {
      n = n - step;
      step = (step / 2);
      n = n + step;
    }
  }
finetune:
```

```
  C_scale = 0.5;
  m_scale = 0.5;
  n_scale = 0.5;
  q = 0.0;
  logC = log(C);
  for(ia = 1; ia <= numpoints; ++ia) {
    temp = y[ia] - C * pow(x[ia], n) * pow(1.0-x[ia], m);
    q += temp * temp;
  }
  old_q = 10000;
  while(fabs(old_q - q) > 0.00001) {
    old_q = q;
    dqdC = 0.0;
    logC = log(C);
    for(ia = 1; ia <= numpoints; ia++)
      dqdC += -2.0*y[ia]*pow(x[ia],n)*pow(1.0-x[ia],m)+
         2.0*C*pow(x[ia],2.0*n)*pow(1.0-x[ia],2.0*m);
    dqdn = 0.0;
    for(ia = 1; ia <= numpoints; ia++)
      dqdn += -2.0*y[ia]*C*pow(1.0-x[ia],m)*pow(x[ia],n)
            *log(x[ia])+C*C*pow(1.0-x[ia],2.0*m)
            *pow(x[ia],2.0*n)*log(x[ia])*2;
    dqdm = 0.0;
    for(ia = 1; ia <= numpoints; ia++)
      dqdm += -2.0*y[ia]*C*pow(x[ia],n)*pow(1.0-x[ia],m)
            *log(1.0-x[ia])+C*C*pow(x[ia],2.0*n)
            *pow(1.0-x[ia],2.0*m)*log(1.0-x[ia])*2;
    old_C = C;
    old_n = n;
    old_m = m;
loop:
    if((fabs(dqdC) > fabs(dqdn)) && (fabs(dqdC) >
       fabs(dqdm))) {
      C = C - q / dqdC * C_scale;
    } else if((fabs(dqdn) > fabs(dqdC)) && (fabs(dqdn)
       > fabs(dqdm))) {
      n = n - q / dqdn * n_scale;
    } else if((fabs(dqdm) > fabs(dqdC)) && (fabs(dqdm)
       > fabs(dqdn))) {
      m = m - q / dqdm * m_scale;
    } else {
```

```
      printf("Error in derivitaves!\n");
      break;
    }
    ++it;
    q = 0.0;
    logC = log(C);
    for(ia = 1; ia <= numpoints; ++ia) {
    temp = y[ia] - C * pow(x[ia], n) * pow(1.0-x[ia], m);
      q += temp * temp;
    }
    if(q > old_q) {
      q = old_q;
      if(C != old_C) {
        C = old_C;
        C_scale = C_scale / 2.0;
        n_scale = 0.1;
        m_scale = 0.1;
      }  else if (n != old_n) {
        n = old_n;
        n_scale = n_scale / 2.0;
        C_scale = 0.1;
        m_scale = 0.1;
      } else if(m != old_m) {
        m = old_m;
        m_scale = m_scale / 2.0;
        C_scale = 0.1;
        n_scale = 0.1;
      }
      goto loop;
    }
  }
  printf(" finetune:fp = %f*b^%f*(1-b)^%f, q = %f\n",
    C, n, m, q);
  avg_diff = 0.0;
  for(ia = 1; ia <= numpoints; ++ia)
    avg_diff += y[ia] - C*pow(x[ia], n)*pow(1.0-x[ia], m);
  avg_diff = avg_diff / (double)numpoints;
  diff = 0.0;
  for(ia = 1; ia <= numpoints; ++ia) {
    temp = (y[ia] - C*pow(x[ia], n)*pow(1.0-x[ia], m))
      - avg_diff;
```

```
    diff += temp * temp;
  }
  diff = diff / (double)(numpoints - 1);
  diff = sqrt(diff);
  printf(" STD = %f, in %4d iterations\n",diff,it);
  goto exit2;
exit5:
  fclose(fp);
exit2:
  y++;
  free(y);
  x++;
  free(x);
}
```